


Spring 1-1-2017

# Laboratory Investigations of Gaseous Plume Structure Using Planar Laser-Induced Fluorescence

Margaret McHugh

University of Colorado at Boulder, mamc9610@colorado.edu

Follow this and additional works at: [https://scholar.colorado.edu/cven\\_gradetds](https://scholar.colorado.edu/cven_gradetds)

 Part of the [Civil and Environmental Engineering Commons](#), and the [Water Resource Management Commons](#)

---

## Recommended Citation

McHugh, Margaret, "Laboratory Investigations of Gaseous Plume Structure Using Planar Laser-Induced Fluorescence" (2017). *Civil Engineering Graduate Theses & Dissertations*. 74.  
[https://scholar.colorado.edu/cven\\_gradetds/74](https://scholar.colorado.edu/cven_gradetds/74)

This Thesis is brought to you for free and open access by Civil, Environmental, and Architectural Engineering at CU Scholar. It has been accepted for inclusion in Civil Engineering Graduate Theses & Dissertations by an authorized administrator of CU Scholar. For more information, please contact [cuscholaradmin@colorado.edu](mailto:cuscholaradmin@colorado.edu).

**Laboratory investigations of gaseous plume structure using  
planar laser-induced fluorescence**

by

**M.K. McHugh**

B.S., Ohio State University, 2015

A thesis submitted to the  
Faculty of the Graduate School of the  
University of Colorado in partial fulfillment  
of the requirements for the degree of  
Masters of Science  
Department of Civil Engineering

2017

This thesis entitled:  
Laboratory investigations of gaseous plume structure using planar laser-induced fluorescence  
written by M.K. McHugh  
has been approved for the Department of Civil Engineering

---

Prof. John Crimaldi

---

Prof. Roseanna Neupauer

---

Prof. Harihar Rajaram

Date \_\_\_\_\_

The final copy of this thesis has been examined by the signatories, and we find that both the content and the form meet acceptable presentation standards of scholarly work in the above mentioned discipline.

McHugh, M.K. (M.S. Civil Engineering)

Laboratory investigations of gaseous plume structure using planar laser-induced fluorescence

Thesis directed by Prof. John Crimaldi

A scalar plume is the spatial and temporal structure of a released scalar, such as heat, chemical or contaminant. The resulting downstream structure is governed by the 3D Advection-Diffusion equation, which couples both advection, through the Navier Stokes equations, and diffusion describing the relative relationship and structure of the plume. Solutions to these equations for turbulent flows are computationally expensive and therefore most of the understanding surrounding turbulent plume structure stems from experimental results. Currently, a majority of experiments investigating plume structure have been done in aqueous environments using planar laser-induced fluorescence (PLIF), while in gaseous environments experiments utilize single point ion detection techniques. This thesis adapted a current gaseous PLIF technique to study airborne 2D scalar plume structure to be suitable for capturing neutrally buoyant plume-like data under two boundary conditions: (1) free-stream release, and (2) near bed release. Processing of the two collected datasets included investigations into instantaneous behavior and computation of relevant statistical metrics including mean concentration, RMS of concentration fluctuations, and intermittency. Results in the free-stream and near bed data differ greatly in the instantaneous and statistical comparisons, suggesting a significant difference in airborne plume behavior once a boundary is introduced.

## Dedication

I would like to dedicate this thesis my best friend and partner Lukas Cameron for all his love and support. You have pushed me to become a better person and lead a life that I am truly proud of. Thank you for talking me through moments of doubt, pushing me to always find the positive, and for reminding me that sometimes I just need to take a deep breath and have a cold beer. You have continually been my rock and my number one fan, I am forever grateful and I love you.

## Acknowledgements

First, I would like to thank my advisor Dr. John Crimaldi. Thank you for the opportunity to work on this project, I have learned so much about what it means to be a scientist and experimentalist. I know much of what I have learned from you in the past two years will remain with me for the rest of my career and make me a better problem solver, engineer, and scientist. Thank you!

Second, I would like to thank my awesome research group. Specifically, Aaron True for all your guidance, patience, and time you spent helping me figure things out in and outside of the lab. I would have never been able to finish this project without your help, so thank you so much for taking time out of your work to help me with mine.

Eric, Kenny, Aaron, and Erin thank you guys for being all around awesome team, supporters and encouragers, and helping me problem solve both in and out the lab.

I will truly miss working with all of you. And of course thanks to all of you for being fun to drink beer with.

I would like to also thank all my peers who are also finishing their Masters, or continuing on to your PhD. Thanks for being a great cohort, and a fun group of people who love science and Colorado just as much as the next person. I am going to miss you all.

I would also like acknowledge NSF and the Brain Initiative for providing funding for a student to explore these topics and how they relate to olfaction. I have learned so much from this experience and feel honored to have been able to be part of such a wonderful collaborative team.

## Contents

<b>Chapter</b>	
<b>1</b>	<b>Literature Review</b> <span style="float: right;"><b>1</b></span>
1.1	Introduction . . . . . 1
1.2	Chemical Plumes in Ecology . . . . . 3
1.3	Physics of Odor Plumes . . . . . 6
1.3.1	Governing Equations . . . . . 6
1.3.2	Non-dimensional parameters for scalar plume transport . . . . . 10
1.3.3	Experimental Studies of Plume Structure . . . . . 13
1.4	Acetone Planar Laser Induced Fluorescence . . . . . 15
1.4.1	Origins of Gaseous PLIF . . . . . 15
1.4.2	The Acetone PLIF Technique . . . . . 16
1.4.3	Relevant Plume Studies . . . . . 16
1.5	Relationship of present work to previous studies . . . . . 17
<b>2</b>	<b>Methods</b> <span style="float: right;"><b>18</b></span>
2.1	Overview . . . . . 18
2.2	Flow Facility . . . . . 19
2.2.1	Wind Tunnel Description and Layout . . . . . 19
2.3	PLIF System Components . . . . . 24
2.3.1	Acetone Vapor Generation . . . . . 24

2.3.2	Delivery of Acetone to Wind Tunnel . . . . .	27
2.3.3	Acetone Safety . . . . .	28
2.4	PLIF System Components . . . . .	29
2.4.1	Nd:YAG doubled frequency UV Laser . . . . .	29
2.4.2	Camera . . . . .	30
2.4.3	Binning Images . . . . .	31
2.4.4	Camera Set Up . . . . .	32
2.4.5	Spectral Considerations . . . . .	32
2.4.6	Data Processing . . . . .	34
2.5	Collected Data Configurations . . . . .	38
<b>3</b>	<b>Results</b>	<b>39</b>
3.1	Unbounded Data Results . . . . .	39
3.1.1	Instantaneous Plume Structure . . . . .	39
3.1.2	Statistical Measures of Plume Structure . . . . .	44
3.2	Bounded Data . . . . .	56
3.2.1	Instantaneous Plume Structure . . . . .	56
3.2.2	Statistical Measures of Plume Structure . . . . .	59
<b>4</b>	<b>Summary</b>	<b>72</b>
4.1	Conclusion . . . . .	72
4.2	Ecological Significance . . . . .	72
4.3	Future Considerations . . . . .	74



**Bibliography** **76**

**Appendix**

<b>A</b>	Acetone Vapor Chemistry	<b>81</b>
	A.1 Full Flow Saturation . . . . .	81
	A.2 Temperature dependence on vapor pressure . . . . .	82
	A.3 Density Calculations . . . . .	83
	A.4 Explosive Limits of Acetone Vapor . . . . .	84
	A.4.1 Wind Tunnel Chemistry . . . . .	85
	A.4.2 Explosive Time . . . . .	87
<b>B</b>	Saturation of Flourophore	<b>94</b>
<b>C</b>	Continous vs. Pulsed Laser	<b>98</b>
<b>D</b>	Binning Comparison	<b>100</b>
	D.1 Unbounded Images . . . . .	100
	D.2 Near Bed Images . . . . .	102
<b>E</b>	Camera Components	<b>103</b>
	E.1 Zyla 4.2+ Specifications . . . . .	103
	E.2 Camera Comparisons . . . . .	105
	E.2.1 Evaluation of Current 5.5 Megapixel sCMOS camera versus Zyla 4.2+ camera.	105
	E.2.2 Comparing the Zyla 4.2+ to the Ultra 888 . . . . .	106
	E.3 F-Stop Theory and Calculations . . . . .	107
	E.4 Edmund Optics Notch Filter . . . . .	108
<b>F</b>	Camera Insight 4G Software Settings	<b>110</b>

<b>G</b> Acetone PLIF and Beer's Law	<b>111</b>
G.1 Understanding Beers Law in a Wind Tunnel . . . . .	111
<b>H</b> Codes for Processing Data	<b>119</b>
H.1 Code for processing unbounded data . . . . .	119
<b>I</b> Sources of Error and Noise	<b>122</b>

## Tables

### Table

2.1 Data Configurations . . . . .	38
-----------------------------------	----

## Figures

### Figure

1.1	Representative instantaneous gaseous plume structure. . . . .	2
1.2	Representative mean concentration gaseous plume structure. . . . .	3
2.1	Overview of experimental apparatus including the wind tunnel and PLIF components.	19
2.2	Exterior dimensions of the wind tunnel. . . . .	20
2.3	Detail of upstream contraction. . . . .	20
2.4	Uniform turbulence grid diagram with relevant length scales and mesh:diameter ratio..	22
2.5	Detail of test section. . . . .	23
2.6	Detail of downstream contraction. . . . .	23
2.7	Flow diagram of acetone vapor, with flow direction indicated by arrows. . . . .	25
2.8	Entire flow diagram of blending process, with flow direction labeled indicated by arrows. . . . .	28
2.9	Absorption spectra of acetone vapor from [32] . . . . .	33
2.10	Emission spectra of acetone vapor from [8] . . . . .	33
2.11	Transmission spectra of filter from Edmund Optics. . . . .	34
2.12	RMS spatial images (a) not flatfielded and (b) flatfielded. . . . .	37
2.13	Histogram of RMS values from Figure 2.12. . . . .	38
3.1	(a-b). Two representative false-color instantaneous plume structures for unbounded case. . . . .	40

3.2	Profiles of (a) streamwise at $y=0$ and (b) lateral locations at $x=10$ mm, and $x=60$ mm for the instantaneous plume shown in Figure 3.1a. . . . .	41
3.3	Profiles of (a) streamwise at $y=0$ and (b) lateral locations at $x=10$ mm, and $x=60$ mm for the instantaneous plume shown in Figure 3.1b. . . . .	42
3.4	Time series over periods of (a) 5 minutes and (b) 30 seconds at $z=0$ mm, $y=0$ mm, $x=10$ mm. Mean concentration is shown with dashed lines. . . . .	43
3.5	Time series over periods of (a) 5 minutes and (b) 30 seconds at $z=0$ mm, $y=-8$ mm, $x=40$ mm. Mean concentration is shown with a dashed line. . . . .	43
3.6	Time series over periods of (a) 5 minutes and (b) 30 seconds at $z=0$ mm, $y=-16$ mm, $x=70$ mm. Mean concentration is shown with a dashed line. . . . .	44
3.7	(a) Normalized mean concentration of the unbounded plume, with (b) corresponding streamwise profile at $y=0$ mm. . . . .	45
3.8	Smoothing comparisons for mean streamwise profile curve. . . . .	46
3.9	Lateral profiles of mean concentration at $x=10$ mm and $x=60$ mm. Gaussian fits are shown as dotted lines. . . . .	47
3.10	(a) Normalized RMS fluctuations of the unbounded plume with (b) corresponding streamwise profile at $y=0$ mm. . . . .	48
3.11	Lateral profiles of RMS at $x=10$ mm and $x=60$ mm. . . . .	49
3.12	Comparison of the mean and RMS streamwise profiles at $y=0$ mm. . . . .	50
3.13	(a) Intermittency for $C_T = 0.03C_0$ with (b) corresponding centerline profile at $y=0$ mm. . . . .	51
3.14	Lateral profiles of intermittency at $x=10$ mm and $x=60$ mm. . . . .	52
3.15	Contours of $C_T$ for $\gamma = 0.5$ . . . . .	53
3.16	Contours of $C_T$ for $\gamma = 0.1$ . . . . .	53
3.17	Map of the nine time series locations (denoted by x's) in relation to each statistical measure. . . . .	54

3.18	Representative time-series of instantaneous normalized concentration for each of the nine locations shown in Fig. 3.18. . . . .	55
3.19	Representative pdfs of instantaneous normalized concentration for each of the nine locations shown in Fig. 3.18. . . . .	56
3.20	(a-b) Two representative false color instantaneous plume structures for bounded case.	58
3.21	Profiles of (a) centerline and (b) lateral locations at $x=10$ mm, and $x=60$ mm for the instantaneous plume shown in Figure 3.21a. . . . .	59
3.22	Profiles of (a) centerline and (b) lateral locations $x=10$ mm, and $x=60$ mm for the instantaneous plume shown in Figure 3.21b . . . . .	60
3.23	Time series over periods of (a) 5 minutes and (b) 30 seconds at $z=0$ mm, $y=0$ mm, $x=10$ mm. Mean concentration shown with dashed line. . . . .	60
3.24	Time series over periods of (a) 5 minutes and (b) 30 seconds at $z=0$ mm, $y=-8$ mm, $x=40$ mm. Mean concentration shown with dashed line. . . . .	61
3.25	Time series over periods of (a) 5 minutes and (b) 30 seconds at $z=0$ mm, $y=-16$ mm, $x=70$ mm. Mean concentration shown with dashed line. . . . .	61
3.26	(a) Normalized mean concentration of bounded plume, with (b) corresponding stream-wise profile at $y=0$ mm. . . . .	62
3.27	Lateral profiles of mean concentration plume at $x=10$ mm, $x=60$ mm, and $x=150$ mm downstream. . . . .	63
3.28	(a) normalized RMS of plume with (b) corresponding centerline profile at $y=0$ mm.	64
3.29	Lateral profiles at $x=10$ mm, $x=60$ mm, and $x=150$ mm. . . . .	64
3.30	Centerline comparison of time-averaged and RMS centerline. . . . .	65
3.31	(a) Intermittency for $C_T = 0.03C_0$ with (b) corresponding centerline profile at $y=0$ mm. . . . .	67
3.32	Lateral profiles of intermittency at $x=0$ mm, $x=60$ mm, and $x=150$ mm. . . . .	67
3.33	Contours of $C_T$ for $\gamma = 0.5$ . . . . .	68
3.34	Contours of $C_T$ for $\gamma = 0.1$ . . . . .	68

3.35	Map of time series locations in relation to each statistical measure. . . . .	69
3.36	Representative time-series of instantaneous normalized concentration for each of the nine locations shown in Fig. 3.35. . . . .	70
3.37	Representative pdfs of instantaneous normalized concentration for each of the nine locations shown in Fig. 3.35. . . . .	71
A.1	Addition of flasks to system to reach maximum saturation . . . . .	81
A.2	Measurements over average counts over 8 minutes to ensure constant seeding . . . .	82
A.3	Vapor pressure vs. temperature, where 1 is the current Pressure ratio using this system. . . . .	83
A.4	Non-dimensional relationship of $C^*$ vs. $t^*$ . . . . .	92
A.5	Specific Non-dimensional relationship of $C^*$ vs. $t^*$ . . . . .	93
B.1	Fluorescence of Acetone vs. Intensity of Laser Take 1 . . . . .	95
B.2	Fluorescence of Acetone vs. Intensity of Laser Take 2 . . . . .	96
B.3	Fluorescence of Acetone vs. Intensity of Laser [32] . . . . .	97
B.4	Fluorescence of Acetone vs. Intensity of Laser [61] . . . . .	97
D.1	Unbounded Data unbinned . . . . .	100
D.2	Unbounded Data 2x2 binned . . . . .	101
D.3	Unbounded Data 4x4 binned . . . . .	101
D.4	Near bed Data unbinned . . . . .	102
D.5	Near bed Data 2x2 binning . . . . .	102
D.6	Near bed Data 4x4 binning . . . . .	102
E.1	Spectral Response of Zyla 4.2+ Camera . . . . .	104
E.2	Comparison of sCMOS 5.5 vs. Zyla 4.2+ . . . . .	106
E.3	532nm Notch Filter Spectra . . . . .	109
G.1	Wind Tunnel Schematic . . . . .	111

G.2	Continuous Release of Acetone into wind tunnel over 25 minutes . . . . .	113
G.3	No Flow in acetone loss over 10 minutes . . . . .	114
G.4	Fitted analytical solution from equation to loss of acetone over time . . . . .	115
G.5	Fitted analytical solution with concentration data over 25 minutes . . . . .	117
G.6	Normalized Beers Law with data . . . . .	118
I.1	Normalized pdfs of the unbounded 30Hz data, with two heads separated and shown in different color. . . . .	123
I.2	Time-series of pixel 1, which is source location of the plume for the 30Hz unbounded data. The two heads are separated and shown in different colors. . . . .	124
I.3	Time-series of pixels 1-4 along the centerline. The two heads are separated and shown in different colors. . . . .	125
I.4	Normalized pdfs of the bounded 30Hz data, with two heads separated and show in different colors. . . . .	126
I.5	Time-series of pixel 1, which is source location of the plume for the 30Hz bounded data. The two heads are separated and shown in different colors. . . . .	127
I.6	Time-series of pixels 1-4 along the centerline. The two heads are separated and shown in different colors. . . . .	128



## Chapter 1

### Literature Review

#### 1.1 Introduction

A scalar is any introduced quantity, such as a chemical, contaminant, or heat that is transported by the ambient flow, and a scalar plume is the resulting temporal and spatial distribution of a transported scalar. The transport of scalar plumes in both air and water is important in engineering and natural sciences. In engineering, water resources engineers study contaminant transport to protect natural resources and drinking water supply. Similarly, atmospheric engineers examine the transport of pollutants from industrial processes to best design air pollution control devices [17]. In the natural sciences, ecologists are interested in both airborne and waterborne odor plumes, with a focus on understanding how animals utilize chemical signaling in plumes for tasks such as source localization.

When a scalar is released, the instantaneous structure downstream is unsteady and spatially complex. The instantaneous structure of a turbulent scalar plume (Figure 1.1) is highly intermittent, with filaments of high concentrations next to areas of no concentration. Due to the filamentous nature of a turbulent plume, it is possible that the instantaneous concentration at a downstream location will greatly exceed the time-averaged concentration at that same location, making it useful to study the instantaneous structure when acute levels of a chemical are of interest. In a contaminant spill the instantaneous concentration field indicates where toxicity thresholds were exceeded, whereas if only a time-average concentration field were examined, it would be impossible to know if instantaneous concentrations remained below a threshold.

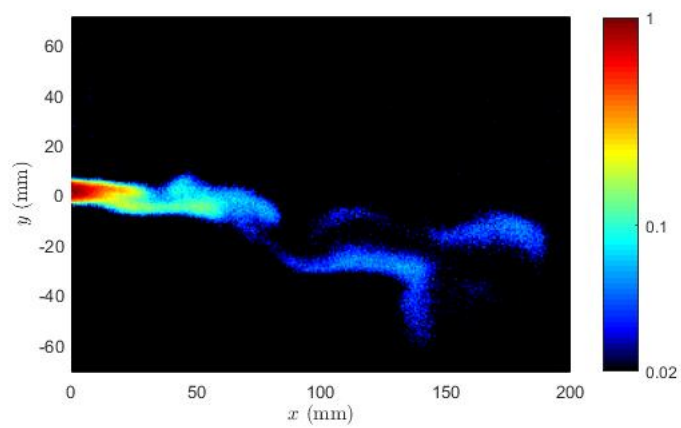


Figure 1.1: Representative instantaneous gaseous plume structure.

The instantaneous plume structure can be averaged in time to provide various different statistical metrics. The simplest is the time-averaged concentration field (Fig. 1.2) , which is the average of instantaneous structures over a long period of time. Time-averaged plumes are typically characterized by smooth concentration gradients, and results in smooth profiles of centerline and lateral cross-sections. Two other common statistical metrics used to examine plume structure are intermittency and intensity. Intermittency is defined how often the scalar concentration is above a threshold, mathematically represented by  $\text{intermittency} = \text{prob} [C \geq C_T]$ . The intensity is the strength of fluctuations in the plume, mathematically calculated by taking the root-mean-square (RMS) of the fluctuations in the plume. These parameters are thought to be important in ecology under the context of animal navigation behavior, although the exact information used to make decisions is still unknown [65].

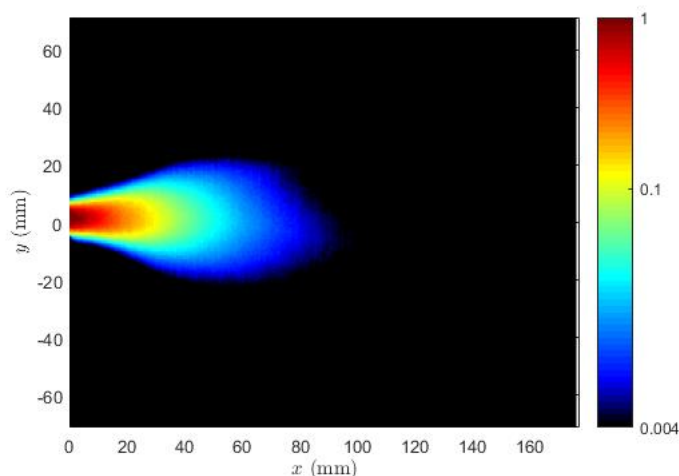


Figure 1.2: Representative mean concentration gaseous plume structure.

## 1.2 Chemical Plumes in Ecology

For millennia organisms have utilized their ability to sense and react to chemicals in their environment to survive. One form of chemical sensing is known as olfaction, the ability to detect odors via chemoreceptors commonly located in the nose, or antennas. In particular, olfaction is

used in a wide range of taxa for navigational purposes [20] to complete vital tasks such as track and locate food sources, mates [43], and avoid predators [40]. Male moths utilize olfaction to navigate turbulent pheromone plumes and locate female moths for mating [34]. Male moths travel upstream, flying against the wind at high velocities, using visual as well as chemical cues to constantly correct their own drift and maintain the most upwind direction possible [43, 11]. Male gypsy moths, as well as other commonly studied species, can successfully locate a pheromone plume from up to 20 meters away in diverse environments of open fields or forests [46]. In aquatic environments, blue crabs [69], whale sharks [19], lobsters [42], and crayfish [41] all exhibit high-level olfactory behavior to locate prey and mates in complex turbulent plume environments. Crabs and lobsters utilize antennule flicking, as well as chemoreceptors on their exoskeleton to detect odors in the ambient environment. The antennules can detect temporal changes in odor concentration through intermittent sampling, while the leg receptors detect a more continuous concentration, by sampling the viscous sublayer on the bed [49].

Olfactory navigation has also been studied in vertebrates (e.g. mice, rats, and dogs) to understand the behavioral and algorithmic phenomena associated with odor localization. Specifically, the ability to recognize and locate mates has long been of interest as it is key to evolution [18]. Experiments done with mice showed that male species can distinguish odors between choosing a female over another a male in a blind Y maze test [7]. Furthermore, mice can not only distinguish odors between male and females, but can individually recognize different female scents up to distances 20 cm away [25]. Dogs have also exhibited the ability to individually differentiate between females that were estrous or not, aiding in their ability to choose a more biological successful mate [2]. Vertebrates are thought to utilize a bilateral sampling method, sniffing an odor through each nostril separately [30]. The loss of one nostril was studied in moles, and shown to decrease the mole's efficiency in locating a source, (e.g. taking longer more indirect paths), although did not prevent the mole from eventually locating the source [12]. Vertebrates are also so successful at tracking odors, we as humans utilize this ability to complete important localization tasks. Most well known is our use of trained dogs to track a scent to find missing persons, locate explosives

in a densely populated area, or detect drug paraphernalia [13]. Other mammals have also been trained to locate specific objects, with rats being frequently used in Cambodia to detect land mines completing the task days faster than a human could [3], as well as truffle pigs which have been used for centuries to locate the culinary truffle [58].

The behavioral mechanisms that animals use to navigate through complex odor plumes, and the aspects of the plume structure that the animals are utilizing are not well understood. Early studies of airborne plume transport used averaged solutions to predict the extent of plume travel and spread from a point source [17]. This simple conceptualization of time-averaged plume distributions was evident in early behavioral studies of insect olfaction, which originally presumed that insects utilize time-averaged concentration gradients to find a source by simply tracking the gradient upstream [6]. For some small insects this hypothesis was validated by studies. Tsetse flies were observed to sample at fixed locations for long enough periods to collect meaningful statistical data before making olfactory decisions [9]. Research in larger animals (e.g. crustaceans and large insects) showed average concentration to be a poor metric for behavioral response [44]. In terrestrial studies, male moths were more successful in locating female moths in intermittent environments, rather than in a smooth ribbon-like plumes [34]. Using mechanically pulsed puffs of odor to create an intermittent plume, male moths were able to locate the source faster, with a more direct flight path at a higher success rate when the plume was intermittent. Conversely, in a continuous ribbon-like plume male moths exhibited slower flying velocities, more turning in the plume, and a lower success rate of finding the source. In aquatic environments it is also the instantaneous structure that provides cues to animals on odor source location [68]. Similar to male moths, blue crabs are more successful in locating prey in intermittent plumes rather than homogeneous plumes [68, 23]. If the plume was released in slow pulses, i.e. long period of time between each release, a decrease in prey localization was observed in blue crabs [23]. Whereas in the continuous release of a turbulent plume crabs were most successful in prey localization [23, 68].

While there have been studies demonstrating that animals can use time-averaged behavior to track odors, others indicate the instantaneous structure is important for source localization.

Invertebrate behavioral studies in moths and crabs helped gain a better understanding of how animals may utilize instantaneous structures of odor plumes, although the exact information they extract from these flows remains unknown. Therefore, to better understand how animals utilize plume content for decision making, we must first understand the physics that drive scalar plume transport.

### 1.3 Physics of Odor Plumes

#### 1.3.1 Governing Equations

Viscous fluid movement is described by the Navier Stokes equations. The 3D advection-diffusion equation couples both advection through the Navier Stokes equations, and diffusion processes describing the relative relationship between the two in the particular system. Advection is a macroscopic process, which describes the bulk mean flow transporting the plume in both laminar and turbulent regimes. Diffusion is a molecular process, which describes the movement of a scalar from high concentration areas to low concentration areas. In understanding these equations it is logical to start in one dimension,  $x$ , with the conservation of mass. In a given control volume the temporal change of concentration is equal to the total flux in the  $x$  direction:

$$\frac{\partial C}{\partial t} = -\frac{\partial q_x}{\partial x} \quad (1.1)$$

where  $C$  denotes concentration, and  $q_x$  denotes the total flux in the  $x$  direction. The total flux is made up of two components: 1. The advective flux,  $uC$ , 2: the diffusive flux  $D\frac{\partial C}{\partial x}$ :

$$q_x = uC - D\frac{\partial C}{\partial x}. \quad (1.2)$$

Substituting equation 1.2 into 1.1 results in the 1D Advection-Diffusion equation for a laminar, incompressible flow:

$$\frac{\partial C}{\partial t} + \frac{\partial}{\partial x}(uC) = D\frac{\partial^2 C}{\partial x^2}. \quad (1.3)$$

Equation 1.3 can be extended to three dimensions, assuming a laminar, incompressible flow and constant diffusivity,  $D$

$$\frac{\partial C}{\partial t} + \frac{\partial}{\partial x}(uC) + \frac{\partial}{\partial y}(vC) + \frac{\partial}{\partial z}(wC) = D \left[ \frac{\partial^2 C}{\partial^2 x} + \frac{\partial^2 C}{\partial^2 y} + \frac{\partial^2 C}{\partial^2 z} \right] \quad (1.4)$$

where,  $v$  denotes velocity in the y-direction, and  $w$  denotes velocity in the z-direction.

Equation 1.4 can be modified to include the effects of turbulence by adding in fluctuations of concentration and velocity in each direction. The fluctuation quantities are denoted with a prime, ', and average quantities are denoted with a bar:

Concentration:

$$C(t) = \bar{C} + c'(t)$$

Velocity in x-direction:

$$u(t) = \bar{u} + u'(t)$$

Velocity in y-direction:

$$v(t) = \bar{v} + v'(t)$$

Velocity in z-direction:

$$w(t) = \bar{w} + w'(t)$$

Substituting these equations into equation 1.4 and taking the time-average of the equation results in:

$$\frac{\partial \bar{C}}{\partial t} + \frac{\partial}{\partial x}(\bar{u}\bar{C}) + \frac{\partial}{\partial y}(\bar{v}\bar{C}) + \frac{\partial}{\partial z}(\bar{w}\bar{C}) = -\frac{\partial}{\partial x} \left[ -D \frac{\partial \bar{C}}{\partial x} + \overline{u'c'} \right] - \frac{\partial}{\partial y} \left[ -D \frac{\partial \bar{C}}{\partial y} + \overline{v'c'} \right] - \frac{\partial}{\partial z} \left[ -D \frac{\partial \bar{C}}{\partial z} + \overline{w'c'} \right]. \quad (1.5)$$

This results in additional turbulent time-averaged terms,  $\overline{u'c'}$ , in each direction. Turbulence is commonly modeled by a gradient flux processes, in which each direction the turbulent flux is equal to the mean gradient:

$$q_{turb_x} = \overline{u'c'} = -\epsilon_x \frac{\partial \bar{C}}{\partial x}$$

$$q_{turb_y} = \overline{v'c'} = -\epsilon_y \frac{\partial \bar{C}}{\partial y}$$

$$q_{turb_z} = \overline{w'c'} = -\epsilon_z \frac{\partial \bar{C}}{\partial z}$$

where  $\epsilon_x$ ,  $\epsilon_y$ , and  $\epsilon_z$  are the turbulent dispersivities in each direction. Substituting these terms into equation 1.5, assuming an incompressible flow, and spatially homogeneous diffusivity, and turbulent dispersivity the 3D-Advection Diffusion equation for a turbulent flow is:

$$\frac{\partial \bar{C}}{\partial t} + \bar{u} \frac{\partial \bar{C}}{\partial x} + \bar{v} \frac{\partial \bar{C}}{\partial y} + \bar{w} \frac{\partial \bar{C}}{\partial z} = (D + \epsilon_x) \frac{\partial^2 \bar{C}}{\partial x^2} + (D + \epsilon_y) \frac{\partial^2 \bar{C}}{\partial y^2} + (D + \epsilon_z) \frac{\partial^2 \bar{C}}{\partial z^2}. \quad (1.6)$$

Equation 1.6 describes the time-averaged behavior of any passive, conservative scalar in a 3D turbulent flow.

### 1.3.1.1 3D Solution for steady state continuous release in laminar flow

Analytical solutions of the 3D advection-diffusion equation for time-averaged, steady state, laminar flows (Equation 1.4) are known for instantaneous and continuous releases of a scalar. Here the the time-averaged solution is found for a continually released scalar away from boundaries, in a laminar flow using Equation 1.4. This solution is relevant for odor releases away from the bed in both water and air.

$$\frac{\partial C}{\partial t} + \frac{\partial}{\partial x}(uC) + \frac{\partial}{\partial y}(vC) + \frac{\partial}{\partial z}(wC) = D \left[ \frac{\partial^2 C}{\partial x^2} + \frac{\partial^2 C}{\partial y^2} + \frac{\partial^2 C}{\partial z^2} \right] \quad (1.7)$$

Assuming steady state, advection only in the x direction, and diffusion only in the y and z directions since advection in x direction  $\gg$  diffusion in x direction we can apply the following mathematical assumptions to equation 1.4:



$$\begin{aligned}\frac{\partial C}{\partial t} &= 0 \\ \frac{\partial}{\partial y}(vC) &= 0 \\ \frac{\partial}{\partial z}(wC) &= 0 \\ D\frac{\partial^2 C}{\partial x^2} &= 0\end{aligned}$$

Making these assumptions, and using  $L$  as a characteristic length of the system, the well known solution of diffusion in two directions is:

$$C(y, z, t) = \frac{M}{4\pi Dt} \exp\left[-\frac{x^2}{4Dt} - \frac{y^2}{4Dt}\right] \quad (1.8)$$

We can assume an infinitesimally small rectangular slice through a 3D domain, with a thickness  $dx$ , moving at a speed of  $U$  such that in the  $x$  direction an infinitesimal change in time is equal to the thickness divided by the velocity,  $U, dt = \frac{dx}{U}$ . A continuously released scalar source can be described as a rate of mass per time as,  $\dot{M} = \frac{Mass}{time}$ . Over the infinitesimally small sliver the change in mass in the  $x$  direction is equal to the input mass per time rate multiplied by the change in time  $dt$ ,  $\dot{M}dt = \dot{M}\frac{dx}{U}$ . And if we assume this small sliver exists in the domain that equation 1.8 does then we know that the  $L$  of the domain is  $dx$ . Substituting in the change in mass yields:

$$C(y, z, t) = \frac{\dot{M}\frac{dx}{U}}{4\pi Dt} \exp\left[-\frac{z^2}{4Dt} - \frac{y^2}{4Dt}\right] \quad (1.9)$$

Note that the  $dx$  will cancel and we can substitute in  $t = \frac{x}{U}$  to equation 1.9 to yield the 3D advection diffusion steady state solution for a continuous scalar source:

$$C(x, y, z) = \frac{\dot{M}}{4\pi Dx} \exp\left[-\frac{Uz^2}{4Dx} - \frac{Uy^2}{4Dx}\right] \quad (1.10)$$

### 1.3.1.2 Near Bed 3D Solution for a continuous scalar source

This solution describes a steady-state concentration distribution near a boundary that exists at  $z=0$ . To derive this solution we will first start with a general boundary solution case, which utilizes image sources,  $C_{image}$  across the defined boundary.

$$C(x, y, z) = \frac{\dot{M}}{4\pi Dx} \exp \left[ -\frac{Uz^2}{4Dx} - \frac{Uy^2}{4Dx} \right] + C_{image} \quad (1.11)$$

If the release is distance  $L$  away from the boundary in the  $y$ -direction, then an image source can account for the boundary by being added in at  $-L$ . This results in the following equation for  $C_{image}$ :

$$C(x, y, z)_{image} = \frac{\dot{M}}{4\pi Dx} \exp \left[ \frac{-U(z + 2L)^2}{4Dx} - \frac{Uy^2}{4Dx} \right] \quad (1.12)$$

Here  $L$  is an arbitrary distance and thus can be used for any boundary case, however in the case of near bed, the release is on the bed therefore  $L=0$ . This results in a simplification of  $C_{image}$  as the exact same equation as original  $C(x,y,z)$  in equation 1.9. Therefore the solution for near bed is:

$$C(x, y, z) = \frac{\dot{M}}{4\pi Dx} \exp \left[ 2 \left[ \frac{-Uz^2}{4Dx} - \frac{Uy^2}{4Dx} \right] \right] \quad (1.13)$$

### 1.3.2 Non-dimensional parameters for scalar plume transport

While the advection diffusion equation provides analytical solutions for specific flow scenarios, the Navier Stokes equations describe the fluid movement in full detail. These equations are only solvable through numerical modeling under a variety of mathematical assumptions about the flow. However, they can still provide insight into the relative mechanisms at play in a flow, and thus by non-dimensionalizing the Navier Stokes equations we can arrive at an important ratio called the Reynolds Number.

### 1.3.2.1 Non-dimensional Navier Stokes Equation

The dimensional Navier Stokes Equations are as follows: Continuity:

$$\nabla \cdot \vec{u} = 0 \quad (1.14)$$

$$\frac{\partial \vec{u}}{\partial t} + \vec{u} \cdot \nabla \vec{u} = -\frac{1}{\rho} \nabla p + \nu \nabla^2 \vec{u} + \vec{g} \quad (1.15)$$

Equation 1.15 can be non-dimensionalized by substituting in new non-dimensional variables:

$$\begin{aligned} \vec{u}^* &= \frac{\vec{u}}{U} \\ \vec{x}^* &= \frac{\vec{x}}{L} \\ t^* &= \frac{t}{T} \\ p^* &= \frac{p}{\Delta p} \\ \nabla^* &= L \nabla \\ (\nabla^*)^2 &= L^2 \nabla^2 \end{aligned}$$

Now substituting in these non-dimensional variables we get the following equation:

$$\frac{U}{T} \frac{\partial \vec{u}^*}{\partial t^*} + \frac{U^2}{L} \vec{u}^* \cdot \nabla^* \vec{u}^* = -\frac{\Delta p}{\rho L} \nabla^* p^* + \frac{\nu U}{L^2} (\nabla^*)^2 \vec{u}^* + \vec{g} \quad (1.16)$$

If we divided each term through by  $\frac{U^2}{L}$  we will get a non-dimensional Navier Stokes with a  $\frac{1}{Re}$  in front of the viscous term as seen below:

$$\frac{L}{UT} \frac{\partial \vec{u}^*}{\partial t^*} + \vec{u}^* \cdot \nabla^* \vec{u}^* = -\frac{\Delta p}{\rho U^2} \nabla^* p^* + \frac{\nu}{UL} (\nabla^*)^2 \vec{u}^* + \frac{\vec{g}L}{U^2} \quad (1.17)$$

$$\frac{L}{UT} \frac{\partial \vec{u}^*}{\partial t^*} + \vec{u}^* \cdot \nabla^* \vec{u}^* = -\frac{\Delta p}{\rho U^2} \nabla^* p^* + \frac{1}{Re} (\nabla^*)^2 \vec{u}^* + \frac{\vec{g}L}{U^2}. \quad (1.18)$$

The Reynolds number is ratio of inertial forces,  $UL$  to viscous forces,  $\nu$ , with the magnitude of the number indicating which force is dominating in the particular flow. The Reynolds number can be classified into laminar and turbulent regimes for specific scenarios. One commonly used

classification is in pipe flow where the flow is considered laminar for  $Re < 2100$  and turbulent for  $Re > 2100$ . However, in general  $Re \gg 1$  is thought to be a turbulent flow, with the intensity of turbulence cascading towards lower Reynold's numbers and thus less turbulent as the number decreases.

### 1.3.2.2 Non-dimensional advection-diffusion equation

Following a similar process of non-dimensionalization, the 1D Advection diffusion equation can be non-dimensionalized such that the group of constants in front of the advection term emerge as the Peclet number (Pe). This number is the ratio of advective to diffusive time scales for a transport of a particle. Starting with the 1D-advection diffusion equation:

$$\frac{\partial C}{\partial t} + u \frac{\partial C}{\partial x} = D \frac{\partial^2 C}{\partial x^2} \quad (1.19)$$

Equation 1.1 can be non-dimensionalized by substituting in new non-dimensional variables:

$$\begin{aligned} u^* &= \frac{u}{U} \\ x^* &= \frac{x}{L} \\ t^* &= \frac{t}{T} \\ C^* &= \frac{C}{C_{max}} \end{aligned}$$

Resulting in:

$$\frac{C}{T} \frac{\partial C^*}{\partial t^*} + \frac{UC}{L} u^* \frac{\partial C^*}{\partial x^*} = \frac{DC}{L^2} \frac{\partial^2 C^*}{\partial (x^*)^2} \quad (1.20)$$

Now to compare the advection to diffusion timescales, the group of variables in front of the diffusivity term,  $\frac{DC}{L^2}$  can be divided by the group of variables in front of the advection term,  $\frac{UC}{L}$ . This results in a constant in front of the temporal term, the unsteadiness coefficient, value of 1 in front of the advection term, and the inverse Peclet number in front of the diffusivity term  $\frac{D}{UL}$ ,

$$\frac{L}{TU} \frac{\partial C^*}{\partial t^*} + u^* \frac{\partial C^*}{\partial x^*} = \frac{D}{UL} \frac{\partial^2 C^*}{\partial (x^*)^2} \quad (1.21)$$

$$\frac{L}{TU} \frac{\partial C^*}{\partial t^*} + u^* \frac{\partial C^*}{\partial x^*} = \frac{1}{Pe} \frac{\partial^2 C^*}{\partial (x^*)^2} \quad (1.22)$$

When  $Pe \ll 1$  diffusion dominates as the main transport of a particle, and when  $Pe \gg 1$  advection dominates. Therefore, this ratio is helpful for understanding which mechanism, advection or diffusion, is driving the flow.

### 1.3.2.3 Schmidt Number

Encompassing both the Peclet and Reynolds number, the Schmidt number compares the two, and the final ratio is viscosity of the fluid or momentum diffusivity, compared to diffusivity of the scalar. The Schmidt number controls the amount of diffusivity present in a system, with a value close to 100 in water and 1 in air, this indicates diffusion plays a larger role in air than it does in water for a scalar.

$$Sc = \frac{Pe}{Re} = \frac{\nu}{D}$$

### 1.3.3 Experimental Studies of Plume Structure

Detailed numerical models of plume structure are limited by computational power, therefore a majority of what is known about scalar plume structures has been found experimentally. The majority of these experiments have been done in water using organic fluorescent dyes and in air using tracers detected via ionization. In water, the most relevant technique is aqueous PLIF, which releases organic dyes that are fluoresced by a laser sheet, and images of the instantaneous structure are captured via high speed scientific camera for analysis [14]. Aqueous PLIF uses non-intrusive visualization and quantification of concentration fields in the flow. In air, plumes are most commonly measured via the photoionization technique. A photoionization detector can measure single point concentration values at a high temporal resolution, often emulating that of an insect's antenna [35]. The results provide a high-resolution temporal history of the odor signal, with information on the intermittency of the plume, and the slope and duration of the odor burst detected. Although techniques differ, the physics of plume transport are the same in both air and water which have led to general conclusions about average and instantaneous turbulent plume structure.

Found in both air and water plume environments the instantaneous structure of concentration fields consists of high concentration filaments or, commonly called in entomology studies, “bursts”, next to ambient air or water having non-detectable concentration, creating sharp concentration gradients within the plume [15, 66, 24, 44]. In air these gradients are much smoother due to the lower Schmidt number of air ( $Sc=1$ ) than in water ( $Sc=100$ ), which indicates diffusion plays a larger role in scalar transport in air than it does in water. Similarly, downstream of the source release, the temporal signal of concentration is detected as short bursts of concentration commonly present 10-20% of the time depending upon location [24]. These filamentous pockets of high concentration are present due to the turbulent vortices in the flow, which aids in stretching and stirring the scalar increasing the average size of the plume [28]. However, it is diffusion that will ultimately bridge the gap between stirring and mixing to create a homogeneous plume downstream of the source, thus increasing the amount of time needed for a plume to transition from coherent turbulent structures to a homogeneous mixed plume [28]. The filamentous structures of turbulent plumes are found to be highly dependent upon on flow and release conditions, such as proximity to boundaries or in different physical environments (e.g. field or forest) [66, 46]. In releases near the bed, an increased homogeneity of the plume is observed due to the more turbulent mixing of being close to a boundary and the the plume being ”trapped” in the viscous sublayer [67]. Conversely, plumes released away from boundaries were found to have structure persist up to 10m downstream of the source due to the low molecular diffusion of the scalar [11]. Other factors such as relative velocity to surrounding velocity can also change downstream plume structure. For instance, an increase in Reynold’s number, in relation to the nozzle velocity release versus the ambient flow, ( $Re=0$  to  $Re=1816$ ), the more homogeneous the plume becomes, as this increase in  $Re$  enhances mixing and stirring in the plume [67]. Our current knowledge of instantaneous plume structure comes from the experimental measurement techniques used in the cited literature to extract this information. While we know the physics of scalar plumes in turbulent environments to be the same in both air and water, the same methodologies of measuring scalar turbulent plumes using PLIF have not yet been employed for the purpose of studying plume structure in air.

## 1.4 Acetone Planar Laser Induced Fluorescence

### 1.4.1 Origins of Gaseous PLIF

Gaseous PLIF is a non-intrusive measurement technique used to capture a series of instantaneous snapshots under different scalar release conditions in gaseous mediums. Gaseous PLIF follows all similar techniques to that of aqueous PLIF, by creating a planar laser sheet and releasing a fluorescent tracer dye under varying flow conditions.

Gaseous PLIF was first implemented in the 1970s as a method to visualize high speed combustion flow fields, internal combustion (IC) flows, turbulent flame jets, and reaction kinetics in combustion flows [21, 47]. Since these techniques focused on combustion flows, many compounds naturally present in the flow, nitric oxide (NO), and carbon monoxide (CO), also naturally fluoresced making them logical and convenient tracers to be used in these studies [27, 55]. Although convenient, these tracers are quite dangerous to human health and safety, and a need for a safer alternative arose. Under a grant by the US Air Force, the Ronlad Hanson group at Stanford began to evaluate possible alternatives to be used in scalar field studies. When searching for the best alternative several factors were taken into consideration. The tracer must be passive and non-reactive, easily seeded into a gaseous flow, safe to human health for those using it directly as well as safe for the lab and building this method is being used in, and preferably inexpensive.

In 1992 a student working for Dr. Ronald K. Hanson, Antonio Lozano, published the paper "Acetone: a tracer for concentration measurements in gaseous flows" explaining the benefits of using acetone as a tracer to measure scalar concentration fields in gaseous flows [32]. In this paper he describes acetone as having superior ability to be seeded into flows at high concentrations due to its high vapor pressure at room temperature. Acetone is also a convenient choice since it is already ubiquitous in most laboratories across the world, its dangers and toxicity effects are relatively low and well known, and it has a very low oxygen quenching effect, which is vital for images in slower flows. A similar compound biacetyl was also being explored at this time, as it had been previously used in some combustion flow studies [29], but Lozano found acetone to be superior in almost every

parameter described.

#### 1.4.2 The Acetone PLIF Technique

In general, the acetone PLIF technique is set up similarly to other PLIF techniques with the three main components for success: 1. fluorescent tracer, 2. laser, and 3. scientific camera. Consistent throughout all published acetone PLIF studies, acetone vapor is generated on site at the time of the experiments as it needs to be created in equilibrium with liquid acetone. Acetone laden flow is delivered to a constructed flow facility via compatible, (most commonly vinyl), tubing at a desired flow rate. The gaseous mixture is then released under controlled conditions into the testing facility and the flow is fluoresced with a UV laser. Acetone is excited under a variety of wavelengths as seen by the excitation spectrum in Fig. 1.3. The most commonly used excitation wavelengths are 248nm, 266nm, and 308nm pulsed lasers. However, in order to get the most excitation taking into account energy available in each laser, as well as efficiency of excitation at each wavelength, 266nm was found to have maximum excitation for acetone vapor [32]. After being excited by 266nm wavelength a high speed scientific camera, most commonly a 512x512 CCD camera, was used to capture instantaneous still frames of the flow. After acetone was published as a viable tracer for gaseous PLIF, many groups interested in studying combustion flows and other IC engine fluid mechanics adopted the acetone PLIF method. Similar to previous papers using gaseous PLIF, studies using acetone PLIF were published on high speed, high Reynolds number combustion jets flows at small millimeter scales [70]. Literature using acetone PLIF was also heavily focused on spray flows [51, 50, 52], temperature flow fields [60, 59], and used for 3D visualization by combining acetone PLIF and Rayleigh scattering techniques [57].

#### 1.4.3 Relevant Plume Studies

The method of acetone PLIF was used mostly by a community of researchers whose main focus was combustion and jet engine studies. However, a few studies published plume like data, with an isokinetic releases at high Reynolds numbers. One of the most notable plume like data



involved using an isokinetic release to minimize shear and compute a commonly used turbulent model variable  $C_d$ , which is the ratio of timescales for mechanical energy dissipation to scalar energy dissipation [37, 38]. The Markides group published numerous papers using the same plume-like dataset, analyzed using different statistical methods for their model validation. Ultimately they were successful in determining a realistic value of  $C_d$ , with their focus on statistical average behavior of the mixing ratios near the source release. Another experiment utilized acetone PLIF to calculate mass entrainment rates for buoyant plumes and jets in relation to pool fires, hot jets, fuel leaks, and diffusion flames. This study used both PLIF and Particle Image Velocimetry (PIV) to analyze different puffing frequencies to calculate mass entrainment rates, again focusing on averaged entrainment rates [5].

## 1.5 Relationship of present work to previous studies

Although dozens of studies have been published using acetone PLIF as method to quantitatively measure gaseous flow structures, scalars, and other variables, very little literature exists for using it study low velocity isokinetic instantaneous plume structure over large spatial environments. Papers that study similar plume-like releases focus on specific statistical variables such as model coefficients and mass entrainment rates. Therefore, the goal of this thesis is to help bridge the gap between current knowledge on odor plumes in water and air, by utilizing and adapting an established method of acetone PLIF. Furthermore, to adapt this method and ensure its successful, capture two baseline datasets using the method. a

## Chapter 2

### Methods

#### 2.1 Overview

In a gaseous plume PLIF experiment, there are two major components: the physical flow facility which allows flow control and conditioning, and the PLIF system required to fluoresce and capture the data. The physical flow facility is a wind tunnel, which has contractions, turbulence generating grids, and a fan controlling the ambient flow designed to meet desired flow rates and conditions. The PLIF system consists of a fluorophore, acetone, which is fluoresced by an appropriately matched laser, 266nm, and a scientific camera to capture high speed images in the flow facility. These components are pictured in Fig. 2.1 and discussed more in the subsequent sections.

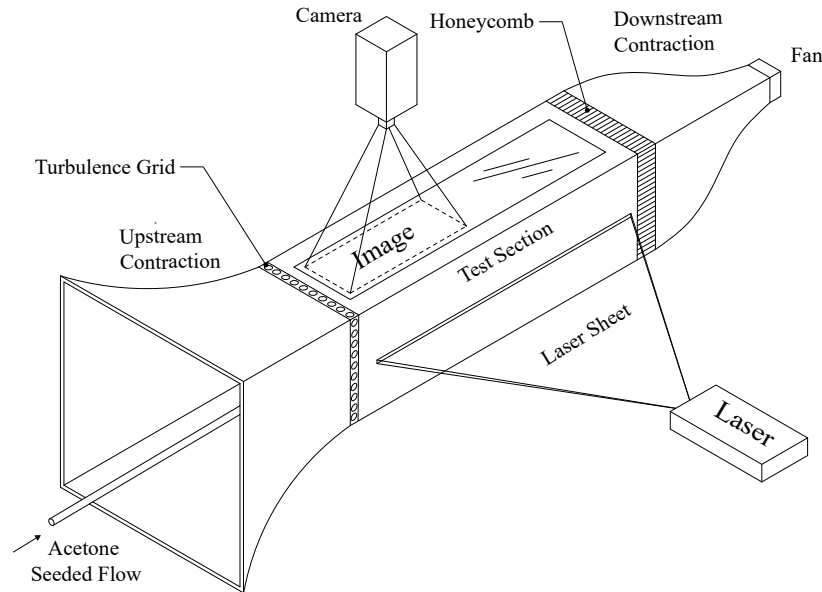


Figure 2.1: Overview of experimental apparatus including the wind tunnel and PLIF components.

## 2.2 Flow Facility

### 2.2.1 Wind Tunnel Description and Layout

The wind tunnel used in these experiments (Figure 2.2) was built to test a newly adapted gaseous PLIF method for capturing plume data. Because of this, the wind tunnel was not constructed for longevity but instead for collecting baseline data in a relatively short period of time. The design and set up used in these experiments has laid the framework for a future more robust wind tunnel (Section 4). The wind tunnel was built out of black 4.7625 mm foam core due to its easy manipulation into sturdy curved and straight structures. In total, the length of the wind tunnel is 2 meters long, with three individual components (labeled in Fig. 2.2) of varying cross-sectional areas:

- (1) Upstream contraction

(2) Test section

(3) Downstream contraction

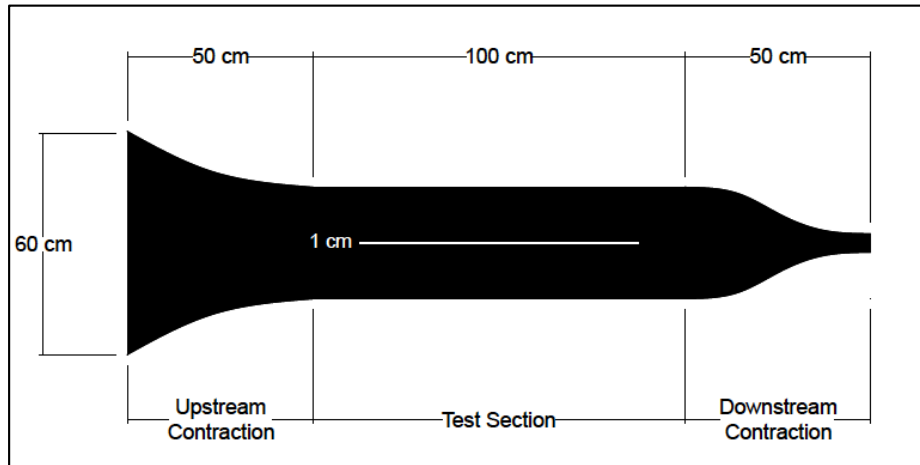


Figure 2.2: Exterior dimensions of the wind tunnel.

The first component, the upstream contraction, is shown with more detailed dimensions in Figure 2.3. The upstream contraction works out perturbations from the ambient air, and conditions the incoming flow to be homogeneous. A 4:1-6:1 cross-sectional area ratio is recommended by JIAA [4] for low-speed wind tunnels ( $\leq 1$  m/s), and was used in the construction of the upstream contraction, which decreased in area from  $3600 \text{ cm}^2$  to  $900 \text{ cm}^2$  as seen in Fig. 2.3.

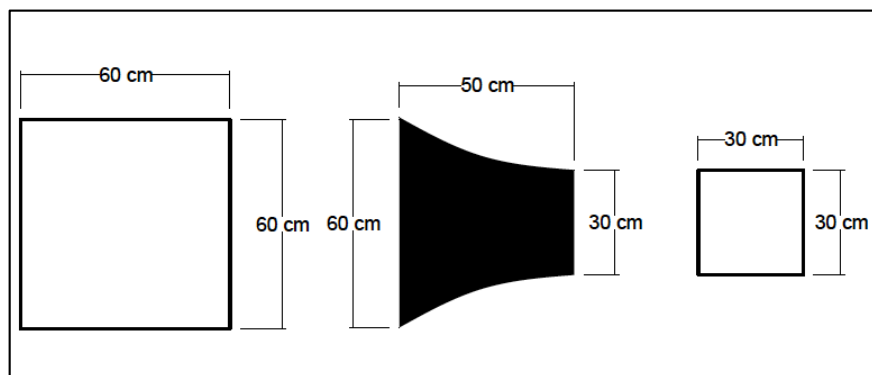


Figure 2.3: Detail of upstream contraction.

Where the upstream contraction and test section meet, there is a uniformly spaced turbulence grid which induces homogeneous isotropic turbulence in the test section [53]. The grid is 30x30

cm<sup>2</sup> with 6.35 mm diameter circular rods, and a mesh size of 25.4 mm (Fig. 2.4). A typically reported ratio for turbulence grids is the mesh size:diameter with a common value of 5, and here is 4. Another quantification of the mesh is to use both the Reynolds number for the Mesh and Diameter, which can provide info on the isotropic nature of the turbulence. They are computed as follows:

$$Re_{mesh} = \frac{UM}{\nu} = \frac{0.05m/s * 0.0254m}{15.11 * 10^6} = 84 \quad (2.1)$$

$$Re_{mesh} = \frac{UD}{\nu} = \frac{0.05m/s * 0.0254m}{15.11 * 10^6} = 20 \quad (2.2)$$

Typical values for Reynolds Mesh numbers range from 400-100,000 [26]. The higher the value of the Reynolds number, the more isotropic the turbulence is believed to be. Another measure for turbulence grids is the solidity of the grid, defined as the following ratio

$$\sigma = \left(\frac{M}{D}\right)\left(2 - \frac{M}{D}\right) = 0.011 \quad (2.3)$$

The solidity needs to be below 0.5 to produce isotropic turbulence. Typical values range from 0.3-0.5 [26]. After the turbulence grid is the 1 m long test section with a constant cross-sectional area of 900 cm<sup>2</sup> (Fig. 2.5). The test section is where data was collected, therefore optical access for the camera and laser was needed in the final design. The top of the test section was constructed out of 4.7625 mm clear glass for camera access and both sides of the test section have 1 cm slits for laser sheet entry and exit.

Between the test section and downstream contraction there is a 15 cm thick piece of honeycomb, which eliminates turbulence produced from the swirling of the fan by straightening the flow and reducing lateral velocity. To ensure the turbulence has been completely minimized, the recommended length:diameter ratio of the honeycomb is 6:1 [4], and a ratio of 15:1 was used in this set up. The final component, the downstream contraction (Fig. 2.6), is 50 cm in length with a 36:1 area contraction, decreasing from 900 cm<sup>2</sup> to 25 cm<sup>2</sup>. This contraction exists solely to fit the small (5cmx5cm) fan (Sunon KDE S.N 1205PFB2-8), that is used to pull air through the tunnel at the chosen specified maximum flow rate of 4340  $\frac{\text{cm}^3}{\text{s}}$  at 12V. The fan is powered by a power supply (Tekpower S.N. TP30020E), which delivers a constant 12V to the fan, thus a constant flow rate of

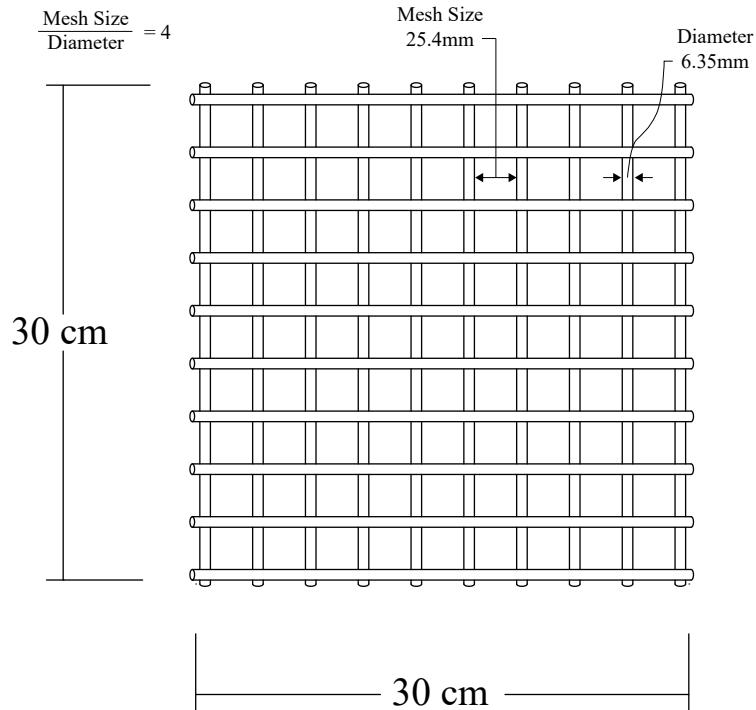


Figure 2.4: Uniform turbulence grid diagram with relevant length scales and mesh:diameter ratio.

$4340 \frac{\text{cm}^3}{\text{s}}$  throughout the wind tunnel. In the test section the fan is pulling air through at a flow rate of  $4340 \frac{\text{cm}^3}{\text{s}}$ , which when using the  $900 \text{ cm}^2$  area results in a  $4.8 \frac{\text{cm}}{\text{s}}$  ambient velocity in the wind tunnel. This velocity was tested with ad-hoc smoke visualization to validate the velocity. An incense was lit in the tunnel and tracked over 10 second intervals. Consistent results matched the calculated  $4.8 \frac{\text{cm}}{\text{s}}$  velocity closely.

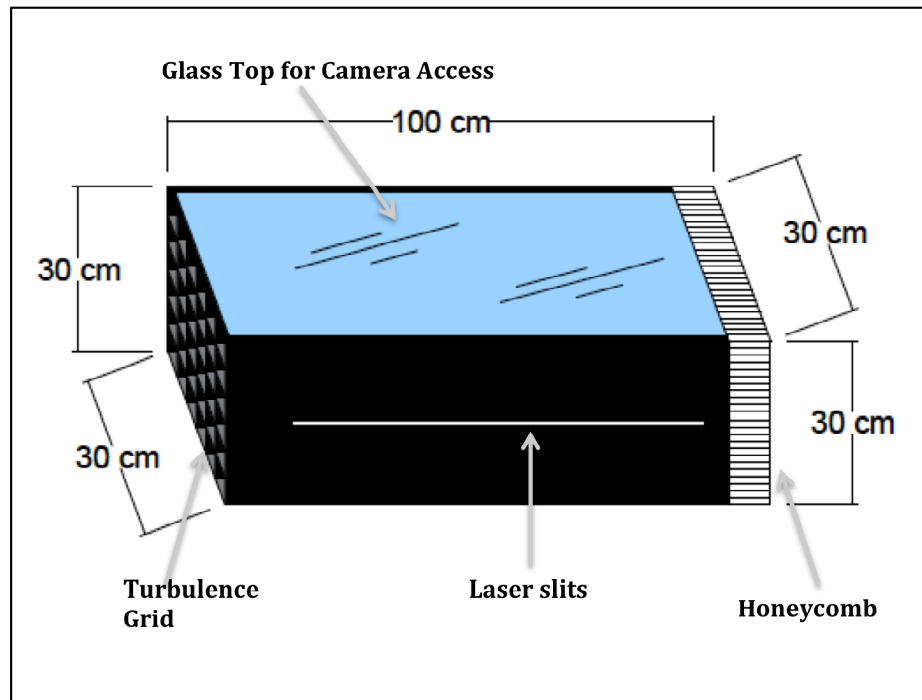


Figure 2.5: Detail of test section.

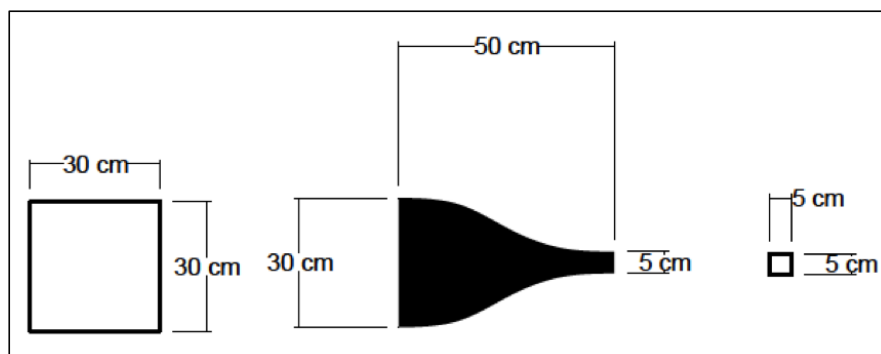


Figure 2.6: Detail of downstream contraction.

## 2.3 PLIF System Components

### 2.3.1 Acetone Vapor Generation

The generation of a vapor is a chemical process that depends on pressure, temperature, and chemical equilibrium. To create acetone vapor, a closed flask of liquid acetone (Fisher Chemical A 18-4) and vapor are given enough time to come to equilibrium. For acetone this process occurs almost instantaneously, as vapor pressure of acetone is relatively high compared to other liquids at room temperature (acetone = 185 mmHg at 20C, while water = 17.5 mmHg at 20C). In Fig. 2.7, a closed flask is pictured with two tubes, which allow entry and exit of a constant, controlled gaseous flow. The flowing mixture enters the flask at the bottom of the liquid acetone, forcing existing saturated acetone vapor to exit the flask via the tube to the wind tunnel, allowing new liquid molecules to evaporate and replace the leaving vapor to maintain equilibrium. The amount of acetone vapor available to be seeded in a flow is limited by a theoretical maximum, which is dependent upon the ideal gas law, vapor pressure of acetone, and temperature of the flask.

To calculate the amount of vapor that can be seeded into a gaseous flow, Raoult's Law of Partial Pressures relates the ratio of partial pressure to atmospheric pressure to that of mole fractions in a gaseous mixture.

$$\frac{X_{acetone}}{X_{total}} = \frac{P_{acetone}}{P_{total}}$$

where  $P_{acetone}$  is the vapor pressure of acetone, and  $P_{total}$  the total pressure in the system. The tubing connected to the flask is open to the atmosphere  $P_{total}=630\text{mmHg}$  (atmos. press. at 5430ft and 20 C). The vapor pressure of acetone at 20 C is 185 mmHg. Substituting these values into Raoult's law, the maximum percentage of acetone that can be seeded into a gaseous flow is:

$$\frac{X_{acetone}}{X_{total}} = \frac{185\text{mmHg}}{630\text{mmHg}}$$

$$\frac{X_{acetone}}{X_{total}} = 0.29 = 29\%.$$



However, 29% is a theoretical value if the efficiency ( $\eta$ ) of seeding was assumed to be  $\eta = 1$ . It is more realistic to assume an efficiency of  $\eta = 0.9$ , which is commonly used in chemistry calculations. This results in the maximum seeding percentage, denoted as S, to be:

$$S = 29\% * \eta$$

$$S = 29\% * 0.9$$

$$S = 26\%$$

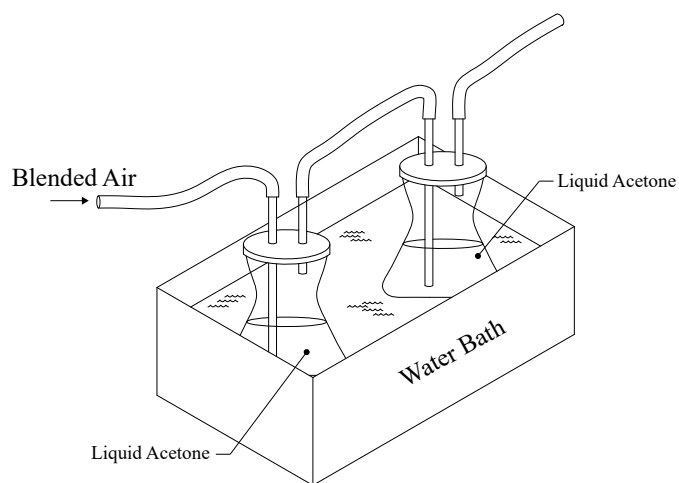


Figure 2.7: Flow diagram of acetone vapor, with flow direction indicated by arrows.

### 2.3.1.1 Ensuring constant and maximum seeding acetone into flow

To ensure continual and constant maximum seeding of acetone vapor, two liquid acetone flasks were placed in serial to seed the flow. The first flask seeds a majority of the flow with acetone, but since this is a dynamic system that actively removes acetone vapor from the flask when seeding, it will fluctuate between being at equilibrium to being slightly below equilibrium. The second flask will then seed any of the remaining flow that has not reached the maximum seeding fraction after traveling through the first flask. In the second flask, the change in equilibrium state is assumed negligible since only a small amount of acetone vapor leaves the flask. The assumption that the maximum seeding fraction is being constantly met in the flow with two flasks was validated from testing the average counts in the core of jet flow, and increasing the number of flasks for each test. More details are described in Appendix A.1. In conclusion, after the addition of a second flask no significant increase to mean count signal was observed. Additionally, little variation in the average count number was observed for each flask, validating a constant maximum seeding rate in the system. This is consistent with other acetone PLIF studies [60, 59, 5] where two flasks were used in the experimental set up to reach maximum seeding level.

In equilibrium, the acetone vapor is evaporating from the liquid into the headspace, which causes a temperature drop due to evaporative cooling. In addition to the evaporative cooling, if acetone is seeded at a higher temperature than the ambient air of which it is flowing through, condensation will occur. Keeping both of these temperature dependent factors in mind, the two-beaker system was submerged in a constant temperature bath at 22 C. 22 C was chosen after trial and error as a temperature that balanced evaporative cooling to keep the flasks at room temperature and didn't produce condensation in flow lines. Vapor pressure is directly proportional to temperature, such that an increase in temperature results in an increase of vapor pressure. Since the maximum seeding percentage is dependent upon vapor pressure, in future studies it may be worthwhile to increase the temperature as this would increase the maximum seeding percentage in the flow, therefore increasing signal in the data. This is discussed in more detail in Appendix A.2.

### 2.3.1.2 Density Correction

In low velocity plume experiments it is necessary to have a neutrally buoyant plume so flow is not driven by gravity, and so the flow remains aligned with the laser sheet and camera for accurate image capturing. Acetone vapor is reported to have a density of  $2.00 \frac{\text{kg}}{\text{m}^3}$  (solved in detail in Appendix A.3), which is roughly twice the density of air. To counteract the heavy acetone vapor, air was blended with helium before entering the acetone flasks for seeding. This ensured a neutrally buoyant mixture exited the flasks and was delivered to the wind tunnel. Mixture percentages of air and helium are solved below.

$$\rho_{mix} = (1 - S) * (x * \rho_{helium} + (1 - x) * \rho_{air}) + S * (\rho_{acetone})$$

where S is the maximum seeding percentage of acetone into the flow, (1-S) will be the total proportion of air and helium to the mixture, and solving for x will yield the appropriate mixture percentages of helium and air. The following densities are all calculated in detail in Appendix A.3, and reported here with other known variables:  $\rho_{helium} = 0.138 \frac{\text{kg}}{\text{m}^3}$   $\rho_{air} = 1.001 \frac{\text{kg}}{\text{m}^3}$   $S = 0.26$

Solving for x in the above equation:

$$1.001 = (1 - 0.26) * (x * 0.138 \frac{\text{kg}}{\text{m}^3} + (1 - x) * 1.001 \frac{\text{kg}}{\text{m}^3}) + 0.26 * (2.00 \frac{\text{kg}}{\text{m}^3})$$

$$x = 0.41$$

which is 41% helium and (1-x)= 0.59, 59% of air blended before entering the acetone flasks.

### 2.3.2 Delivery of Acetone to Wind Tunnel

The gaseous mixture was delivered to the wind tunnel under isokinetic (release velocity = ambient velocity) conditions. A plume velocity of 5 cm/s was chosen, and all components of the delivery system were designed to meet this specification. The ambient wind tunnel velocity determined in section 2.2.1 was  $4.8 \frac{\text{cm}}{\text{s}}$ . In order for the release velocity to match the ambient

velocity, vinyl tubing (resistant to acetone) with an inner diameter of 0.9525 cm, and compatible Dwyer mass flow controllers (MFC) (air MFC (Model: VFA-21-BV) and helium MFC (Model: RMA-13-SSV)) were used to control flow rates. Using the area of the vinyl tubing, the required flow rate to match the ambient velocity was calculated to be  $3.33 \frac{\text{cm}^3}{\text{s}}$  in the tube release flow rate.  $3.33 \frac{\text{cm}^3}{\text{s}}$  was then used as the total flow rate for determining the appropriate flow proportions of the air and helium mixture. Setting the flow rates to  $1.9 \frac{\text{cm}^3}{\text{s}}$ , and  $1.4 \frac{\text{cm}^3}{\text{s}}$  for air and helium respectively, resulted in a  $4.7 \frac{\text{cm}}{\text{s}}$  release velocity. This process is depicted in Fig. 2.8.

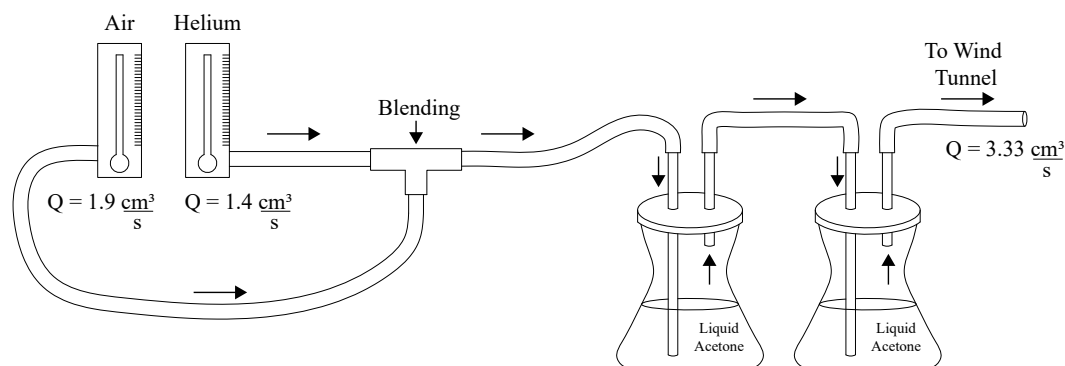


Figure 2.8: Entire flow diagram of blending process, with flow direction labeled indicated by arrows.

### 2.3.3 Acetone Safety

Acetone is a highly flammable compound in both liquid and vapor states. To ensure an explosive environment is not created in the lab or wind tunnel is therefore vital for safety of the students working in the lab and building. Calculations on acetone explosive limits, indicate conditions in the lab are well below explosive the explosive limits of acetone vapor. This is detailed more in Appendix A.4.

## 2.4 PLIF System Components

### 2.4.1 Nd:YAG doubled frequency UV Laser

Due to current market availability of high energy UV lasers, the best option was to upgrade an existing pulsed 532 nm Quantel Evergreen laser (S.N. 30266) to produce a wavelength of 266 nm at 35 mJ per pulse. Maximizing energy per image is important for maximizing signal in the data, however it is also important not to saturate the fluorophore as this will produce unreliable results. The 35 mJ per pulse energy in the Quantel Evergreen laser was determined to be within linear regime of fluorophore excitation [14], thus there was no concern with saturating the acetone vapor (Appendix B). Consequently, once it was known that the laser energy was not close to saturation of the fluorophore, the possibility of purchasing a UV laser with higher energy output was researched. However, after careful calculations it was determined that no other UV lasers on the market produced as much energy per image as the upgraded Evergreen 532nm. This decision is detailed more in Appendix C. To trigger the laser, BNC cables are attached to a PC machine equipped with highly detailed software to manually input framing rates (0-30Hz), timing delays, and power levels. This software allows ease of control over synchronization of the laser and camera to capture images at desired framing rates.

To create a thin light sheet for data collection, speciality UV optics from TSI Inc. were used. A 1 mm thick sheet covered the large field of view (35 cmx35 cm). To create the sheet, a series of optics were mounted directly onto the laser head. First, a dichroic mirror was attached directly to the laser head, which diverted any residual 532nm light left after the upgrade from entering the sheet. However, approximately 1-2% of the 532nm still remained in the sheet after the dichroic, so a 532nm notch filter (Edmund Optics S.N. 86-130 (Appendix F.3)) filtered out any remaining 532nm light detected by the camera. After the dichroic mirror, three more lenses were mounted in the following order (Figure 2.11): 1. collimator focusing lens to focus the sheet, 2. -25mm cylindrical lens to spread the beam into a sheet, 3. -15mm cylindrical lens to spread the sheet thinner. In theory, the thickness of the sheet should create an approximately equal sized voxel with the pixels

in the image, such that the thickness dimension is equal to a pixel length and width on the image. The images used in the analysis were originally 2048x2048 pixels binned 4x4 to 512x512 pixels, over a 35x35 cm<sup>2</sup> area with a final voxel volume of 0.7 mmx0.7 mmx1 mm. Since binning was done to an extensive amount, it was concluded no structure was lost due to sheet thickness (See Appendix D for more information on binning).

### 2.4.2 Camera

Acetone PLIF is signal limited with counts orders of magnitude below the saturation limit on a 16-bit camera. Because of this, any measures to increase signal and thus increase signal-to-noise ratio (SNR) were taken. SNR is important when analyzing images to determine if signal is meaningful data or noise, the higher the SNR the more confidence exists in the data. The camera has most control over SNR and can be maximized in a variety of ways, starting with the choice of camera. To capture high speed images in a low light environment a highly sensitive scientific camera is required. The Andor Zyla 4.2+ camera was designed specifically to capture high resolution images in low light environments (Appendix E.1). The Zyla 4.2+ has a 82% quantum efficiency, 33,000:1 dynamic range, and state of the art USB 3.0 data transfer at 53 fps. The Zyla 4.2+ has an extremely low readout noise of 0.9e-, allowing high signal-to-noise (SNR), and a global shutter feature to reduce dead time and take images with no spatial distortion. Therefore, taking into account these capabilities the Zyla 4.2+ was chosen as the best camera for the experimental conditions.

The Zyla 4.2+ was tested with two other cameras before determining it was the best for these experimental conditions. First, it was compared to an existing camera in our laboratory, sCMOS 5.5, and second it was compared to another Andor Camera, the EMCCD Ultra 888. Results indicated that under the exact same environmental conditions the Zyla 4.2+ provided the highest signal detection, with highest SNR. These comparisons are documented in full detail in Appendix E.2.

To maximize light in the image (maximize SNR), the fastest lens available on the market, a

f/0.95 Schneider lens, was used on the Zyla 4.2+. A small f-stop number (such as f/0.95) indicates a fast lens, which means more light can reach the sensor on the camera, increasing signal in the images. In common aqueous PLIF scenarios that are not signal limited, a typical lens with an f-stop of f/2.8, lets in approximately 3 times less light than a f/0.95 (Appendix E.3). The high quality manufacturing ensures maximum light reaching the camera sensor, with minimal distortion and a narrow depth of field. Due to the highly sensitive nature of the lens, all lights had to be turned off during data capturing such as small computer lights covered with black tape, and the computer screen dimmed to minimal lighting. These steps are extremely necessary to minimize light pollution and increase the SNR. Additionally, a 532nm notch filter from Edmund Optics (Appendix E.4) was used to block any residual 532nm light in the sheet from reaching the camera.

### 2.4.3 Binning Images

In the final step to increase SNR in each image, the Zyla 4.2+ can be binned on the sensor chip before capturing images. If images are binned  $n \times n$ , the pixels will increase in area by  $n^2$ . Binning directly on the camera chip results in an increase of SNR as  $n$ , with a lower noise level than if it were binned post processing on the computer. To explain this in detail, a chip is defined as 4 pixels with a readout noise of  $5e^-$ . In unbinned mode, each pixel row ( $2 \times 1$  pixels) is shifted down to the amplifier and the signal is read. To read each pixel there is an associated noise involved (readout noise) typically expressed as  $Ie^-$ , where  $I$  is a set integer, and in this example  $5e^-$ . In unbinned mode the noise associated with each pixel is  $5e^-$ , therefore if we were getting a signal of  $20e^-$  then the SNR would be 4:1. If the images were binned on the computer after the fact, the SNR would increase to 8:1 following the quadrature rule. The quadrature rule states that the noise is added in quadratures, or square root of the sum of the noises squared, which for a noise of  $5e^-$  is equal to  $10e^-$ , and the signal accumulates linearly as 4, therefore  $80e^-/10e^-$  is equal to 8:1 SNR. However, if the chip were binned  $2 \times 2$ , resulting into one larger pixel with an increase in area of 4, the readout operation works differently. In the  $2 \times 2$  binned mode, the first row of pixels is shifted down to the amplifier, then the second row is also shifted and added to the first row. After this

addition, the two remaining pixels are summed, and readout on the amplifier. This results in an increase of signal by 4, while noise remains that for one pixel,  $5e^-$ , which is a SNR increase of  $80e^-/5e^-$ , 16:1 SNR. Thus, it is more efficient to increase the SNR by binning on the chip rather than binning after the image is captured. In this data, images were pre-binned 2x2, and further binned 4x4 in post-processing. This was done to increase SNR, while also checking that no structure was lost in capturing the images (discussed more in Appendix D).

#### 2.4.4 Camera Set Up

The camera is oriented perpendicular to the test section, such that images are collected in a 'x-y plane' slice from above (Fig. 2.10). The height of the camera, which is chosen to have proper depth of field is set by sliding aluminum tracks to the desired location on the vertical 80/20 piece, which can be locked in place by compatible bolts. The downstream location of the camera can be moved by sliding the vertical aluminum bars on their tracks, locking in place with bolts. The camera has three main cords to ensure proper operation: 1. Power Cord, 2. BNC trigger cable, and 3. USB 3.0. The BNC trigger cable was used to trigger the camera from the laser to ensure proper synchronized timing and framing rate of the captured images. The USB 3.0 is a state of the art technology that transfers data over to the computer via one simple USB 3.0 cord. The settings used in the software used to capture images, Insight 4G, are described in detail in Appendix F.

#### 2.4.5 Spectral Considerations

Using these PLIF system components and flow facility to take meaningful data sets requires consideration of spectral response of the acetone excitation, and emission, laser wavelength, camera spectral response, and filter spectral response. The spectral acetone excitation, laser wavelength must overlap to maximize fluorescence in the system, while the acetone emission and camera and filter spectral responses must overlap to maximize signal detected and collected. Acetone is excited over a range of low ultra-violet (UV) wavelengths (Fig 2.10) with maximum excitation at 275 nm and the laser used in these experiments falls close to the maximum at 266 nm, indicated on the



figure with a red line. Acetone vapor emits at 450 nm in a visible deep violet color (Fig. 2.11)

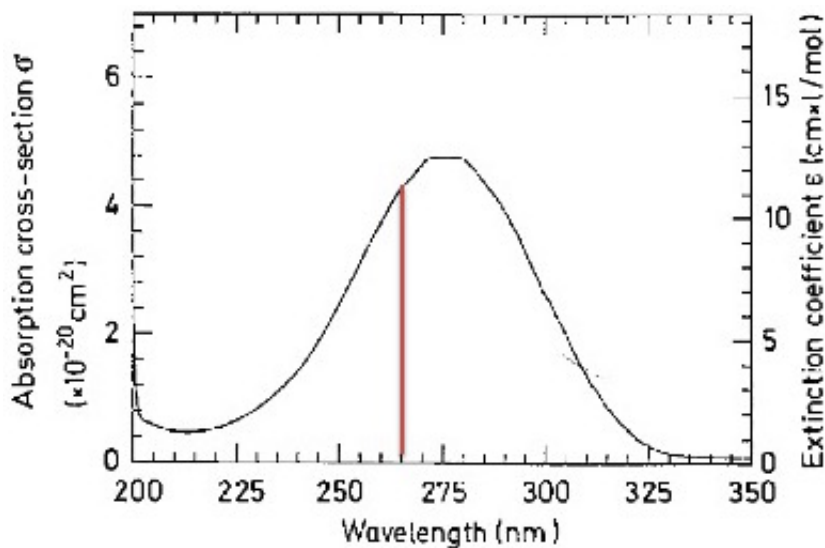


Figure 2.9: Absorption spectra of acetone vapor from [32]

which overlaps with the spectral response of the Zyla 4.2+ camera, indicated in Fig. 2.11 as a red line. Concurrently, the spectral response of the filter used to block residual 532 nm, allows 450nm to pass through at high transmittance percentages (Fig. 2.12).

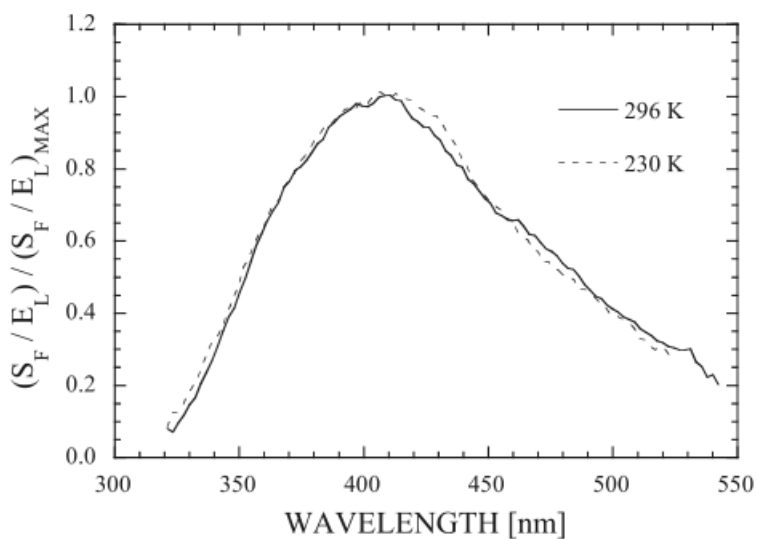


Figure 2.10: Emission spectra of acetone vapor from [8]

The purposeful alignment of these responses is how each piece of the system works together to

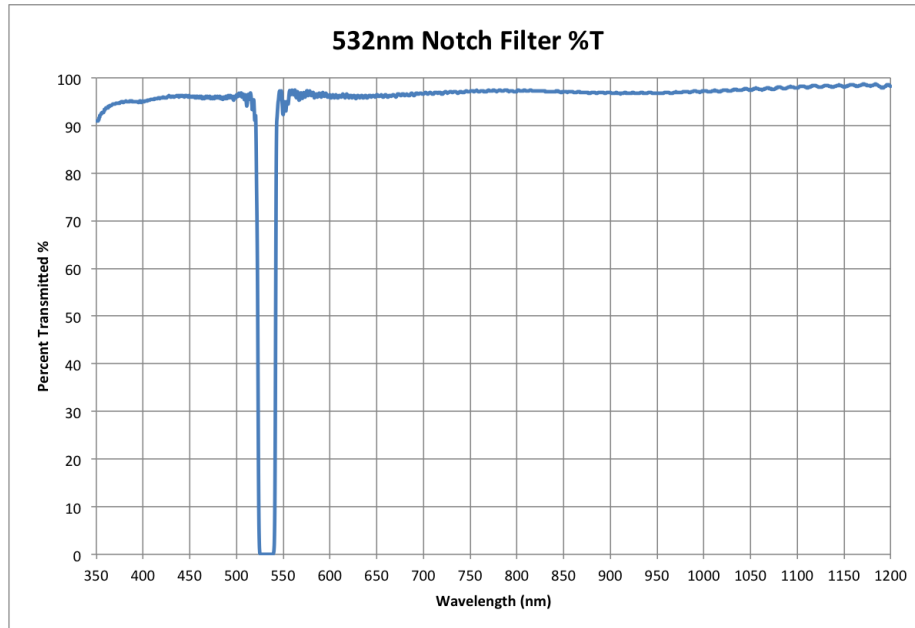


Figure 2.11: Transmission spectra of filter from Edmund Optics.

capture fluorescent flow data in a controlled environment. After that data is captured, the images are processed to return calibrated concentration fields.

## 2.4.6 Data Processing

The data collected on the camera is stored on a high-powered PC Machine, and processed to become meaningful concentration data. There are several processing equations used to reach the final calibrated concentration data, such as Beer-Lambert Law, background subtraction, and flatfielding.

### 2.4.6.1 Beer-Lambert Law

According to Beer-Lambert law the absorption along a path can cause changes in intensity of the ray of light, or laser beam. This is described mathematically as:

$$\frac{dI}{I} = -\epsilon C dr \quad (2.4)$$

Integrating both sides:

$$\frac{I}{I_0} = \exp(-\epsilon C(r_1 - r_2)) \quad (2.5)$$

where  $I$  is the intensity at location  $r_2$ , and  $I_0$  is the intensity at location  $r_1$ ,  $\epsilon$  is the absorption coefficient, and  $C$  is the concentration.  $I/I_0$  is the ratio of intensity lost due to absorption in the path length. In a uniform concentration field the attenuation along a path is negligible if  $\epsilon C (r_1 - r_2) \gg 1$ , making the system “optically thin”. This parameter of optical thinness is desirable for PLIF applications, and is assumed in these experiments. Experiments were done to test this assumption by filling the wind tunnel with low levels of acetone, and fitting the concentration values from a beam through the tunnel (Appendix G). In summary, it was found that a small loss due to Beer’s Law does occur, but over the path length of typical data set and full strength source concentration, these losses were insignificant ( $\leq 5\%$  attenuation). An attempt was made to estimate the absorption coefficient of acetone which is detailed more in Appendix G.

#### 2.4.6.2 Processing Equations

The data collected were processed similarly to that described in Crimaldi’s aqueous PLIF Review [14], which uses the following equation:

$$c_n(i, j) \approx \frac{b_n}{a_c(r, \theta)} \frac{I_n(i, j) - B_n(i, j)}{B_n(i, j) - D(i, j)} \quad (2.6)$$

where  $c_n$  is the concentration,  $B_n$  is the uniform background dye concentration in the recirculating flume,  $a_c$  is the attenuation coefficient,  $I_n$  is the recorded fluorescence intensity,  $B_n$  is spatial fluorescence intensity in a uniform background concentration field, and  $D$  is the dark response. There are several notable differences in the processing of gaseous data from a wind tunnel versus a recirculating aqueous flume as described in Crimaldi [14]. First,  $b_n$  is not relevant in a single pass wind tunnel since no background dye accumulates over time in the tunnel.  $a_c$  accounts for attenuation of the laser sheet in the dye, which if severe, degrades signal beyond a certain path length, but was found to be negligible for the purposes of this thesis (Appendix D).  $B_n$  captures the power variations in a laser sheet, and normalizes each pixel accordingly. To capture  $B_n$  in a

single pass wind tunnel, the tunnel was sealed on both ends, and allowed to come to a steady state in which low acetone concentrations were well mixed in the tunnel, and several hundred images were captured. Lastly, a new term,  $B_a$  was used, which captures the ambient background of the wind tunnel without acetone, and includes the dark response,  $D$ . Using these variables, a modified version of equation 2.3 can be written for the wind tunnel as:

$$c_n(i, j) \approx \frac{I_n(i, j) - B_a(i, j)}{B_n(i, j) - B_a(i, j)}. \quad (2.7)$$

This equation was used to process all images collected in the wind tunnel (codes for processing in Appendix F). Most concentration fields were normalized by maximum concentrations and cropped to include only relevant areas of the image (e.g. cut out visible ends of the wind tunnel and laser slits). All processing was completed in MATLAB as it is equipped to handle large 3D matrix math in an efficient manner.

#### 2.4.6.3 Noise Characterization

The noise for the system was characterized in each data set. The noise for the camera is reported as 0.9 e-, and was found to vary 1 count in unbinned images. Therefore, it was presumed that the shot-to-shot noise of the laser dominates the noise of the system. A known specification of noise for our own laser was tested at the factory and found to be about 1% in the laser head. We also looked to characterize this noise, and the RMS of the flatfield images were calculated in the following manner:

$$RMS_{noise} = \frac{\sum(\text{InstantaneousFlatfield} - \text{AverageFlatfield})^2}{\text{Totalimages}}. \quad (2.8)$$

After this calculation, the RMS of the noise was also flatfielded. This was to ensure spatial consistency within the RMS field, since areas with higher signal would have higher RMS otherwise. An image of before and after the RMS was flatfielded are shown below in Figures 2.12a and 2.12b.

From these images, a histogram of RMS values of the noise is shown in Figure 2.13. This

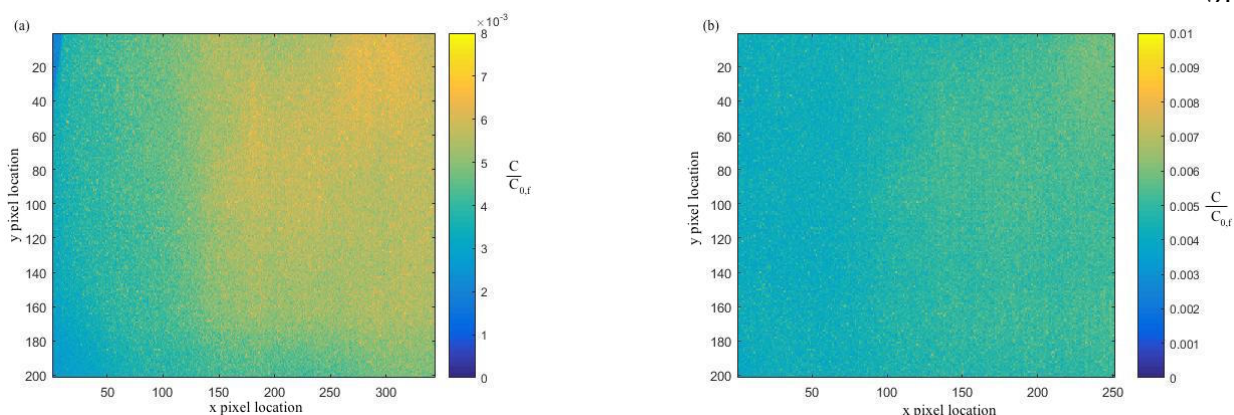


Figure 2.12: RMS spatial images (a) not flatfielded and (b) flatfielded.

indicates a median value of noise of  $0.00483C_F$ , where  $C_F$  is the maximum concentration in the flatfield images. This estimate is a factor of 2 below the factory spec of laser noise. This difference in values may be due to the way we computed the noise, which was from very low concentration flatfield images. The concentration in those images was around 70 counts, while the source concentration in the data had counts close to 7000 counts. In the lower concentration images we would not expect to capture the specified shot-to-shot noise from the laser, as the signal is not strong enough. Therefore, we would expect the noise to increase to closer to 1% of the source, if using a moderately higher flatfield image. Additionally, a better way to measure shot-to-shot noise would be to have a fixed object in the image, which consistently fluoresced i.e a piece of white paper, so no concentration dependence is needed.

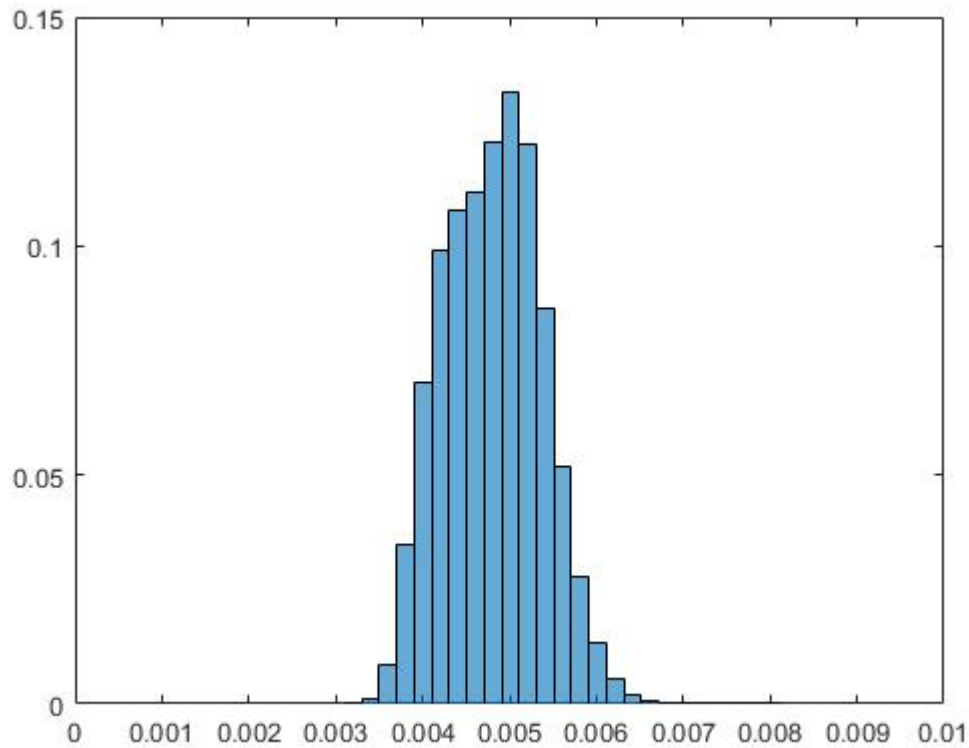


Figure 2.13: Histogram of RMS values from Figure 2.12.

## 2.5 Collected Data Configurations

The following Table 2.1 describes the two data collection configurations using all components. The important factors included are field of view, binning, flow rate, framing rates, pulsed laser rate, length of data, and flow configuration. In the results all data used are 30Hz data.

Table 2.1: Data Configurations

Flow Condition	Velocity	Field of View	Binning	Framing Rate	Length of Data
Unbounded	5 cm/s	10 cm x 17.5 cm	4x4	5 Hz	20 minutes
				15 Hz	5 minutes
				30 Hz	5 minutes
Near bed	5 cm/s	20 cm x 35 cm	4x4	5 Hz	20 minutes
				15 Hz	5 minutes
				30 Hz	5 minutes

## Chapter 3

### Results

#### 3.1 Unbounded Data Results

##### 3.1.1 Instantaneous Plume Structure

The instantaneous structure of a plume is highly intermittent, with areas of high concentration next to areas of no concentration. Two images were chosen randomly from the dataset to illustrate the intermittent and complex nature of the plume structure, and it is expected that the plume structure and corresponding profiles will vary significantly image to image. Figure 3.1a-b. shows two different instantaneous plumes at  $z=0$  mm, in an x-y plane area of  $120 \times 100$  mm<sup>2</sup>, normalized by the source concentration,  $C_0$ . Streamwise profiles at  $y=0$  of each plume (Fig. 3.2a. and Fig. 3.3a.) have fluctuating concentration values, with significant peaks and valleys along the centerline, and a general concentration magnitude decrease as distance from the source increases. In Figures 3.2b. and 3.3b. the lateral profiles of each plume at  $x=10$  mm and 60 mm similarly reveal concentration fluctuations with biases to different sides of the plume source due to cross-wind flapping in the flow facility.

The comparison of a long time-record (5 minutes) at a single point, to a short time record (30 seconds) at the same point reveals differences in available concentration information over the two time scales. Time series of three different locations downstream of the source are shown in Figs. 3.4-3.6. At the first location,  $z=0$  mm,  $y=0$  mm, and  $x=10$  mm, there is a consistent nonzero concentration observed in both long and short time series. The signal alternates about the mean

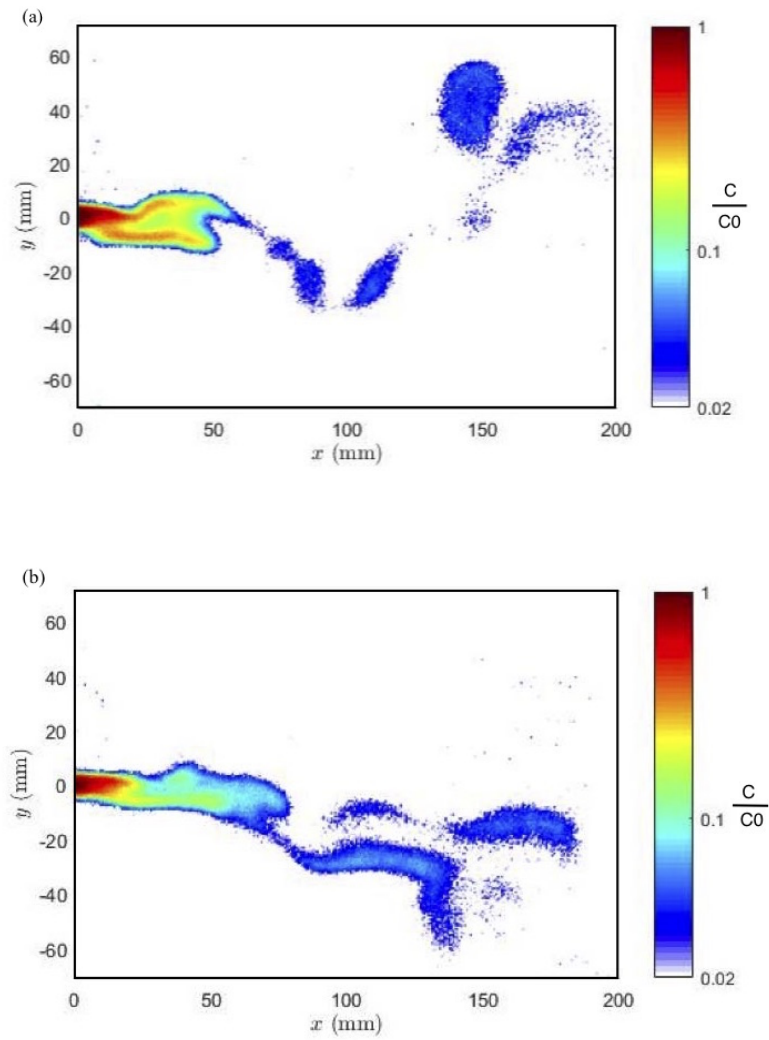


Figure 3.1: (a-b). Two representative false-color instantaneous plume structures for unbounded case.



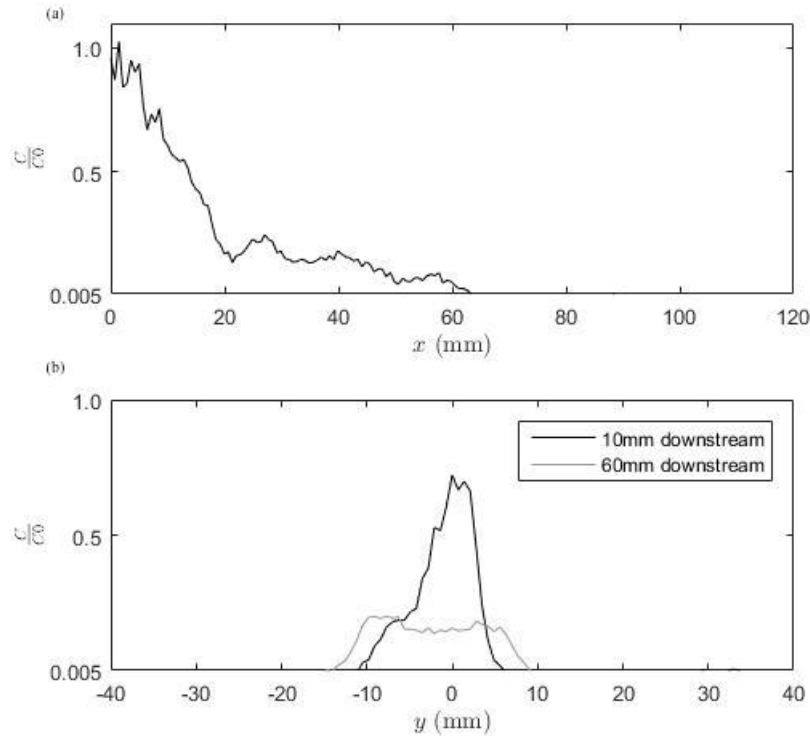


Figure 3.2: Profiles of (a) streamwise at  $y=0$  and (b) lateral locations at  $x=10$  mm, and  $x=60$  mm for the instantaneous plume shown in Figure 3.1a.

concentration at the point, which is 63% of the source concentration and denoted by the dashed gray line.

At the second location,  $z=0$  mm,  $y=-8$  mm,  $x=40$  mm, intermittent nonzero values exist in both the long and short time series. In the long time-series concentration reaches peak values above 50% of the source, while in the short time series values only reach 40% of source concentration. In both, there are sustained periods of signal, followed by short durations of zero concentration. This trend is most visible in Fig.3.6b, where the shorter time scale reveals the discrete odorant signal which persists above zero for several seconds. At this location concentrations peaks range from 40-60% of the source concentration, which is well above the mean concentration at that location, 15% of source concentration.

At the third location,  $z=0$  mm,  $y=-16$  mm, and  $x=70$  mm, the signal has intermittent

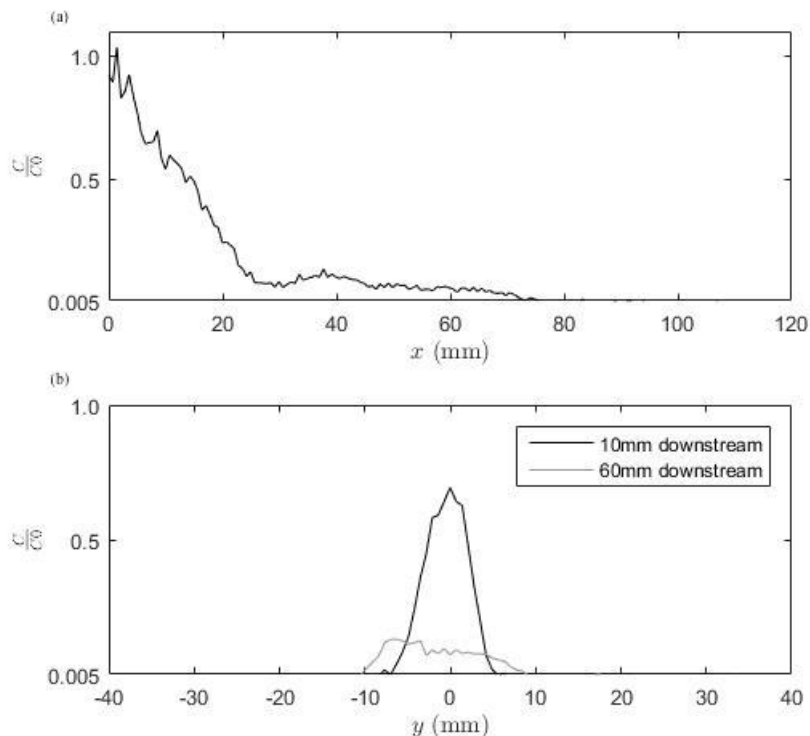


Figure 3.3: Profiles of (a) streamwise at  $y=0$  and (b) lateral locations at  $x=10$  mm, and  $x=60$  mm for the instantaneous plume shown in Figure 3.1b.

nonzero spikes followed by longer periods of zero concentration than observed in both Figs 3.4 and 3.5. In the short time series, small clusters of odorant signal are followed by several seconds of zero concentration. The longer duration of zero concentration indicates that intermittency is decreasing from the source, and the probability of encountering a detectable odorant signal above a threshold is decreasing with increasing distance from the source. Concentration peaks range from 10-20% of the source concentration, which is significantly above the mean concentration at the location, 5% of the source concentration.

The instantaneous data is the most native form of the data, and in the context of animal olfaction is the signal the organism will encounter while tracking an odorant. In addition to this understanding of the instantaneous signal it is also useful to analyze the data using several statistical measures, which help to describe the behavior of a plume by characterizing statistical trends and behaviors.

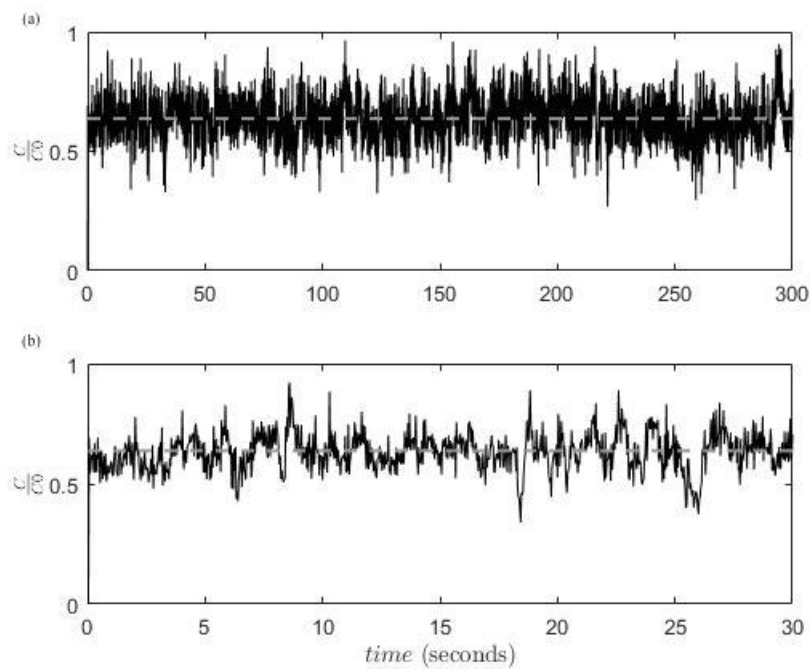


Figure 3.4: Time series over periods of (a) 5 minutes and (b) 30 seconds at  $z=0$  mm,  $y=0$  mm,  $x=10$  mm. Mean concentration is shown with dashed lines.

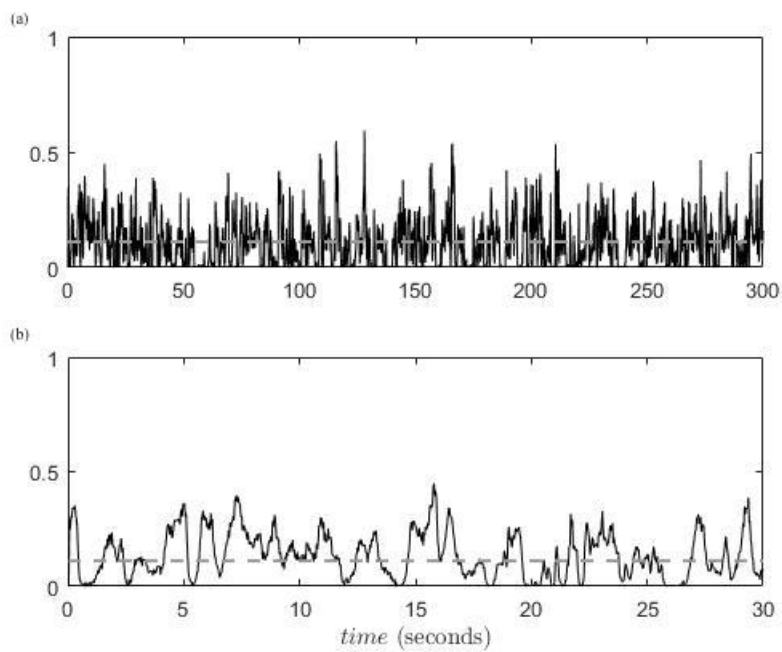


Figure 3.5: Time series over periods of (a) 5 minutes and (b) 30 seconds at  $z=0$  mm,  $y=-8$  mm,  $x=40$  mm. Mean concentration is shown with a dashed line.

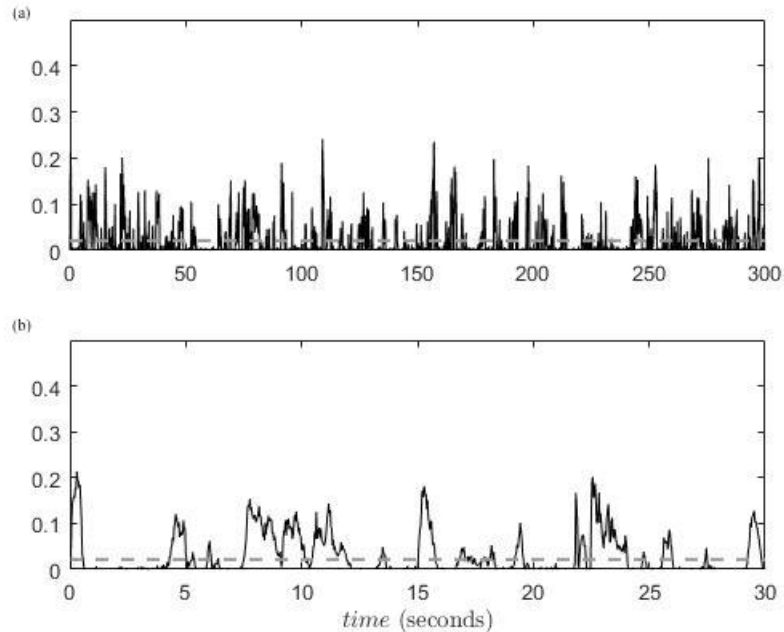


Figure 3.6: Time series over periods of (a) 5 minutes and (b) 30 seconds at  $z=0$  mm,  $y=-16$  mm,  $x=70$  mm. Mean concentration is shown with a dashed line.

### 3.1.2 Statistical Measures of Plume Structure

There are many different statistical measures that can be used to analyze plume structure. In order to best analyze the plume behavior in relation to olfaction three statistical measures were chosen for analysis: time-averaged concentration, root-mean-square (RMS) of concentration fluctuations (intensity), and the intermittency ( $\text{Pr}: C \geq C_t$ ). In all presented images the calculated RMS of the noise floor,  $0.0048C_0$ , is used as the lower limit of meaningful data. It is at this concentration value that the signal-to-noise ratio reaches 1, and below the floor SNR continues to decrease below 1 making all reported values below this level no longer meaningful.

The normalized time-averaged concentration plume shown in Fig. 3.7, shows the time-averaged spread of the plume in both streamwise and lateral directions. The streamwise profile is averaged over 3 pixels in the lateral direction, and 6 pixels in the streamwise direction to produce a smooth curve. A comparison of different smoothing techniques is shown in Fig. 3.8, which indicates that the 3x6 smoothing exhibited the most smoothing with no loss of information.

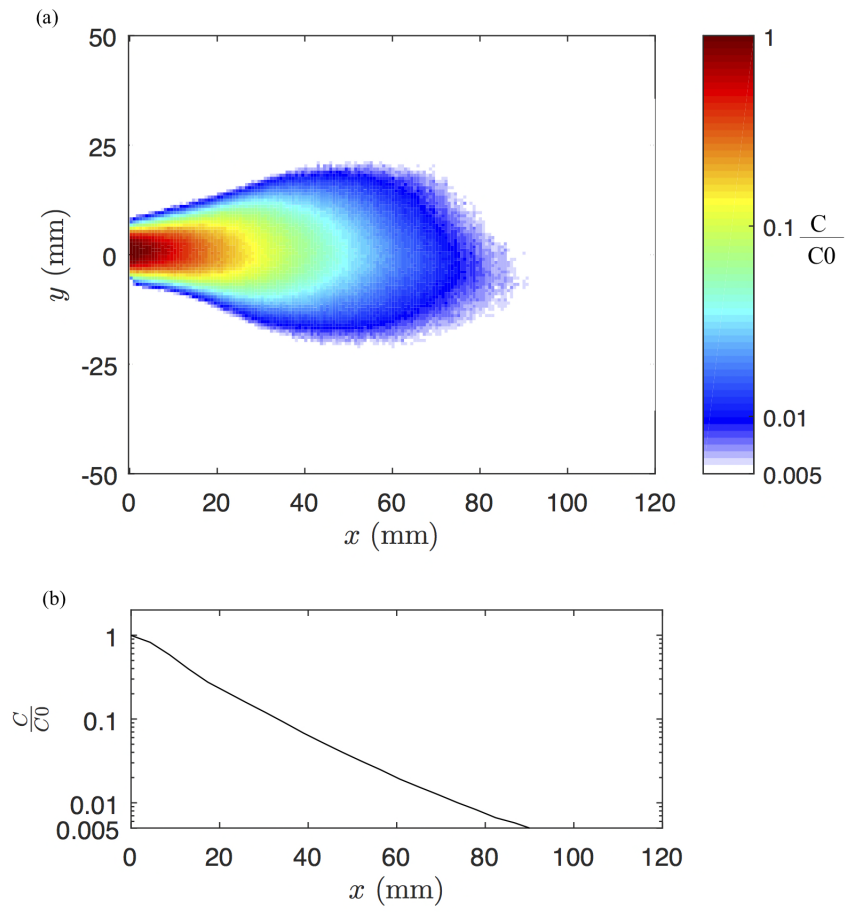


Figure 3.7: (a) Normalized mean concentration of the unbounded plume, with (b) corresponding streamwise profile at  $y=0$  mm.

The false color image of the mean concentration structure shows the extent of the average

plume spread in both the lateral and streamwise directions. The streamwise profile of the mean plume has a monotonic decrease, reaching the noise floor at 85 mm downstream, consistent with the spread of the false-color image of the plume. The mean concentration plume differs greatly from instantaneous time series discussed in Figs. 3.5 and 3.6, which showed that instantaneous concentrations at downstream locations are not well represented by the time-averaged values. This suggests that the mean concentration plume is a product of the large nonzero concentration spikes and zero concentration values as observed in Figs. 3.5 and 3.6, resulting in lower average values than are actually occurring at those downstream locations.

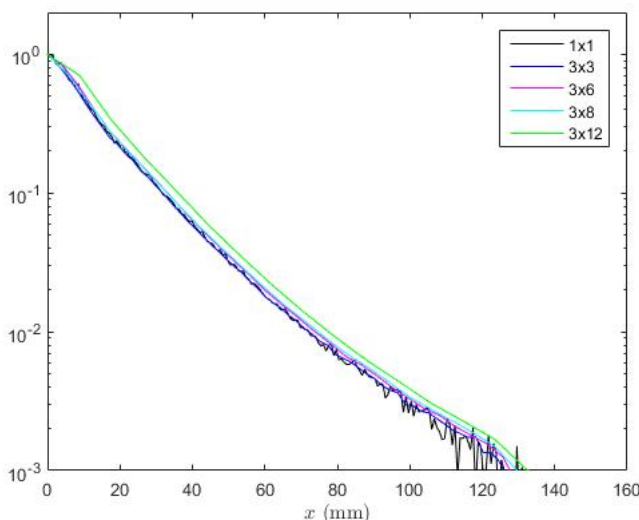


Figure 3.8: Smoothing comparisons for mean streamwise profile curve.

Lateral profiles of the mean concentration plume show a larger spread downstream of the source (Fig. 3.9). The lateral spreads fit expected Gaussian behavior, which is fitted to curves in Fig. 3.9. Moving downstream from 10 mm to 60 mm, the plume spreads by more than a factor of 2, with  $\sigma_y = 10$  mm increasing to over 20 mm. The spreading behavior is consistent with Fig. 3.7, and is expected due to diffusion and advection of the plume, which mixes and spreads the plume across longer distances as downstream distance of the source increases.

The second statistical metric of plume structure is the RMS of concentrations fluctuations, or intensity. The normalized RMS is calculated as follows:

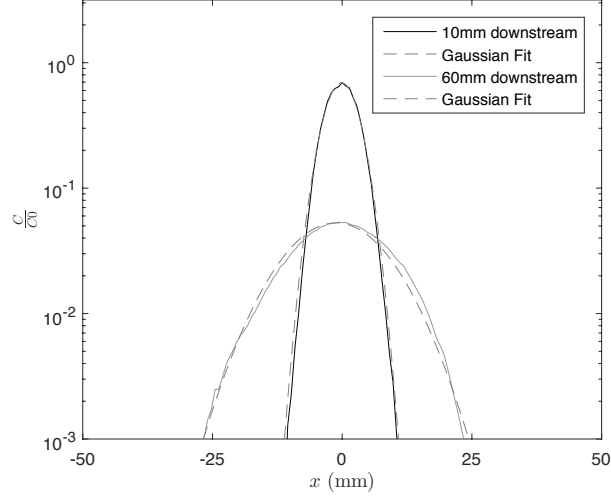


Figure 3.9: Lateral profiles of mean concentration at  $x=10$  mm and  $x=60$  mm. Gaussian fits are shown as dotted lines.

$$\text{RMS} = \sqrt{\frac{\sum (C_{\text{instant}}/C_0 - C_{\text{avg}}/C_0)^2}{n}} \quad (3.1)$$

where  $C_0$  is the source concentration,  $C_{\text{instant}}$  is the instantaneous concentration,  $C_{\text{avg}}$  is the average concentration at that location, and  $n$  is the number of images. The normalized RMS of the plume is shown in Fig. 3.10 at  $z=0$  mm, over the same  $120 \times 100$  mm<sup>2</sup> area as shown in Fig. 3.7. The RMS centerline is averaged using the same  $3 \times 6$  technique as the time-averaged centerline, over 3 pixels laterally and 6 pixels downstream.

In Figure 3.10a and b the maximum RMS occurs slightly downstream of the source. The immediate plume exiting the nozzle will have a consistent strong concentration core with little to no fluctuations, resulting in a low RMS value. Slightly downstream of the core, strong, but

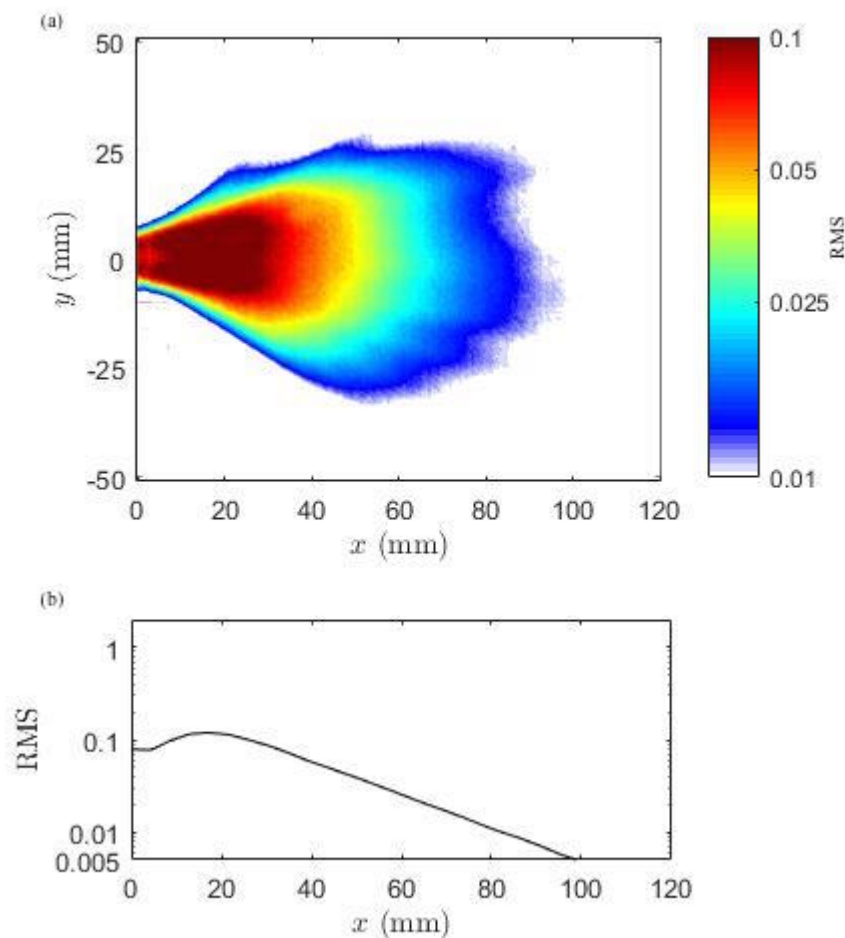


Figure 3.10: (a) Normalized RMS fluctuations of the unbounded plume with (b) corresponding streamwise profile at  $y=0$  mm.

more infrequent concentrations will occur due to the cross-wind in the tunnel. These contribute more to the RMS calculation than the time-averaged concentration, therefore the maximum RMS occurs slightly downstream from the source. The centerline structure of the RMS also shows the maximum slightly downstream of the exit of the tube. The RMS covers a larger spatial area than observed in the time-average plume. This is due to infrequent but strong concentration filaments occurring downstream of the source. The RMS extends farther in space because if a filament persists downstream in one single event, it will still contribute to the calculation of the RMS, whereas in the time-averaged plume it would be averaged out with zero values. In Fig. 3.11 the lateral spread



of the RMS at the same locations in the time-averaged plume,  $x=10$  mm, and  $x=60$  mm, show that the RMS spreads more at both downstream locations than observed in the time-averaged plume.

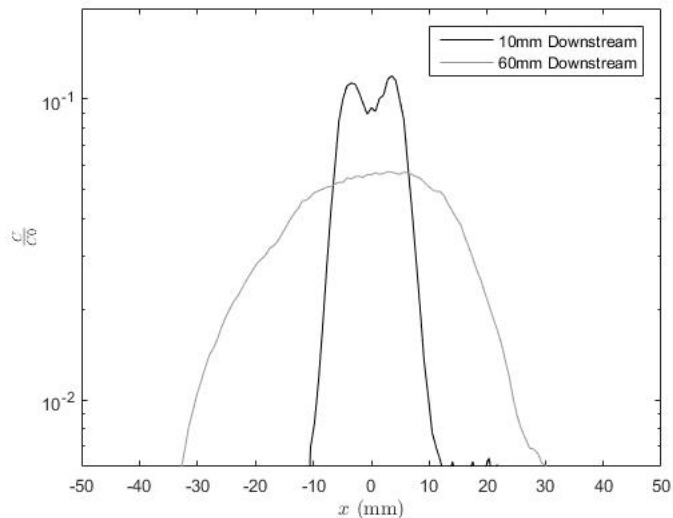


Figure 3.11: Lateral profiles of RMS at  $x=10$  mm and  $x=60$  mm.

In Fig. 3.12 a comparison of the time-average and RMS centerline structures show the time-averaged plume centerline magnitude dominates near the source, and after 40 mm downstream the RMS becomes the dominate signal. This suggests that near the source the time-average plume is a better metric to understanding the plume behavior, while farther downstream the RMS becomes a more robust metric. Furthermore, the slope of the RMS line decreases at a slower rate than the slope of the time-averaged line, suggesting that the time-averaged behavior more quickly falls below the noise floor than the RMS downstream of the source. Again this suggests that the RMS is a better metric of plume behavior at farther locations downstream from the source.

The last statistical measure used to describe plume behavior, and perhaps the most important for olfactory navigation, is intermittency. As previously defined, intermittency is the probability that the concentration will exceed some defined threshold,  $\text{Pr}: C \geq C_T$ . Any real olfactory sensor has a finite detectability, and the intermittency conveys important information if there is signal above that detectability, and if so what is the probability it will be encountered. In Fig. 3.13, a defined threshold of  $C_T = 0.03C_0$  is used to compute the probabilities. The intermittency behaves

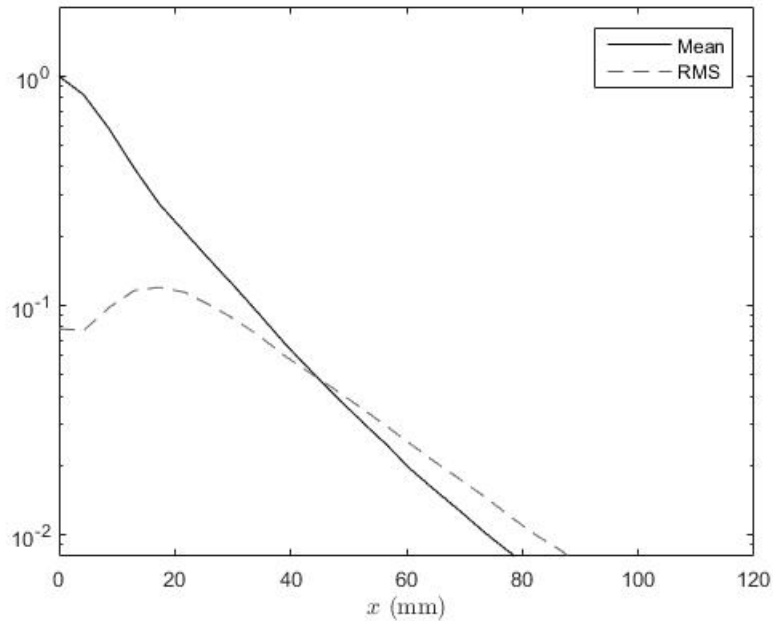


Figure 3.12: Comparison of the mean and RMS streamwise profiles at  $y=0$  mm.

much differently than the time-averaged and RMS plume, persisting at a value of 1 for approximately 20 mm downstream of the source on the centerline. This means that for 20 mm downstream of the source release there is a 100% chance that an organism will detect that signal. Additionally, the intermittency persists farther downstream than the mean and RMS plumes, observed in both the false color and centerline structure. Along the centerline small probabilities of encountering  $C_T$  exist past 100 mm downstream of the source, while in the time-average and RMS plumes no detectable values remained past 80 or 95 mm respectively. The lateral spread of the intermittency near the source exhibits a “top-hat” behavior, with almost 100% certainty of detecting the plume over a 20 mm width, dropping off drastically to zero within less than a 1 mm (Fig. 3.14). Downstream at 60 mm the lateral spread shows a smoother decrease, with a 50% probability of detecting  $C_T$  at the centerline, decreasing to 0% by 30 mm off the centerline.

A second perspective on intermittency is also examined to help convey the importance of intermittency in relation to olfaction. Instead of setting a threshold  $C_T$  and creating a map of spatial probabilities, a probability is chosen and a map of concentration thresholds are plotted in Figs. 3.15

and 3.16. In Figs. 3.15 and 3.16, 50% probability and 10% probability are plotted for 5 varying concentration thresholds. In Fig 3.15 a small spatial area exists for detecting concentrations with a intermittency of 50%, and this area extends both laterally and downstream when the intermittency decreases to 10% in Fig 3.17. This has important implications for olfactory navigation, and provides

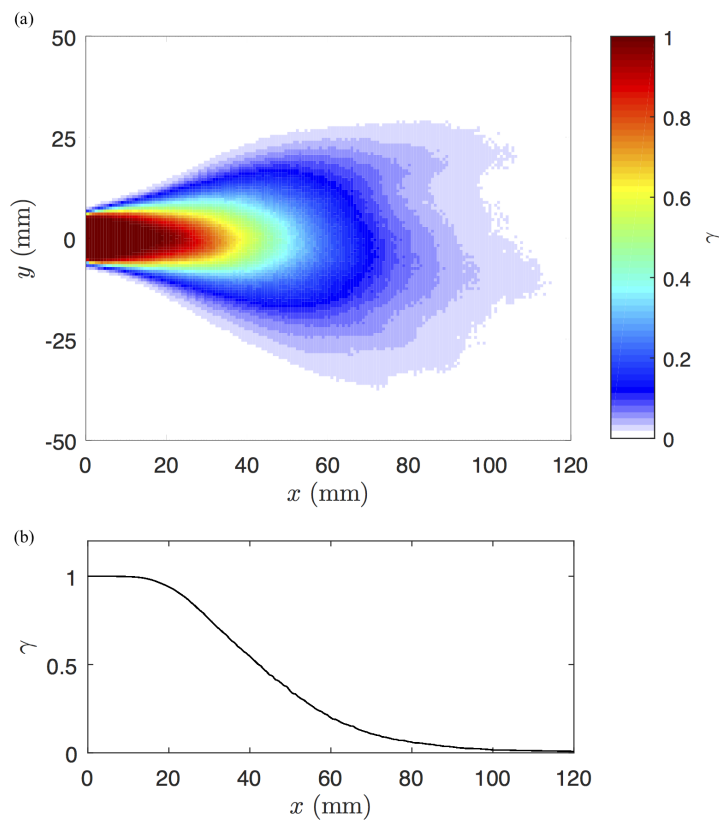


Figure 3.13: (a) Intermittency for  $C_T = 0.03C_0$  with (b) corresponding centerline profile at  $y=0$  mm.

a spatial understanding of the different concentration thresholds organisms may need to first detect an odorant signal.

To understand how the concentration evolves spatially and temporally in an unbounded flow, series of 30 second time histories and the corresponding pdfs are plotted in Figs. 3.18 and 3.19, respectively. A map of these locations is shown in Fig. 3.17, with each location denoted by an  $x$ , corresponding to each panel. The locations are shown over all three statistical metrics so an understanding of how each metric may be influencing the behavior is clear. The locations chosen in Fig. 3.17 cover the symmetrical plume at varying centerline and lateral downstream locations.

In Fig. 3.18 locations closer to source have more consistent non-zero concentrations occurring, with no zero values present at the two closest locations,  $x=10$  mm and  $y=0$  mm, and  $x=10$  mm and  $y=-8$  mm. Farther downstream and off the centerline, all locations have zero concentration detected over the 30 seconds. The frequency of zero concentrations increases while moving farther downstream and farther laterally off the centerline. This is consistent with both the RMS persisting farther downstream than the time-average plume, and the intermittency decreasing downstream from the source. The intermittent signal causes the RMS to persist farther downstream than the time-average, because single concentration peaks contribute to the RMS calculation, while the

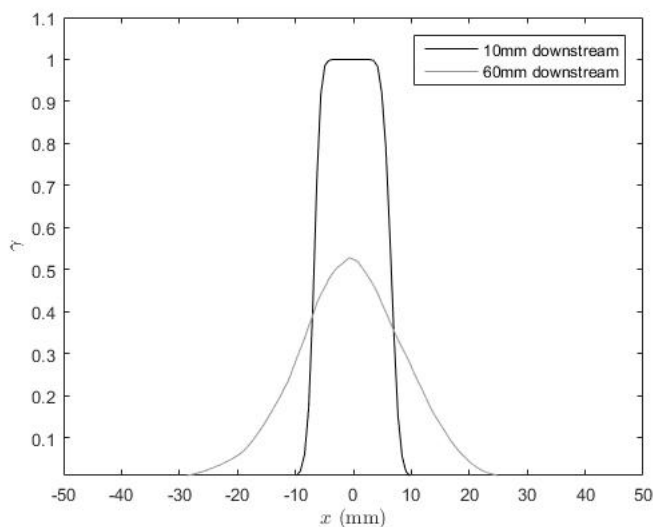
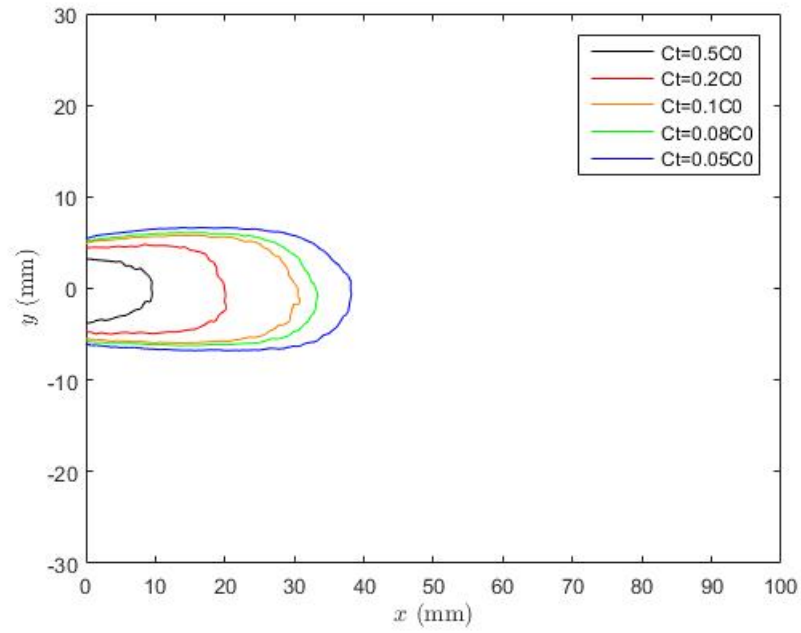
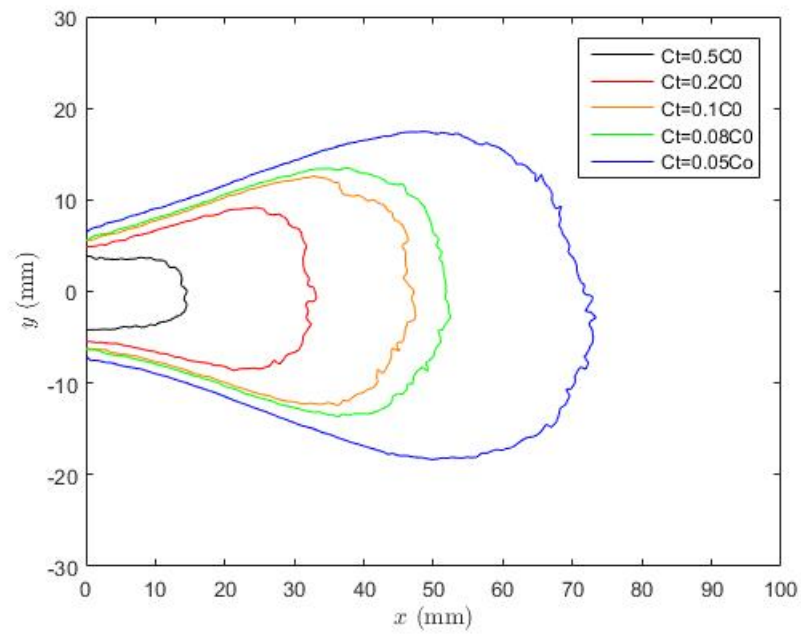


Figure 3.14: Lateral profiles of intermittency at  $x=10$  mm and  $x=60$  mm.

Figure 3.15: Contours of  $C_T$  for  $\gamma = 0.5$ .Figure 3.16: Contours of  $C_T$  for  $\gamma = 0.1$ .

time-averaged calculation smears out these peaks by averaging with the zero concentration values. Again, the time-average at each location in Fig. 3.18 becomes a worse metric of behavior the farther downstream and off centerline the location is.

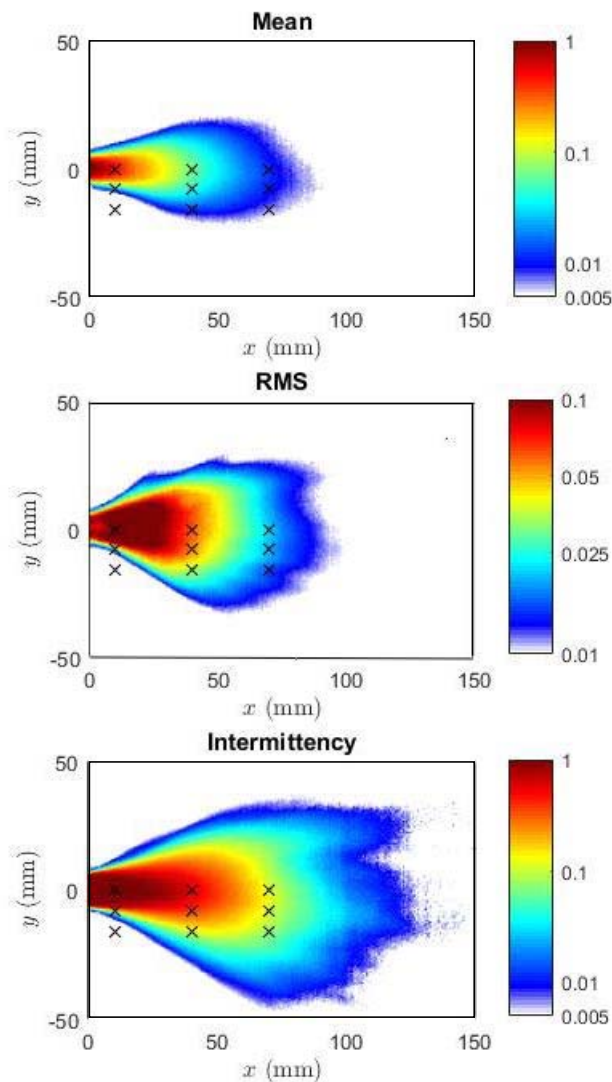


Figure 3.17: Map of the nine time series locations (denoted by x's) in relation to each statistical measure.

In Fig. 3.19 the pdfs of each location show a gradual change in the statistical distributions of

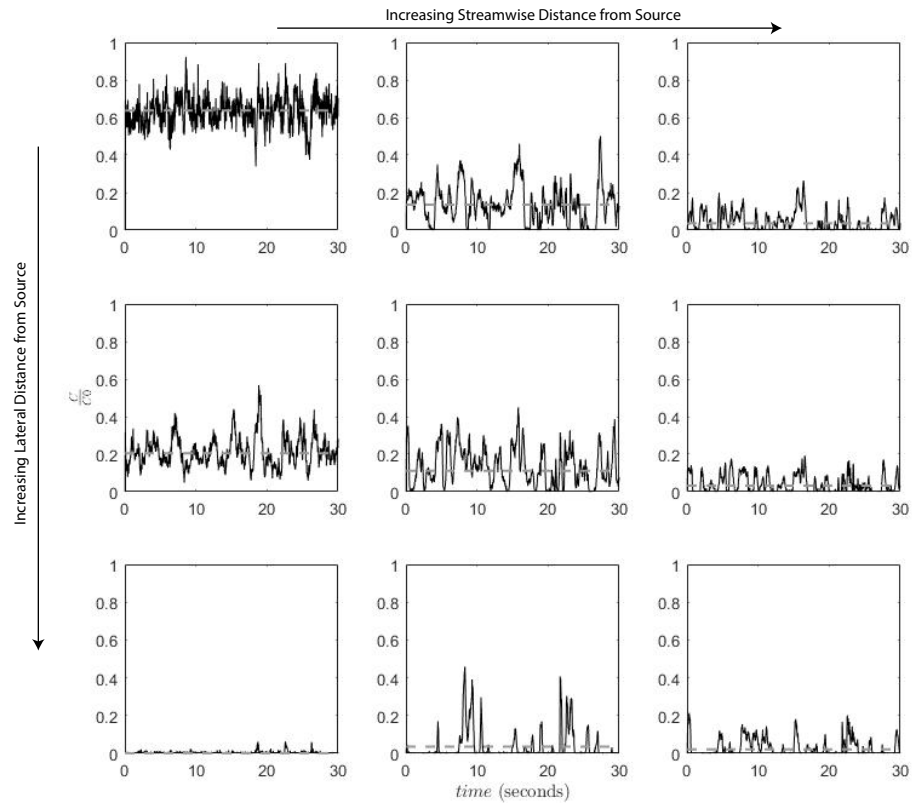


Figure 3.18: Representative time-series of instantaneous normalized concentration for each of the nine locations shown in Fig. 3.18.

the concentrations. Close to the source, a normal distribution about a non-zero concentration value occurs. Moving downstream along the centerline a semi-normal distribution is observed at  $x=40$  mm, which evolves to lognormal at 70 mm downstream. Moving off the centerline a similar trend occurs, where a normal distribution persists at 8 mm off the centerline, but quickly transforms to a log-normal distribution 16 mm off the centerline. This change from normal to a log-normal distribution occurs as the likelihood of encountering a zero value increases. In each lognormal distribution the highest probability exists for encountering a concentration of zero, which reaches a maximum the location farthest downstream and off the centerline of the plume.

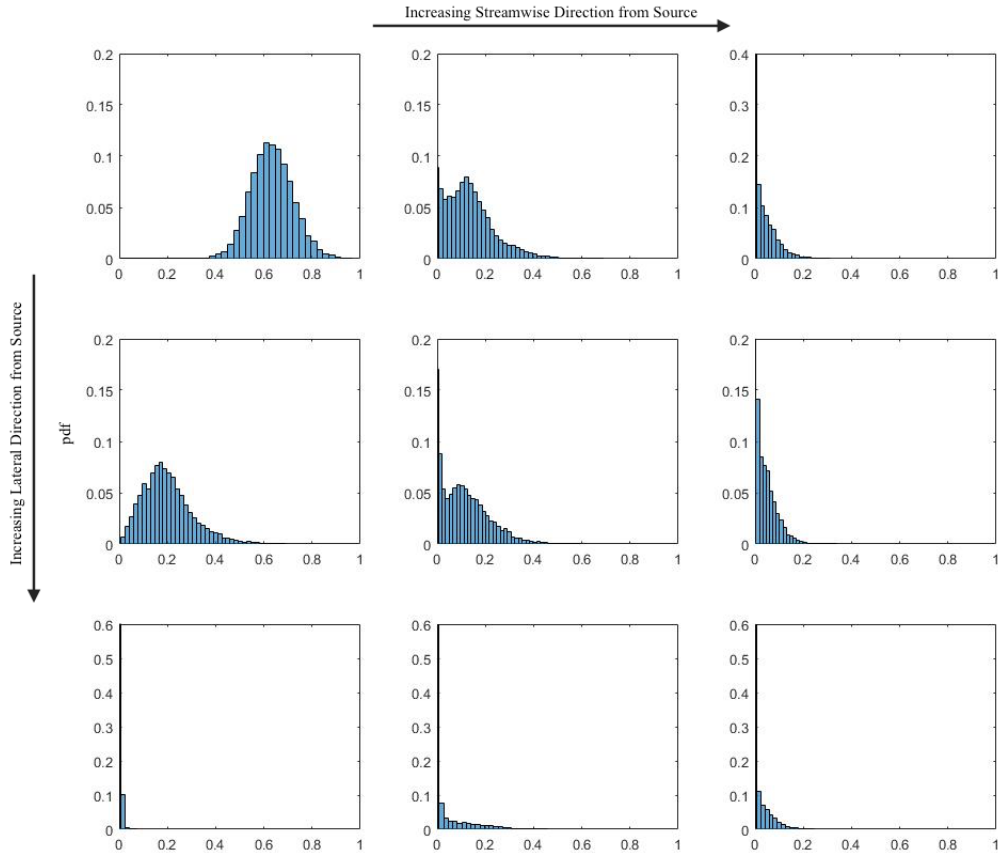


Figure 3.19: Representative pdfs of instantaneous normalized concentration for each of the nine locations shown in Fig. 3.18.

## 3.2 Bounded Data

### 3.2.1 Instantaneous Plume Structure

The introduction of a boundary close to the source release will alter the downstream structure by inhibiting 3D mixing that was observed in the unbounded case. In Fig. 3.20a-b the bounded plume covers a larger spatial area than observed in Fig 3.1a-b of the unbounded plume, and has a wider, more consistent plume width persisting farther downstream than observed in the unbounded data. In Figs. 3.21a and 3.22a the centerline profile exhibits similar fluctuating behavior seen in the unbounded plume, with peaks and valleys of concentration along the centerline. A notable



difference is the concentration remains above the noise floor for a farther distance downstream, 250 mm, than observed in the unbounded data, 80 mm. The instantaneous lateral profiles in Figs. 3.21b and 3.22b 10 mm downstream has a similar lateral spread to that in the unbounded data,  $\sigma_y = 10mm$ , but in the bounded data has a higher concentration magnitude close to 1, whereas the magnitude in the unbounded data is  $0.6C_0$  or 60% of the source concentration. Additionally, the bounded data does not fit Gaussian trends downstream, as the introduced boundary causes the plume to deviate from Gaussian behavior.

Three time series at the same locations described in the unbounded data are shown in Figs. 3.23-3.25. At the first location (Fig. 3.23), the concentration never reaches values of zero, remaining consistently at  $\frac{C}{C_0} = 1$ . Similarly in the unbounded data the concentration also does not reach any zero values at that location. However, the magnitudes differ between the two cases and the concentration is much lower in the unbounded case, 63% of the source concentration, whereas in the bounded it remains close to 100% of the source concentration.

At the second time point (Fig. 3.24) concentrations in the bounded data remain largely above zero, with only a few intermittent spikes of zero concentration observed over the entire 5 minutes. At this location in the unbounded data, the concentration consistently fluctuates between zero and non-zero values, reaching zero values much more frequently than observed in the bounded data. The concentration magnitude in the bounded data remains at a constant value of 30% of source concentration and close to the mean at that location, whereas in the unbounded data there are large fluctuations in concentration magnitude with extremes of 0 and 50% of source concentration occurring.

At the third time point in Fig. 3.25, concentrations remain similar in magnitude to those observed in Fig. 3.24. Concentration values rarely reach zero, with a few more instances than observed in Fig. 3.24. At this location in the unbounded data (Fig. 3.5), concentration values fluctuate between zero and 20% of the source concentration, with frequent occurrences of zero concentration, while in the bounded data infrequent occurrences of zero concentration occur and the concentration remains consistently close to 30% of the source concentration. One major difference

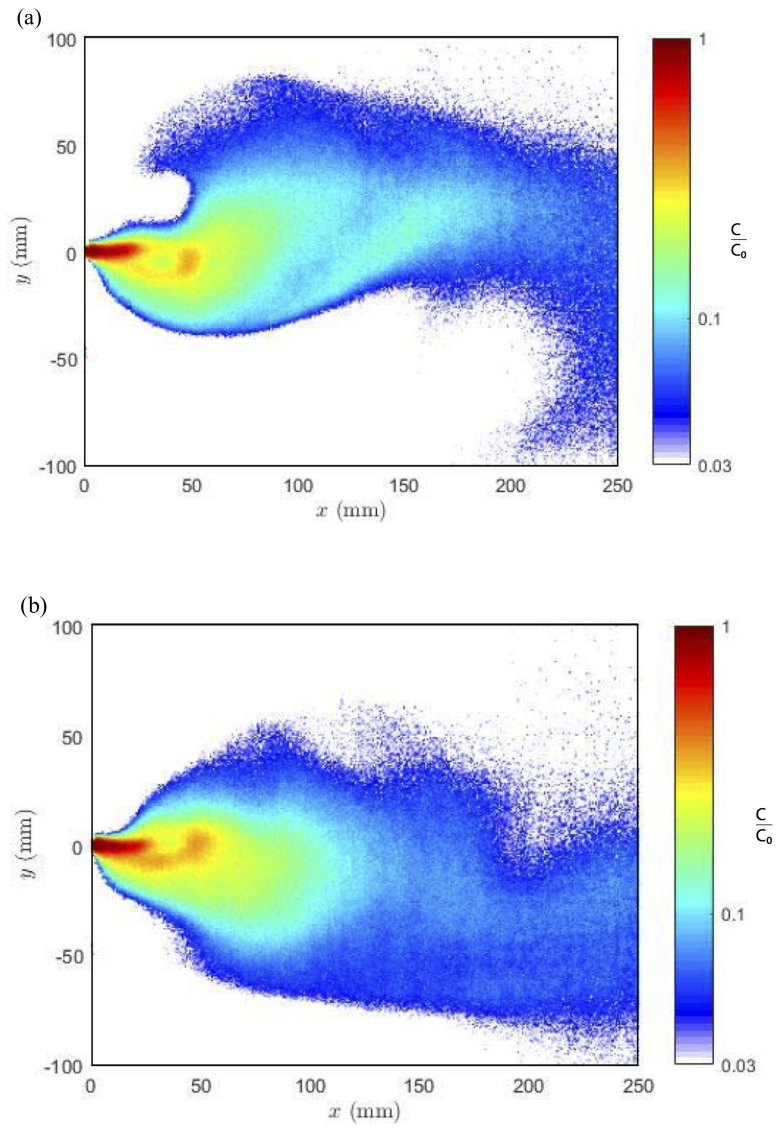


Figure 3.20: (a-b) Two representative false color instantaneous plume structures for bounded case.

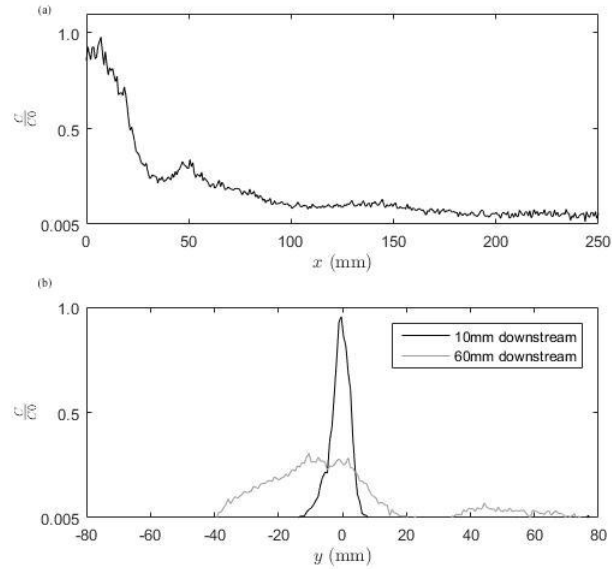


Figure 3.21: Profiles of (a) centerline and (b) lateral locations at  $x=10$  mm, and  $x=60$  mm for the instantaneous plume shown in Figure 3.21a.

observed in Figs. 3.23-3.25, is that the mean value is a much better estimate of the concentration at these locations than it is in the unbounded data. This is not true for the unbounded data, since the mean value is biased by the more frequent occurrences of zero concentration.

### 3.2.2 Statistical Measures of Plume Structure

The time-averaged mean concentration bounded plume (Fig. 3.26) has a more consistent spread over a larger area than observed in the unbounded data (Fig. 3.7). Detectable concentrations with less filamentous structure persist farther downstream in the bounded data than in the unbounded data. The centerline concentration structure also differs from the unbounded data, decreasing at a much slower rate, and remaining above the noise floor over a larger distance. One important note is that the non-monotonic decrease in the bounded centerline is believed to be a physical artifact in the data. In capturing data near a boundary, several complications arise such as increase in reflections, and a high sensitivity in flow to any disturbances in the bed. These factors, as well as other unknown experimental factors could have contributed to this deviation. Although

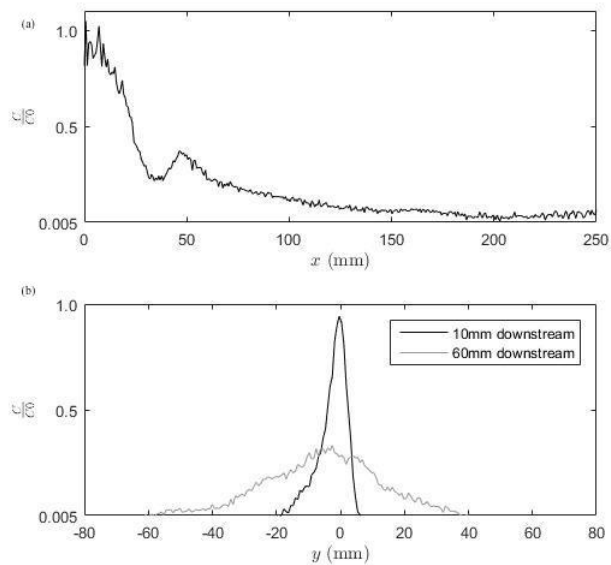


Figure 3.22: Profiles of (a) centerline and (b) lateral locations  $x=10$  mm, and  $x=60$  mm for the instantaneous plume shown in Figure 3.21b

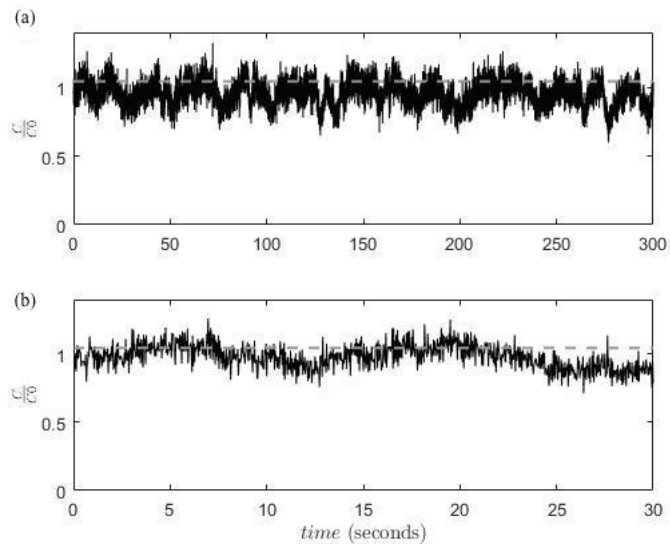


Figure 3.23: Time series over periods of (a) 5 minutes and (b) 30 seconds at  $z=0$  mm,  $y=0$  mm,  $x=10$  mm. Mean concentration shown with dashed line.

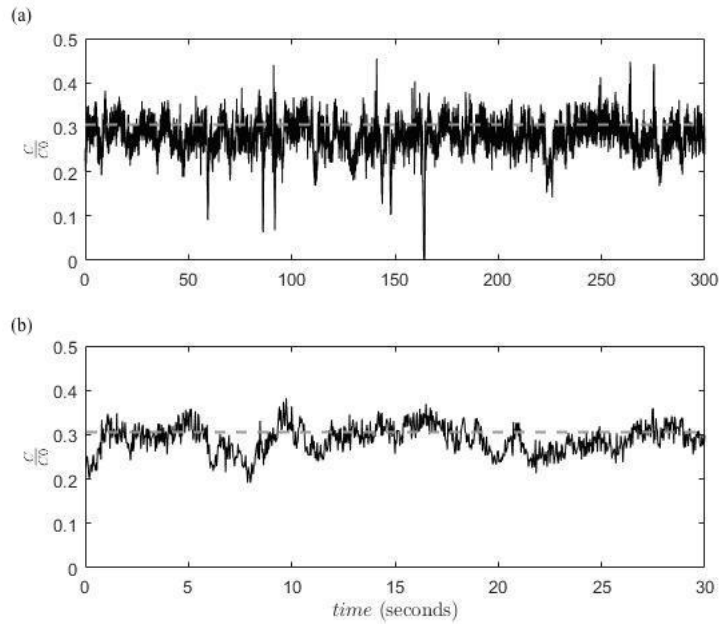


Figure 3.24: Time series over periods of (a) 5 minutes and (b) 30 seconds at  $z=0$  mm,  $y=-8$  mm,  $x=40$  mm. Mean concentration shown with dashed line.

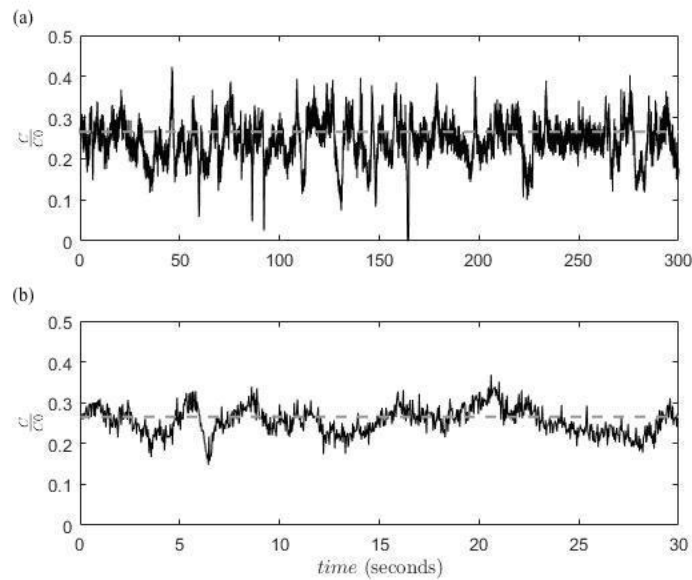


Figure 3.25: Time series over periods of (a) 5 minutes and (b) 30 seconds at  $z=0$  mm,  $y=-16$  mm,  $x=70$  mm. Mean concentration shown with dashed line.

this anomaly does exist, the spread and extent of the near boundary data was so different than the unbounded it is expected that trend is true, and thus merits being shared for comparison.

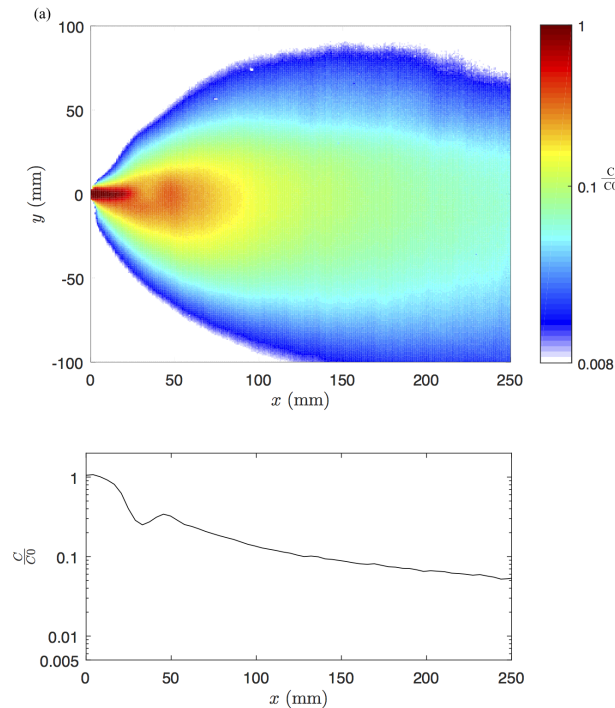


Figure 3.26: (a) Normalized mean concentration of bounded plume, with (b) corresponding stream-wise profile at  $y=0$  mm.

In the lateral profiles of the mean concentration bounded data (Fig. 3.27), a similar spread is observed at 10 mm downstream of the source to that in the unbounded data. However, in the bounded data the magnitude in the spread is much higher, with the peak at source concentration, whereas in the unbounded data the peak concentration was 60% of the source. At 60 mm downstream the plume has spread over a factor of 2 times more in bounded data than the unbounded. The bounded plume persists much farther downstream with a spread of 200 mm at 150 mm downstream, whereas in the unbounded data no detectable signal is present at that distance. This is due to the boundary layer providing a bed for concentrations to persist at higher consistent values, whereas in the unbounded data filaments quickly mix out with no boundary to inhibit that mixing.

In Fig. 3.28a. the RMS of the bounded data has a similar spread to that of its mean, which is not observed in the unbounded data. In the bounded data the consistent concentrations that

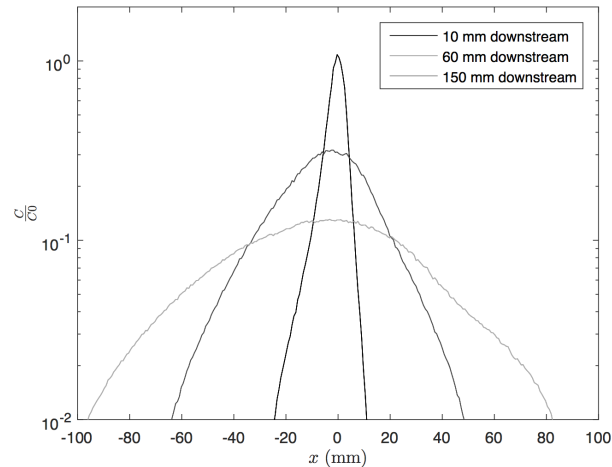


Figure 3.27: Lateral profiles of mean concentration plume at  $x=10$  mm,  $x=60$  mm, and  $x=150$  mm downstream.

persist downstream result in a RMS of similar structure since there are less variations at each location. The structure of the RMS plume also varies greatly compared to that of the unbounded data, with more asymmetrical behavior, following no smooth gradient as observed in the unbounded data. This is likely due to two factors. First, the plume is not as symmetrical about the tube as it is in the unbounded data. The ability to capture perfectly symmetrical plumes is difficult in experiments, and adding a boundary next to the tube complicates this as any small variations in elevation of the bed can significantly bias the plume. As for not having as smooth as a gradient in the unbounded data, this likely involves the influence of the non-monotonic deviation observed in the mean plume.

The RMS centerline structure also decreases at a slower rate than observed in the unbounded data, consistent with trend of persisting downstream concentrations in the bounded data. The lateral profiles in Fig. 3.29 have a wider spread than observed in the unbounded data, and slightly wider spread than that in the time-averaged bounded data. The RMS also persists farther downstream in the bounded than in the unbounded data, with values close to  $0.03C_0$  at 150 mm downstream.

A comparison of the time-averaged and RMS centerline structure (Fig. 3.30) of the bounded

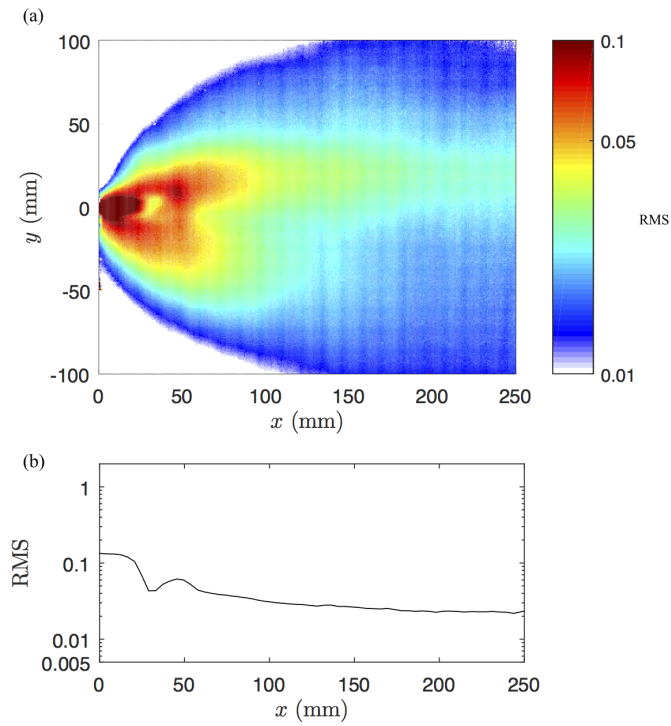


Figure 3.28: (a) normalized RMS of plume with (b) corresponding centerline profile at  $y=0$  mm.

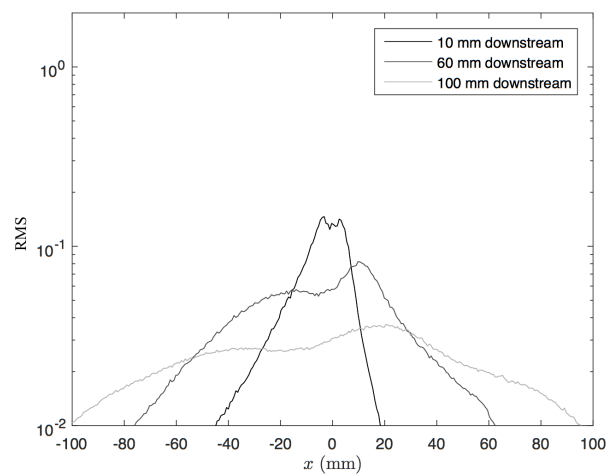


Figure 3.29: Lateral profiles at  $x=10$  mm,  $x=60$  mm, and  $x=150$  mm.



data reveals a parallel structure, differing from the unbounded data where the centerlines intersect early on. In the bounded data the time-averaged centerline remains almost a full order of magnitude above the RMS, only with noticeable beginning of convergence farther downstream at 250 mm. This is very different from the unbounded data where the RMS became a more robust metric after 40 mm downstream, instead in the bounded data the mean remains a more robust metric throughout the entire frame. This is consistent with previous differences where the plume is much more consistent in the bounded time-averaged image versus the unbounded time-averaged image.

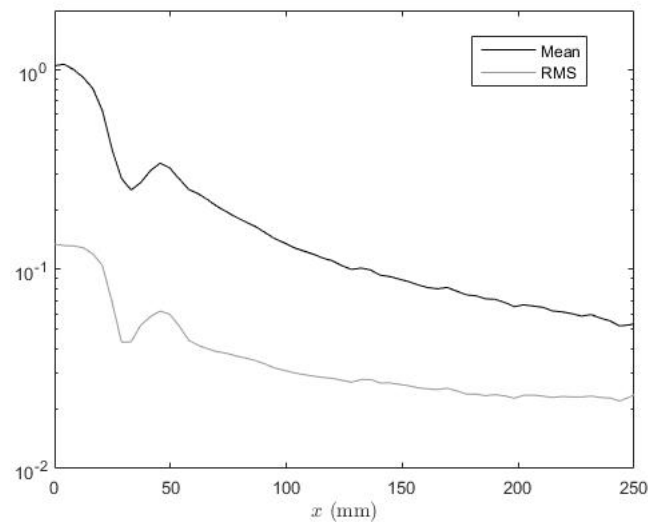


Figure 3.30: Centerline comparison of time-averaged and RMS centerline.

The last statistical metric, intermittency, is profoundly different in the bounded data, than the unbounded data due to the more consistent plume similarly observed in the other metrics. Fig. 3.31 has extremely high consistent value of 1 down the centerline of the plume, until the very end of the frame where it decreases to 0.9 at 250 mm. In the unbounded data the intermittency decreased from 1 after 20 mm, and reached zero at 100 mm downstream. In Fig 3.32 the lateral profiles of intermittency show top hat behavior over a significantly longer distance than observed in the unbounded data, where a value of 1 only lasted for 8 mm at 10 mm downstream. In the bounded data it lasts for a similar distance of 8 mm at 10 mm downstream, but with no sharp gradient drop off to zero, and instead has a gradual decline towards 0 once reaching the edge of the plume over

80 mm. The lateral spread of the intermittency at 60 mm downstream of the source shows a top hat value of 1 over 80 mm, gradually decreasing to 0 over 140 mm, whereas in the unbounded data intermittency is close to 0.5 at 60 mm downstream decreasing to zero over over 40 mm. Similar to the time-average and RMS lateral spreads, the intermittency also persists farther downstream than observed in the unbounded data. The values at 150 mm downstream exhibit “top-hat” behavior with values of 1 persisting over 120 mm laterally, whereas in the unbounded data no detectable values exists at 150 mm downstream.

Similarly in Fig. 3.33 and 3.34 contours for two intermittency values of  $\gamma = 0.5$ , and  $\gamma = 0.1$  over the same varying concentration thresholds cover more spatial area than in the unbounded data. This is consistent with Fig 3.31 in that the probability of encountering a concentration covers a much larger spatial area than it does in the unbounded data. In respect to olfactory navigation this means that organisms tracking a scent would have access to the same concentration information farther downstream and laterally from the source in the bounded data than they would in the unbounded data.

Lastly, 9 time-series and pdfs were plotted in the bounded data covering a larger spatial area than in the unbounded data , shown on a map in Fig. 3.35. Consistent throughout all the time-series (Fig. 3.36) is that the concentration rarely reaches values of zero, except for the two lateral locations closest to the source. This differs greatly from the unbounded data time series, which had spikes of non-zero concentration next to values of zero concentration at most locations. Fig. 3.37 also differs from the unbounded data, with a majority of distributions being normal pdfs, centered around around non-zero means, which is consistent with the other reported bounded data behavior. This normal distribution is due to the less frequent occurrence of zero concentration values, due to the bed inhibiting the mixing behavior that is present in the unbounded case. For example, in the two cases with concentration values reaching zero in Fig. 3.37, the corresponding pdf panels show deviation from normal distributions due to the more frequent occurrence of zero values, which skews the data’s statistical distribution from normal.

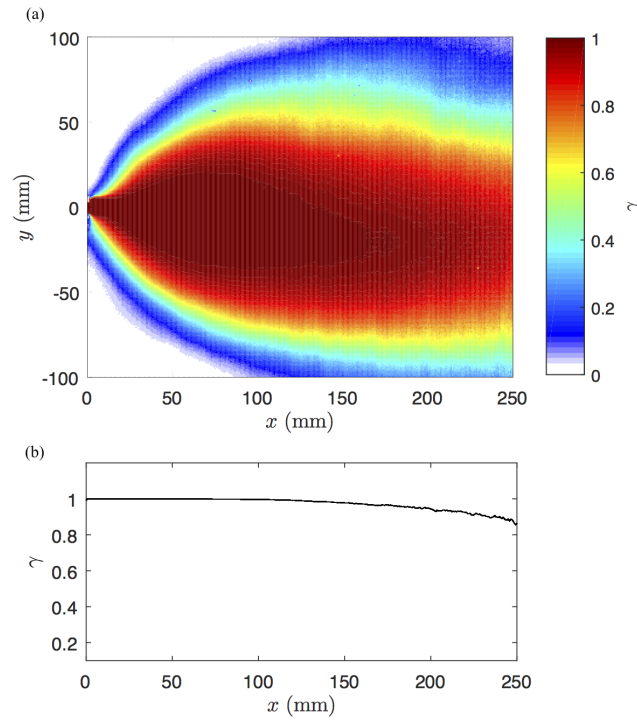


Figure 3.31: (a) Intermittency for  $C_T = 0.03C_0$  with (b) corresponding centerline profile at  $y=0$  mm.

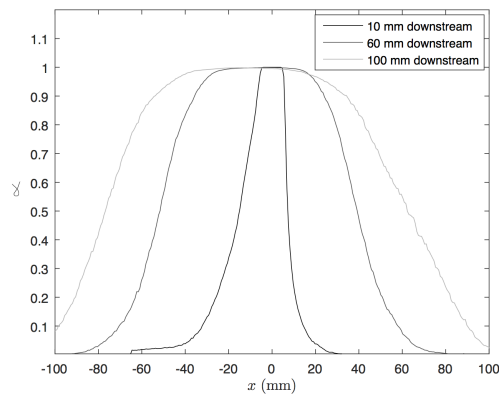
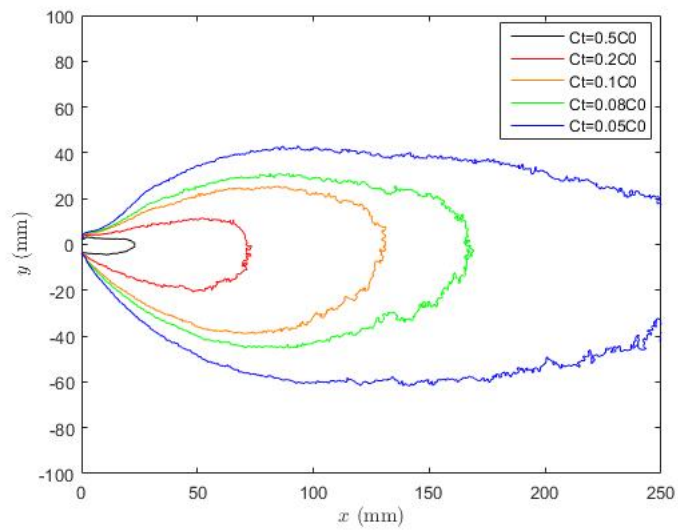
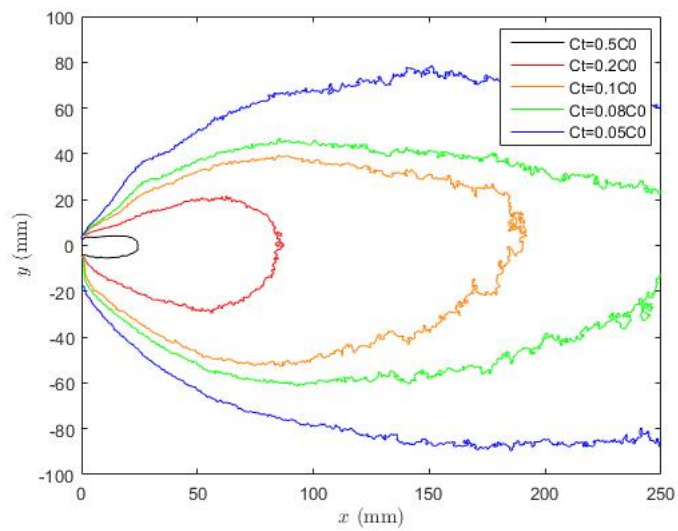


Figure 3.32: Lateral profiles of intermittency at  $x=0$  mm,  $x=60$  mm, and  $x=150$  mm.

Figure 3.33: Contours of  $C_T$  for  $\gamma = 0.5$ .Figure 3.34: Contours of  $C_T$  for  $\gamma = 0.1$ .

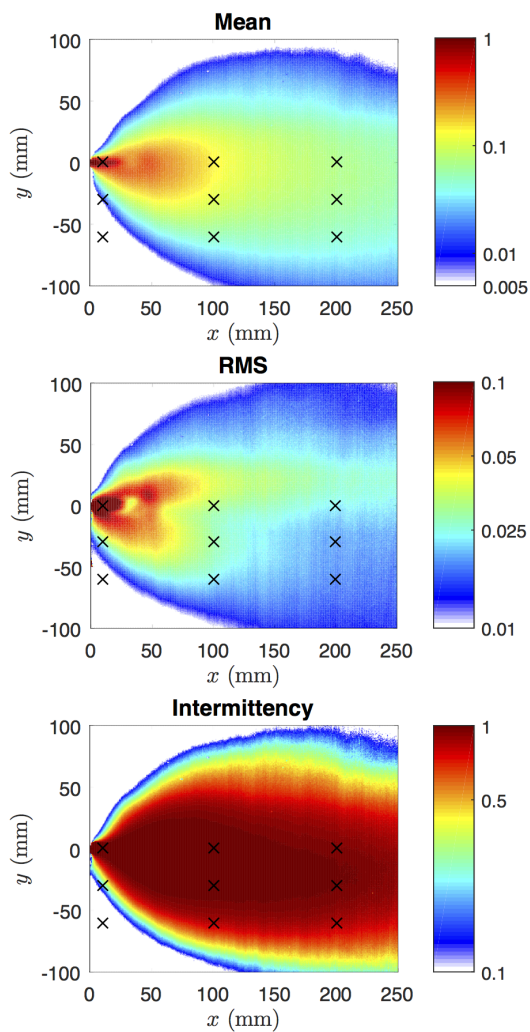


Figure 3.35: Map of time series locations in relation to each statistical measure.

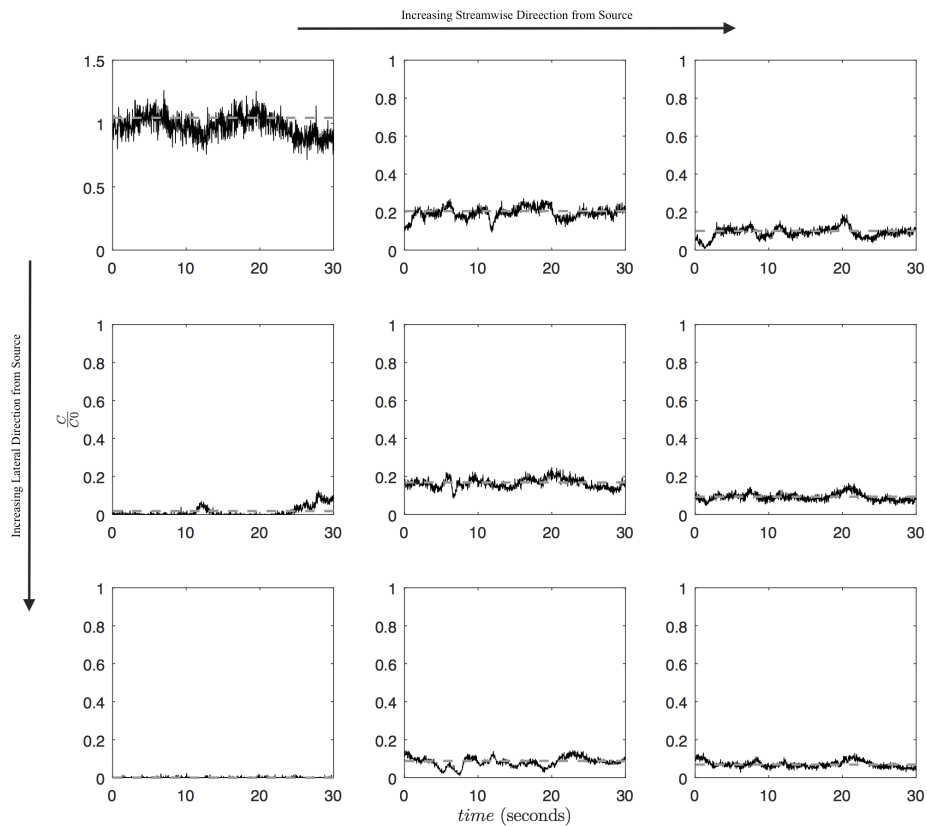


Figure 3.36: Representative time-series of instantaneous normalized concentration for each of the nine locations shown in Fig. 3.35.

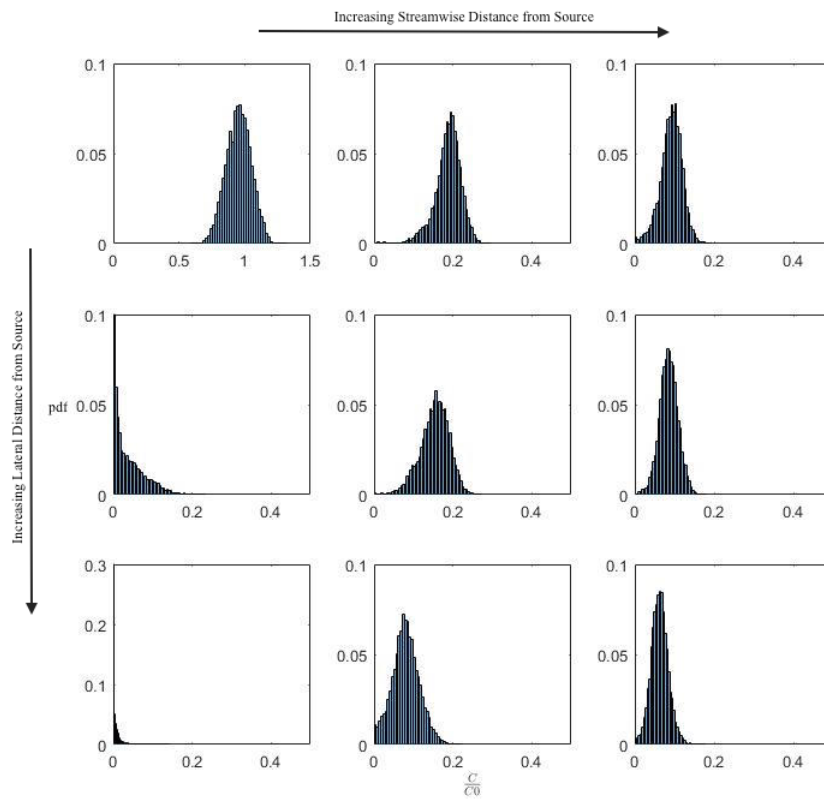


Figure 3.37: Representative pdfs of instantaneous normalized concentration for each of the nine locations shown in Fig. 3.35.

## Chapter 4

### Summary

#### 4.1 Conclusion

A new adaptation of acetone PLIF has been successfully implemented for quantifying gaseous plume behavior. The modified acetone PLIF method has diverged from previous studies by working in the plume data realm, with isokinetic releases at low speeds, over large spatial areas. To be successful a few key components were altered, such as the flow apparatus design and buoyancy correction, to collect plume-like data. The design and implementation of this system has provided the necessary experience and insight into how to design a more robust experimental apparatus, and enhance the quality of data captured. While this method has contributed to the experimental fluid mechanics community, the data is also relevant to work on olfactory navigation, and has helped researchers visualize and quantify the structure of plumes in relation to odor tracking. The two datasets collected here provide the instantaneous visualization to understand the raw signal animals may encounter and the statistical analysis which help inform us about the ecological relevance. This baseline data has provided a deeper understanding of what to expect in gaseous plume behavior, and given the multidisciplinary team we work with the ability to begin to analyze how an animal may use this signal.

#### 4.2 Ecological Significance

In olfactory navigation organisms utilize the instantaneous plume signal to make decisions when navigating an odor plume. The instantaneous data provides insight into the structure and be-



havior of the plume signal, allowing the quantification and visualization of instantaneous structure. While the native instantaneous signal is useful for understanding the signal the animal encounters, relevant statistical measures of plume behavior are also important as they offer different perspectives of the information embedded in the plume. The different statistical measures chosen in this thesis all aid in understanding plume behavior in relation to ecological decisions. For example, it is suggested that some animals adapt to the mean concentration in the plume, and have the ability to sense and utilize the concentration fluctuations from the mean to locate the source. To better understand these animals, the RMS becomes a very important metric as this provides more information about the fluctuations of the concentration from the mean. Another example, is that any animal detecting an odor or other chemical stimulus will have some finite threshold, and the intermittency tells us the spatial extent of the plume for different concentration thresholds. Therefore, intermittency and probability spatial plots give us valuable information for different concentration thresholds and can help in describing olfactory navigation in different species. The mean plume can provide information in the average spatial differences in concentration from the source, and is used in the statistics calculations to understand the average behavior of the plume. In some locations the mean is a good estimate of the concentration, and in others it is not, and this is dependent upon boundary condition layers and location in the plume. Lastly, the pdfs of concentration values at varying downstream and lateral locations along the plume help understand the probability and distribution of concentrations from which an animal may sampling. This also helps in analyzing animal decision making behavior while navigating a plume, as the likelihood and statistical spread of encountering different concentrations changes at different locations. It is clear that while the instantaneous data is the native signal, the statistical measures can provide valuable insight into both the plume and animal behavior.

The data reported here has been shared with a team of researchers who are using it in animal based experiments, virtual environments, and computer algorithms. For example, a team at Weill Cornell Medical College is using these data to simulate animal tracking behavior in computer models. Previously, they had no information on what a realistic gaseous plume would look like,

and so these data gives them more confidence in their results. Researchers at Berkley are using these data to conduct virtual reality environment experiments with human subjects. Here they use the data in a computer simulation where humans use visual and audio cues to make decisions to find the plume source. Their results are paths along the simulation in which each human took to locate the source if successful, this is providing interesting insight into how we as humans make decisions when tracking an “virtual” odor. Experiments using genetically altered organisms, such as mice and flies, are also being designed to examine how vertebrates brains respond neurologically to odor cues. Here the goal is to map the neurological response to odor cues in order to help understand the decision making process of olfactory navigation as well as offer a detailed looked at the neuron capabilities in the brain.

### 4.3 Future Considerations

The tunnel designed for these experiments offered the capability of collecting relevant and useful data to be shared with collaborators across the country. The next step is to capture more data for this team under varying flow constraints and nozzle releases. In order to do this successfully, there are many improvements that can be made to the wind tunnel, to increase longevity and help improve the overall quality of the data captured. This first and arguably most important improvement to be made is to design and construct a recirculating closed loop wind tunnel. Recirculating the air in the tunnel allows for more control over air flow, and temperature, both of which can aid in data capturing and post processing improvements. First, heating the recirculating tunnel will allow a signal increase of up to a factor of 4. Since vapor pressure is temperature dependent, increasing temperature increases the vapor pressure acetone can be seeded, and therefore increases the fraction of acetone seeded into the flow. This is done much more easily in a recirculating wind tunnel since the air being reused in the tunnel is a small volume, which can be heated to the desired temperature and fixed to remain constant using thermocouples. The second improvement is to better understand and quantify the effects of Beer’s Law. Right now, it is assumed absorption due to Beer’s Law is negligible in the data, an assumption past acetone PLIF studies have also made.

And while it may not affect these data sets, under different flow and release conditions the effects may become more apparent as path lengths or concentrations increase. Therefore, having this new tunnel to conduct absorption experiments in and quantify the coefficient of absorption will help correct the data in post-processing and provide more accurate results. Next, a characterization of the shot-to-shot noise of the laser would help reduce the noise floor in the data, and increase downstream SNR levels. Currently, a power meter with the capabilities of recording and correcting for shot-to-shot noise exists. However, a signal loss is taken since it samples 8% of the beam in each shot, and is why it was not used for this data. However, having a heated recirculated tunnel allows for an increase in signal such that the loss from this power meter would not be as significant as it is in the current set up. Lastly, the recirculating wind tunnel will also allow for a more controlled flatfield of the data, since the recirculation of the air will ensure a well-mixed flow of acetone to take repeated and controlled flatfield images. This can also improve the quality of data, and reduce noise if the flatfield is taken over longer periods of time than currently available. These improvements were identified after this first implementation of acetone PLIF in a low speed wind tunnel. Understanding all the factors at play in the tunnel is vital for improvement and robustness of the facility. Making these improvements will greatly improve the quality of the wind tunnel and data, so new experiments and exciting experiments can be completed with more certainty and greater ease.

## Bibliography

- [1] J. Adler. Chemoreceptors in bacteria. Science, 166:1588–1597, 1969.
- [2] F.A. Beach, M.G. Buehler, and I.F. Dunbar. Development of attraction to estrous females in male dogs. Physio. Behav., 31:293–297, 1983.
- [3] R.A. Becker. Meet the giant rats that are sniffing out landmines. National Geographic, 2015.
- [4] J.H. Bell and R.D. Mehta. Contraction design for small low-speed wind tunnels. JIAA, 1988.
- [5] K.K. Bharadwaj, D. Das, and P.K. Sharma. Near field characteristics of buoyant plumes. Sadhana, 40(3):757–768, 2015.
- [6] W.H. Bossert and E.O. Wilson. The analysis of olfactory communication among animals. J. Theor. Biol., 5:443–469, 1963.
- [7] J.M. Bowers and B.K. Alexander. Mice: individual recognition of olfactory cues. Science, 158:1208–1210, 1967.
- [8] R.A. Bryant, J.M. Donbar, and J.F. Driscoll. Acetone laser induced fluorescence for low pressure/low temperature flow visualization. Exp. in Fluids., 28:471–476, 2000.
- [9] E. Bursell. Observations on the orientation of tsetse flies (*glossina pallidipes*) to wind-borne odours. Physio. Entomol., 9:133–137, 1984.
- [10] R. Camilli, C.M. Reddy, D.R. Yoerger, B.A.S. Van Mooy, M.V. Jakuba, J.C. Kinsey, C.P. McIntyre, S.P. Sylva, and J.V. Maloney. Tracking hydrocarbon plume transport and biodegradation at deepwater horizon. Science, 330:201–204, 2008.
- [11] R.T. Carde and M.A. Willis. Navigational strategies used by insects to find distant, wind-borne sources of odor. J. Chem Ecol, 34:854–866, 2008.
- [12] K.C. Catania. Stereo and serial sniffing guide navigation to an odour source in a mammal. Nature, 4:1208–1210, 2013.
- [13] Stephanie Chen. Puppies train to smell bombs, narcotics and missing people. CNN, 2009.
- [14] JP Crimaldi. Planar laser induced fluorescence in aqueous flows. J.P. Exp Fluids, 44:851, 2008.
- [15] J.P. Crimaldi, M.B. Wiley, and J.R. Koseff. The relationship between mean and instantaneous structure in a turbulent passive scalar. J Turbul, 3:014, 2002.

- [16] P.H. Daum, L.I. Kleinman, L. Newman, W.T. Luke, W. Weinstein-Lloyd, C.M. Berkowitz, and K.M. Busness. Chemical and physical properties of plumes of anthropogenic pollutants transported over the north atlantic during the north atlantic regional experiment. J. Geophys. Res. Atmos., 101:29029–29042, 1996.
- [17] Noel de Nevers. Air Pollution Control Engineering. Waveland Pr Inc, Long Grove, Illinois, 2010.
- [18] R.L. Doty. Odor-guided behavior in mammals. Experientia, 42(3):349–375, 1986.
- [19] ADM. Dove. Foraging and ingestive behaviors of whale sharks, rhincodon typus, in response to chemical stimulus cues. Biol. Bull., 228:65–74, 2015.
- [20] A. Gomez-Marin, B.J. Duistermars, M.A. Frye, and M. Louis. Mechanisms of odor-tracking: Multiple sensors of enhanced perception and behavior. Front. Cell. Neurosci., 4:6, 2010.
- [21] R.K. Hanson and J.M. Seitzman. Handbook of Flow Visualization. Hemisphere Pub. Corp., Carlsbad, CA, 1989.
- [22] E.S. Hodgson and R.F. Matthewson. Chemosensory orientation in sharks. Ann. N.Y. Acad. Sci., 188:175–182, 1971.
- [23] J. Jackson, D.R. Webster, S. Rahman, and M.J. Weissburg. Bed-roughness effects on boundary-layer turbulence and consequences for odor-tracking behavior of blue crabs. Limnol. Oceanogr., 52:1883–1897, 2007.
- [24] C.D. Jones. On the structure of instantaneous plumes in the atmosphere. Jour. Hazard. Mater., 7:87–112, 1983.
- [25] W. Kalkowski. Visual control of social environment in the white mouse. Folia biol. Krawkow, 16:215–233, 1968.
- [26] T. Kurian and J.H.M. Fransson. Grid-generated turbulence revisited. Fluid Dyn. Res., 41:32pp, 2009.
- [27] G. Kychakoff, K. Knapp, R.D. Howe, and R.K. Hanson. Flow visualization in combustion gases using nitric oxide fluorescence. AIAA, 22:153–154, 1984.
- [28] Q. Liao and E.A. Cowen. The information content of a scalar plume- a plume tracing perspective. Environ. Fluid. Mech., 2:9–34, 2002.
- [29] J.B. Liu, Q. Pan, C.S. Liu, and J.R. Shi. Principles of flow field diagnostics by laser-induced biacetyl phosphorescence. Exp. in Fluids., 6:505–513, 1988.
- [30] M. Louis, T. Huber, R. Benton, T.P. Sakmar, and L.B. Vosshall. Bilateral olfactory sensory input enhances chemotaxis behavior. Nat. Neurosci., 11:187–199, 2008.
- [31] A. Lozano, M. Smith, G. Mungal, and R.K. Hanson. Concentration measurements in a transverse jet by planar-laser induced fluorescence of acetone. AIAA, 32:218–221, 1994.
- [32] A. Lozano, B. Yip, and R.K. Hanson. Acetone: a tracer for concentration measurements in gaseous flows by planar laser-induced fluorescence. Exp. in Fluids., 13:369–376, 1992.

- [33] A. Mafra-Neto and T.C. Baker. Elevation of pheromone response threshold in almond moth males pre-exposed to pheromone spray. Physio. Entomol., 21:217–222, 1996.
- [34] A. Mafra-Neto and R.T. Carde. Fine-scale structure of pheromone plumes modulates upwind orientation of flying moths. Letters to Nature, 360:142–144, 1994.
- [35] A. Mafra-Neto and R.T. Carde. Measurement of odor-plume structure in a wind tunnel using a photoionization detector and a tracer gas. Environ. Fluid Mech., 2:115–142, 2002.
- [36] A. Mafra-Neto and R.T. Carde. Influence of plume structure and pheromone concentration on upwind flight of *cadra cautella* males. Physio. Entomol., 20:117–133, 2008.
- [37] C.N. Markides and E. Mastorakos. Measurements of scalar dissipation in a turbulent plume with planar laser-induced fluorescence of acetone. Chem. Eng. Sci., 61:2835–2842, 2006.
- [38] C.N. Markides and E. Mastorakos. Measurements of scalar dissipation in a turbulent plume with planar laser-induced fluorescence of acetone. Chem. Eng. Sci., 90:221–241, 2013.
- [39] M.M. Metzger and J.C. Klewicki. Development and characterization of a probe to measure scalar transport. Meas. Sci. Technol., 14:1437–1448, 2003.
- [40] P. Moore and J.P. Crimaldi. Odor landscapes and animal behavior: tracking odor plumes in different physical worlds. J. Mar. Syst., 49:55–64, 2004.
- [41] P.A. Moore and J. Grills. Chemical orientation to food by the crayfish, *orconectes rusticus*: influence by hydrodynamics. Anim. Behav., 58:953–963, 1999.
- [42] P.A. Moore, N. Scholz, and J. Atema. Chemical orientation of lobsters, *homarus americanus*, in turbulent odor plumes. J.J Chem. Ecol., 3:1293, 1991.
- [43] J. Murlis, J.S. Elkington, and R.T. Carde. Odor plumes and how insects use them. Annu.Rev.Entomol., 37:505–532, 1992.
- [44] J. Murlis and C.D. Jones. Fine-scale structure of odour plumes in relation to insect orientation to distant pheromone and other attractant sources. Physio. Entomol., 6:71–86, 1981.
- [45] J. Murlis and C.D. Jones. Fine-scale structure of odour plumes in relation to insect orientation to distant pheromone and other attractant sources. Physio. Entomol., 6:71–86, 1981.
- [46] J. Murlis, M. Willis, and R. Carde. Spatial and temporal structures of pheromone plumes in the fields and forest. Physiol Entomol, 25:211–222, 2000.
- [47] P.H. Paul, J.M. Seitzman, and R.K. Hanson. Planar laser-fluorescence imaging in combustion gases. App.Phys, B50:441–454, 1990.
- [48] S. Pichon, G. Black, N. Chaumeix, M. Yahyaoui, and J.M. Simmie. The combustion chemistry of a fuel tracer: Measured flame speeds and ignition delays and a detailed chemical kinetic model for the oxidation of acetone. Combust. Flame, 156(2):273–546, 2009.
- [49] M.A. Reidenback and M.A.R. Koehl. The spatial and temporal patterns of odors sampled by lobsters and crabs in a turbulent plume. J. Exp. Biol., 214:3138–3153, 2011.

- [50] B.D. Ritchie and J.M. Seitzman. Mixing in coaxial jets using synthetic jet actuators. 38th AIAA Meeting, Reno, NV., 2000.
- [51] B.D. Ritchie and J.M. Seitzman. Quantitative acetone plif in two-phase flows. 39th AIAA Meeting, Reno, NV., 2001.
- [52] B.D. Ritchie and J.M. Seitzman. Simultaneous imaging of vapor and liquid spray concentration using combined acetone fluorescence and phosphorescence. 42nd AIAA Meeting, Reno, NV., 2004.
- [53] Y. Sakai, K. Nagata, H. Suzuki, and Y. Ito. Mixing and diffusion in a regular/fractal grid turbulence. CISM International Centre for Mechanical Sciences., 568:17–73, 2016.
- [54] C. Schulz and V. Sick. Tracer-lif diagnostics: quantitative measurement of fuel concentration, temperature, and/or fuel/air ratio in practical combustion systems. Prog. Energy Combust. Sci., 31(1):75–121, 2005.
- [55] J.M. Seitzman, A. Ungut, P.H. Paul, and R.K. Hanson. Imaging and characterization of oh structures in a turbulent nonpremixed flame. AIAA, 22:153–154, 1984.
- [56] S.H. Smith and M.G. Mungal. Mixing, structure and scaling of the jet in crossflow. J. Fluid. Mech., 357:83–122, 1998.
- [57] L Su and N. Clemens. Planar measurements of the full three-dimensional scalar dissipation rate in gas-phase turbulent flows. Expts. Fluids., 27:507–521, 1999.
- [58] W. Sullivan. Truffles: Why pigs can sniff them out. New York Times., 1982.
- [59] M.C. Thurber, F. Grisch, and R.K. Hanson. Temperature imaging with single- and dual-wavelength acetone planar laser-induced fluorescence. Opt. Lett., 22:251–253, 1997.
- [60] M.C. Thurber, F. Grisch, B.J. Kirby, M. Votsmeier, and R.K. Hanson. Measurements and modeling of acetone laser-induced fluorescence with implications for temperature-imaging diagnostics. Appl. Opt., 37:4963–4978, 1998.
- [61] Thao T. Tran. Acetone Planar Laser-Induced Fluorescence and Phosphorescence for Mixing Studies of Multiphase Flows. PhD thesis, Georgia Institute of Technology, 2008.
- [62] J. Trost, M. Loeffler, L. Zigan, and A. Leipertz. Simultaneous quantitative acetone-plif measurements for determination of temperature and gas composition in an ic-engine. Phys. Procedia., 5:689–696, 2010.
- [63] R.S. Vetter, A.E. Sage, K.A. Justus, R.T. Carde, and C.G. Galizia. Temporal integrity of an airborne odor stimulus is greatly affected by physical aspects of the odor delivery system. Chem. Senses., 31:359–369, 2006.
- [64] N.J. Vickers. Mechanisms of animal navigation. Biol. Bull., 198:203–212, 2000.
- [65] D.R. Webster, S. Rahman, and L. P. Dasi. On the usefulness of bilateral comparison to tracking turbulent chemical odor plumes. Limnol. Oceanogr., 46:1048–1053, 2001.
- [66] D.R. Webster, S. Rahman, and L.P. Dasi. Laser-induced fluorescence measurements of a turbulent plume. Jour. Eng. Mech., 129:1130–1137, 2003.

- [67] D.R. Webster and M.J. Weissburg. Chemosensory guidance cues in a turbulent chemical odor plume. Limnol. Oceanogr., 46(5):1034–1047, 2001.
- [68] M. Weissburg and R.K. Zimmer-Faust. Life and death in moving fluids: Hydrodynamic effects on chemosensory-mediated predation. Ecol., 74:1428–1443, 1993.
- [69] M. Weissburg and R.K. Zimmer-Faust. Odor plumes and how blue crabs use them in finding prey. J.exp. Biol., 197:349–375, 1994.
- [70] B. Yip, M.F. Miller, A. Lozano, and R.K. Hanson. A combined oh/acetone planar laser-induced fluorescence imaging technique for visualizing combustion flows. Expts. Fluids., 17:330–336, 1994.



## Appendix A

### Acetone Vapor Chemistry

#### A.1 Full Flow Saturation

In order to ensure that enough flasks are being used to reach a maximum saturation of acetone in the seeded flow, the addition of flasks to the system is plotted versus counts in an image of jet core. We can see that there is only a significant difference between the addition of a second flask from one flask. Any other addition of flasks does not statistically increase the mean signal in the flow.

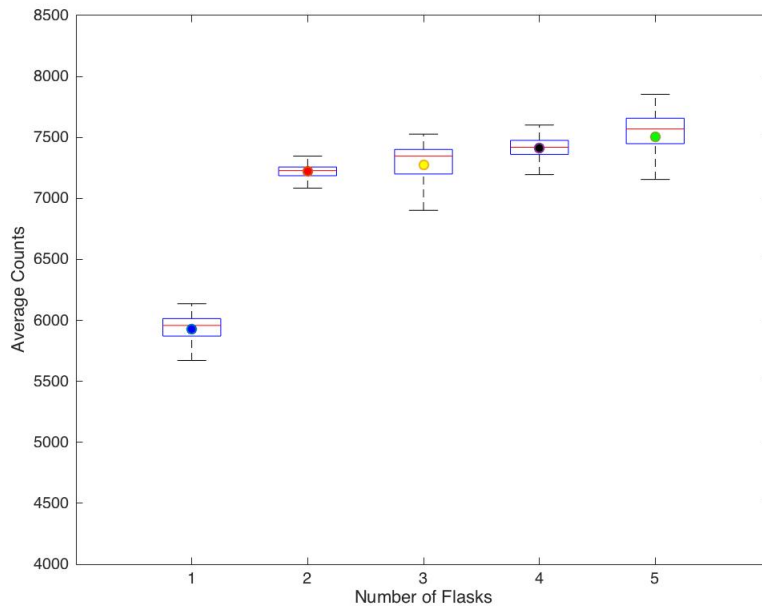


Figure A.1: Addition of flasks to system to reach maximum saturation

To ensure that acetone vapor was being seeded into the flow rate at constant proportions over time, images of a jet core were taken over approximately 8 minutes at 2Hz, and corresponding average signal counts were reported. In Figure A.2. it is evident no significant decrease in average counts occurred, therefore ensuring constant seeding over acetone vapor over time.

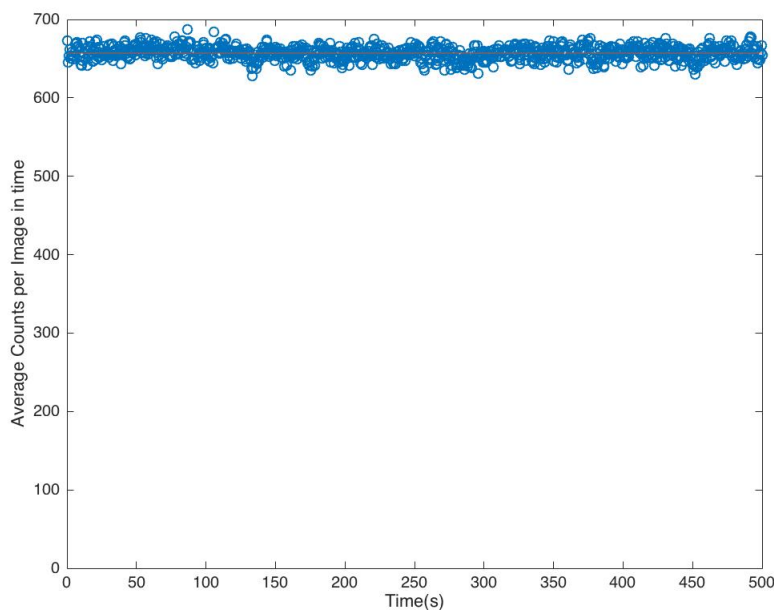


Figure A.2: Measurements over average counts over 8 minutes to ensure constant seeding

## A.2 Temperature dependence on vapor pressure

Vapor pressure is dependent upon the substance as well as the temperature at which the liquid and vapor are coming to equilibrium. Therefore, if temperature were increased, the vapor pressure would also increase non-linearly. As seen in using Raoult's Law, an increase in vapor pressure would result in an increase in seeding percentage of acetone, thus higher signal in the data. Below is a normalized plot of Temperature vs. Vapor Pressure of acetone, calculated from the Clausius-Claperyon relationship, where a value of 1 indicates where this data was taken. One can see that by increasing to 55C, the signal could increase by 4.

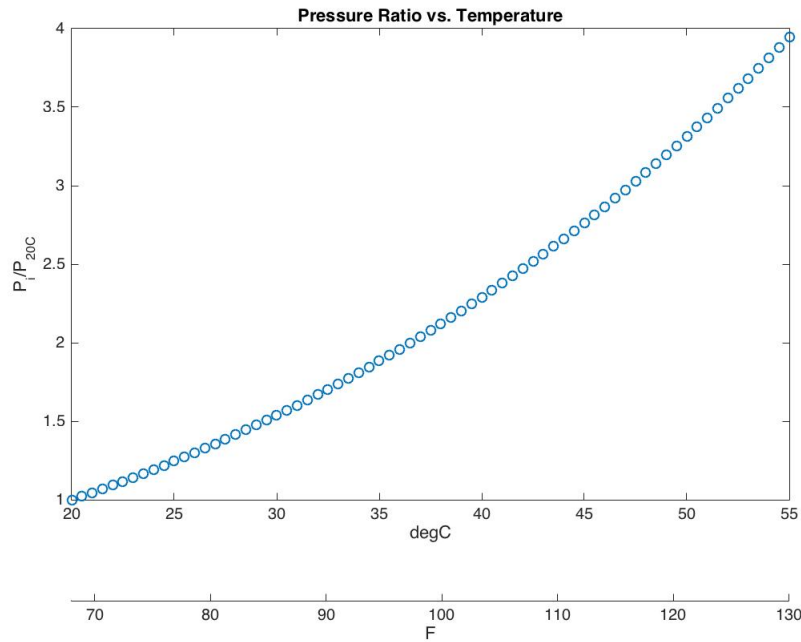


Figure A.3: Vapor pressure vs. temperature, where 1 is the current Pressure ratio using this system.

### A.3 Density Calculations

Reported values of the density of helium, air, and acetone vapor at 5480 ft are solved for below using the ideal gas law.

$$\rho_{helium} = \frac{0.83atm}{82.06 \frac{atm \cdot cm^3}{mol \cdot K} * 293.15K} * 4 \frac{g}{mol}$$

$$\rho_{helium} = 0.138 \frac{kg}{m^3}$$

Density of air is known  $1.001 \frac{kg}{m^3}$  at 20C and pressure of 0.83 atm.

$$P = 0.83atm$$

$$T = 293.15K$$

$$R = 82.06 \frac{atm * cm^3}{mol * K}$$

$$MW_{acetone} = 58.08 \frac{g}{mol}$$

where P is the pressure at Boulder, CO elevation of 5280ft, T is room temperature of the laboratory, and MW is the molecular weight of acetone.

$$\rho = \frac{P}{R * T} * MW$$

$$\rho_{acetonevapor} = \frac{0.83atm}{82.06 \frac{atm*cm^3}{mol*K} * 293.15K} * 58.08 \frac{g}{mol}$$

$$\rho_{acetonevapor} = 2.00 \frac{kg}{m^3}$$

## A.4 Explosive Limits of Acetone Vapor

### A.4.0.1 Background

Under certain conditions the mixture of acetone and air can create an explosive environment. This environment needs two things for an explosion to occur:

- (1) The acetone to air ratio by volume is between 2.2 and 12.8%
- (2) An ignition source

### A.4.0.2 The Perfect Mixture

The acetone to air ratio by volume ( $\frac{VolumeofAcetone}{VolumeofAir} * 100\%$ ) better known as explosive limits are a range of percent by volume mixtures that are conducive to explosive and ignitable gaseous mixtures. Such limits exist for most gaseous compounds and are derived from the fuel:air ratio concepts. This idea comes from the fact that for every gaseous compound there is a range in which the appropriate amount of fuel and air are mixed such that it can create a burn or explosion. If there is too little air (or oxygen) in the system than an explosion or fire cannot occur, while if there is too much oxygen, it can also prevent the fuel from igniting. Thus to prevent explosions and fire we can take preventative steps to ensure the perfect mixture of acetone and air never exists in our wind tunnel.

### **A.4.0.3 An ignition source**

An ignition source can be any source of high energy or friction that could add enough energy to the system to start a flame or explosion. Such examples include:

- (1) Spark
- (2) Laser sheet
- (3) Smoke
- (4) Excessive heat
- (5) Heating elements

Since we do plan on heating our wind tunnel in the future and we are shining a laser through the tunnel to take data we can assume with reasonable cause that we are providing an ignition source for the acetone. Thus our best method of preventing an explosion comes from limiting the acetone in the wind tunnel to ever be between the explosive limits.

### **A.4.1 Wind Tunnel Chemistry**

To ensure that we do not reach the volumetric ratios defined in the above explosive limits, we need to fully understand the chemistry of the system.

#### **A.4.1.1 Relationship of Vapor Pressure and Concentration**

The vapor pressure of a gas is defined as the equilibrium pressure that is exerted by the vapor when it is in equilibrium with its liquid phase. This vapor pressure is highly dependent upon temperature as demonstrated from the ideal gas law:

$$PV = nRT$$

Where we can see that holding all other things constant if temperature (T) increases in a system the pressure (P) increases as well. Thus the temperature at which we seed the airflow with acetone gives us a maximum seeding limit.

#### A.4.1.2 Raoult's Law of Partial Pressures

Raoult's Law of Partial Pressures allows us to relate the total pressure of a system to the vapor pressure of solvent and mole fraction of that solvent in the system.

$$P_{solution} = X_{solvent} * P_{solvent}$$

In our system we have air and acetone. We know that since the system is not pressurized, we can define our atmospheric pressure as the pressure of the total solution thus

$$P_{air} = P_{solution} = 0.83atm$$

which is the atmospheric pressure at 5280 ft above sea level. Next we can use the Antoine Equation relationship, which describes the relationship between temperature and partial pressure of acetone to compute our partial pressure of acetone at room temperature (T=20 C).

$$P = 10^{A-(B/(C+T))}$$

Where A,B,C are defined constants dependent upon the relevant temperature range. So for this scenario:

$$A= 7.13 \quad B= 1220 \quad C= 231$$

Thus at 20C:

$$P_{acetone} = P_{solvent} = 184mmHg = 0.242atm$$

Now we are ready to solve for the mole fraction of our mixture such that:

$$X_{solvent} = \frac{0.242atm}{0.82atm} = 0.29$$

We know from Avogadro's Law that:

$$\frac{V_1}{V_2} = \frac{n_1}{n_2}$$

Since we already know the right hand side of this equation we can then relate the mole fraction to volume fraction such that we can conclude our seeded acetone and air mixture is as follows:

$$\frac{V_{acetone}}{V_{air}} = 0.29 = 29\% \text{ acetone by volume}$$

This value is important because it is our source concentration exiting out the nozzle in our set up. Thus, we know our exit volume percentage is much higher than our explosive limit range mentioned in Section 1. However, this means there is a period of time where we are slowly reaching that lower limit of 2.2% v/v. Thus the next step is to calculate that time.

#### A.4.2 Explosive Time

In order to determine the time it would take to reach the lower limit of our explosive range we need to define the system and parameters involved. Here we can use a well mixed reactor as a model for our system with the following governing equation:

$$\frac{dM}{dT} = R_{in} - R_{out}$$

Where  $M$  is defined as mass, and  $R$  is the rate at which it is entering and exiting the system.

$$R_{in} = Q_{in} * C_o \quad R_{out} = Q_{out} * C_{mix}(t)$$

We can then redefine our well mixed concentration,  $C_{mix}$  as the mass at a specific time divided by the total volume of air in our system. Such that

$$C_{mix}(t) = \frac{M(t)}{V}$$

Note that  $M$  changes with time, since  $C_{mix}$  is also dependent upon time.

Now rearranging we can write equation 1 as follows:

$$\frac{dM}{dT} = Q_{in} * C_o - Q_{out} * \frac{M(t)}{V}$$

We can see that this is a linear differential equation which we can arrange to solve.

$$\frac{dM}{dT} + -Q_{out} * \frac{M(t)}{V} = Q_{in} * C_o$$

And

$$M(t) = \int \frac{u(t)*q(t)dt+K}{u(t)}$$

We can define our function  $u(t)$  as follows:

$$u(t) = e^{\int \frac{Q}{V} dt} \quad (\text{A.1})$$

$$u(t) = e^{\frac{Q}{V}t} \quad (\text{A.2})$$

We know that  $q(t)$  is equal to the following:

$$q(t) = Q * C_o$$

So we can plug back into equation 3 and get:

$$M(t) = \int \frac{e^{QVt}*Q*C_o*dt+K}{e^{\frac{Q}{V}*t}}$$

Which after solving the integral and canceling terms we get:

$$M(t) = C_o * V + K * e^{-\frac{Q}{V}*t}$$

Now to solve for constant  $K$ , we can use an initial condition of  $M(t = 0) = 0$  or in other words at  $t=0$ , there is no acetone in the system.

Plugging that in we get:  $K = -C_o * V$

So plugging back into the final equation and dividing by the volume,  $V$  we can rewrite the solution as  $C_{mix}(t)$  :

$$C_{mix}(t) = C_o * 1 - e^{-\frac{Q}{V}t}$$

Now we can redefine a variable  $t^*$  as follows:

$$t^* = \frac{Q}{V}t$$

We can also break down this relationship further by acknowledging the following:

$$C^* = \frac{C_{mix}}{C_o}$$

We now have a non-dimensional relationship, depicted in Figure 1:  $C^* = 1 - e^{-t^*}$



Specifically we are interested in the time it takes to reach the lower explosive limit. Since these limits we mentioned earlier are 2.2 and 12.8% we are interested in calculating how long it will take to reach the lower limit of 2.2%. In our case we will also add a level of uncertainty, thus we will use our lower explosive limit as 1% v/v. In solving for this time, we can use our non-dimensional relationships to identify how long it will take for the tunnel to be full of 1% of acetone by volume.

If we remember from earlier:

$$C^* = \frac{C_{mix}}{C_o}$$

Thus if our lower limit is 1% we want to solve for when  $C^* = 0.01$ . In the relationship between  $C^*$  and  $t^*$  we see:

$$C^* = 1 - e^{-t^*}$$

So solving for  $t^*$  we see that  $t^* = 0.01$ . This makes sense in Figure 2, as we can see at these  $t^*$  and  $C^*$  values the relationship is highly linear.

Now solving for  $t$  in the  $t^*$  relationship we described earlier, we can use the following relationships:

$$t^* = \frac{Q}{V} * t \quad Q = u * A_{nozzle}$$

where,

$u$  = exit velocity from nozzle

$A_{nozzle}$  = cross sectional area of nozzle

$V$  = total volume of wind tunnel

Taking this further we can redefine volume,  $V$  as:

$$V = A_{windtunnel} * L$$

where  $A_{windtunnel}$  is the cross sectional area of the wind tunnel, and  $L$  is the total length of the wind tunnel.

Now we can substitute in all our known quantities to solve for  $t$ , using our newly rearranged equation:

$$t = \frac{A_{windtunnel} * L}{u * A_{nozzle}} * t^*$$

We know the following:

$$L = 600cm$$

$$A_{windtunnel} = 50cm * 50cm = 2500cm^2$$

$$A_{nozzle} = \pi * 0.476^2 = 0.72cm^2$$

$$u = 5cm/s$$

$$t^* = 0.01$$

Plugging these values in we see that the time it takes to reach 1% v/v is approximately:

$$t = 4.24 * 10^3 \text{ seconds} = 70 \text{ minutes}$$

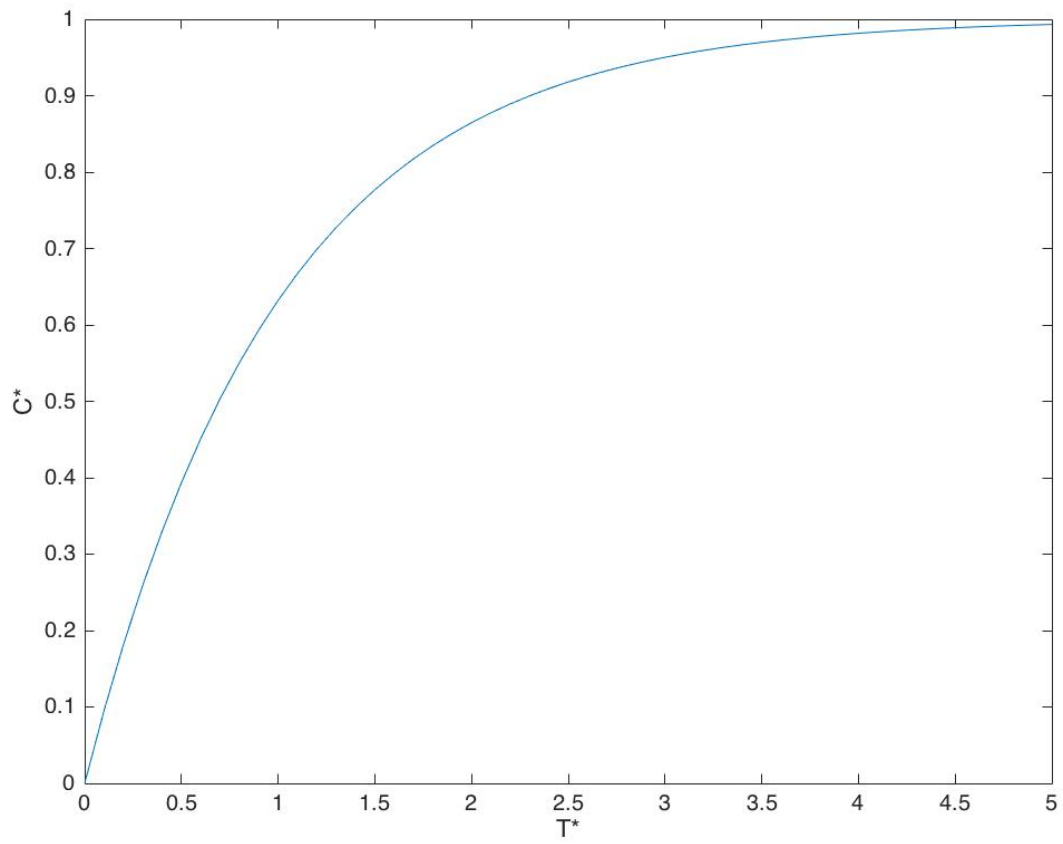


Figure A.4: Non-dimensional relationship of  $C^*$  vs.  $t^*$

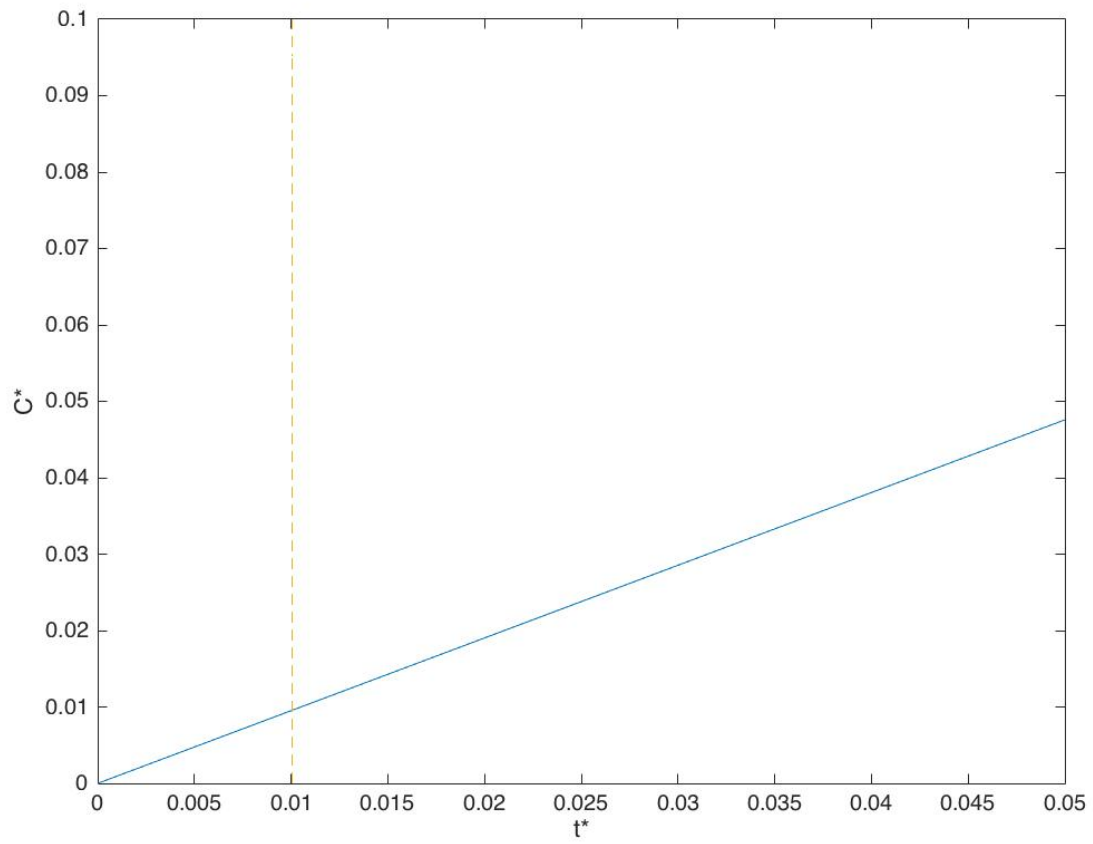


Figure A.5: Specific Non-dimensional relationship of  $C^*$  vs.  $t^*$

## Appendix B

### Saturation of Fluorophore

One important assumption of using the method of planar laser induced fluorescence is that the fluorophore is nowhere near saturation and is in the linear realm. Saturation in this case is when you continue to apply more intensity of laser to a fluorophore and the fluorescence no longer increases, or increases non-linearly most likely near leveling off. This assumption helps with calculations and the mathematics of computing concentrations. Thus for acetone, I fired the laser at varying energies and recorded the fluorescence under each. Below are two plots I created from taking the data twice, along two other published plots showing similar results that the acetone is in the linear regime.

Other published work has examined the linear relationship between power intensity and fluorescence signal. Specifically, two published plots are shown below as example. These are in agreement with the findings in Figures B.1 and B.2.

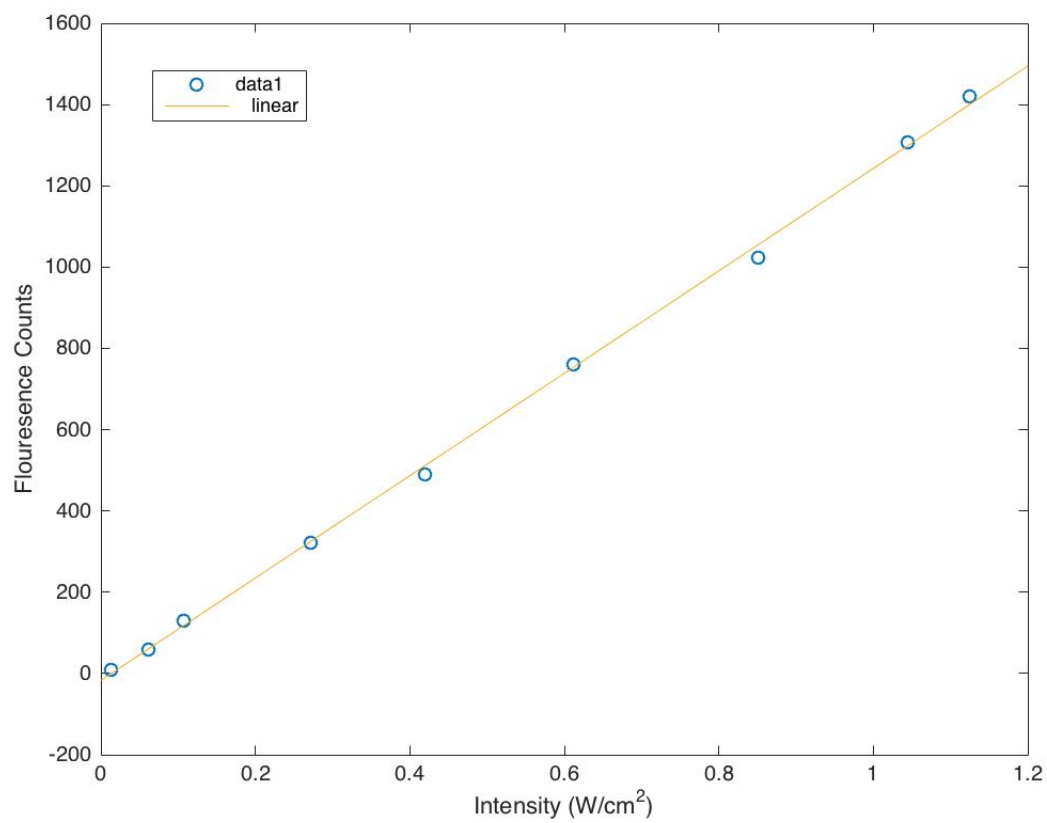


Figure B.1: Fluorescence of Acetone vs. Intensity of Laser Take 1

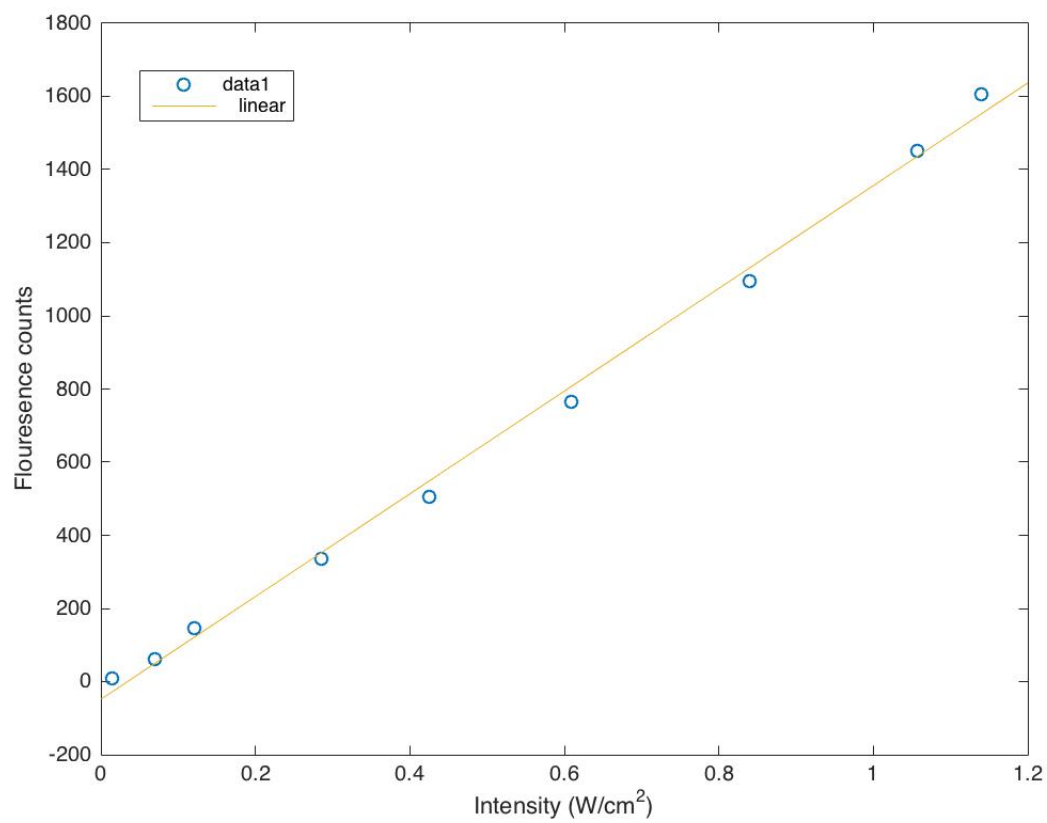


Figure B.2: Fluorescence of Acetone vs. Intensity of Laser Take 2



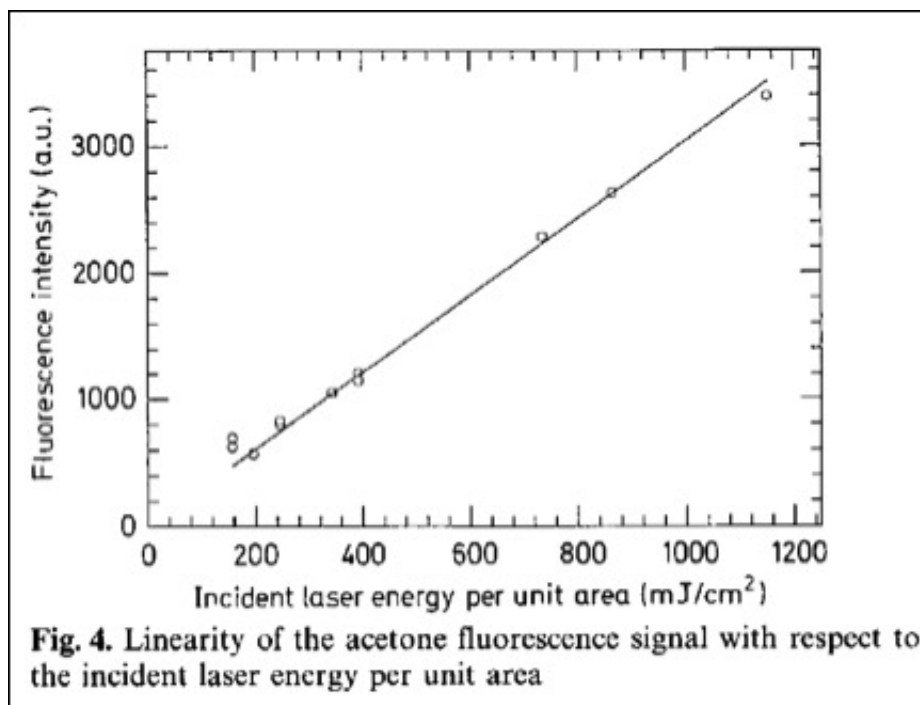


Figure B.3: Fluorescence of Acetone vs. Intensity of Laser [32]

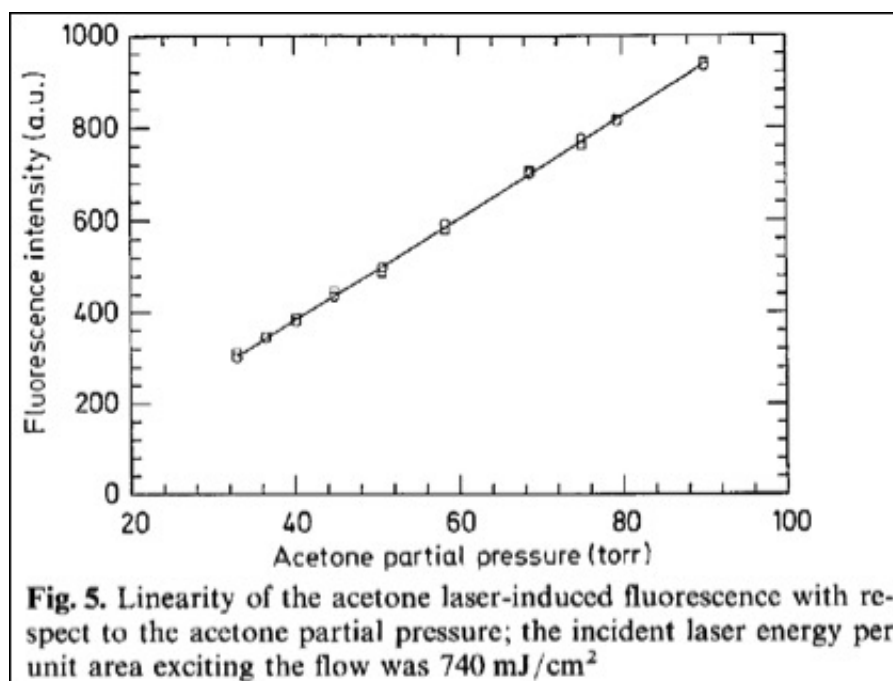


Figure B.4: Fluorescence of Acetone vs. Intensity of Laser [61]

## Appendix C

### Continuous vs. Pulsed Laser

In order to compare pulsed laser and continuous laser, we need to compare in terms of Energy (J). A pulsed laser outputs an energy per pulse, and our laser is double pulsed. Thus the calculation for energy output for the pulsed laser is as follows:

$$\text{Total Energy} = \text{energy per pulse of first head (J)} + \text{energy per pulse of second head (J)}$$

After we find the energy of the pulsed laser we can then calculate our energy for the continuous laser. We can first recognize the relationship between energy and watts relevant to continuous lasers, shown below.

$$\text{Energy} = \text{Watts} * \text{Time}$$

Since we are trying to determine if a continuous wave laser would be better for us than our pulsed laser we can plug in the energy we have for our pulsed laser as a minimum energy we would need in our continuous laser. Next we can define our time as our maximum allowable exposure time (MAET), which we can calculate using the three variables listed below.

- (1) Maximum allowable exposure time (MAET)
- (2) Pixel Size
- (3) FOV
- (4) Flow velocity

Defining these two variables leaves us solving for minimum watts we would need in a continuous laser to make it the same as our pulsed laser. Thus we can conclude if there is a laser with

more power it would be a better option. Using the above method we can begin to calculate all of our variables as shown below.

The energy per pulse given to us from Quantel is as follows: Energy = 0.034 J + 0.036 J = 0.070 J or 70 mJ

Maximum Allowable Exposure Time: MAET (ms) = Pixel Size / Flow Velocity \* 1000 (ms/s)

Under our parameters we are assuming the following:

- (1) FOV is 40 cm x 40 cm
- (2) Flow speed is 5cm/s
- (3) Binning is 2x2 so pixel size = 0.39mm = 390um ((Ideal Sheet Thickness)).

We can use this information in our MAET equation and solve for our maximum allowable exposure time MAET (ms) = 390um/50,000um/s \* 1000 = 7.8ms

Finally we can plug in energy and time into the original equation

Energy = Watts \* Time

Where energy is the energy we currently have in our pulsed laser: Energy = 0.070 J And time is the maximum exposure time: Time = 0.0078s

Thus the minimum watts needed on a continuous laser is: Watts = 0.070 J / 0.0078 s = 8.97 W or 9 W \*\*

\*\*Note this is ignoring any saturation values in the pulsed laser, which is unknown. The linearity of acetone to laser power is shown in Appendix E.

## Appendix D

### Binning Comparison

In order to ensure that no data was lost by binning the images the following comparison demonstrates the differences between unbinned (2048x2048 pixels), 2x2 binned, (1024x1024 pixels) and 4x4 binned (512 x512 pixels). Examinations were done for unbounded and near bed data.

#### D.1 Unbounded Images

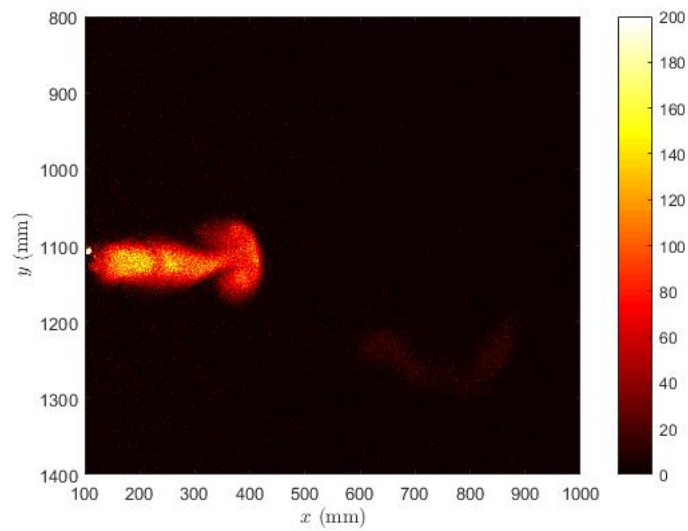


Figure D.1: Unbounded Data unbinned

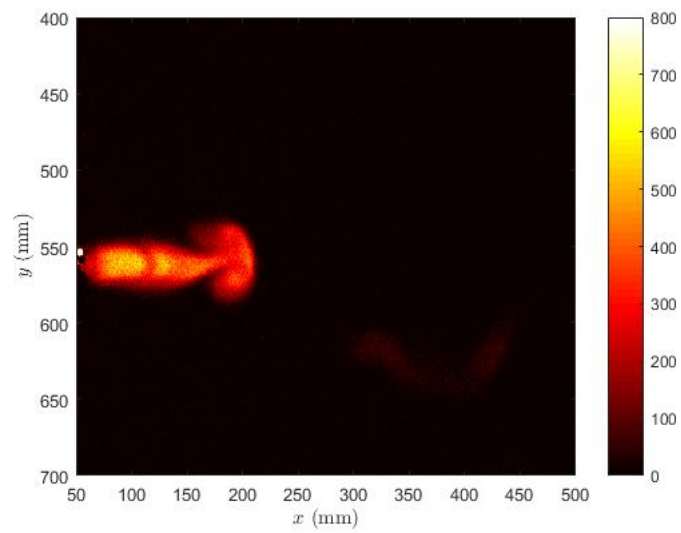


Figure D.2: Unbounded Data 2x2 binned

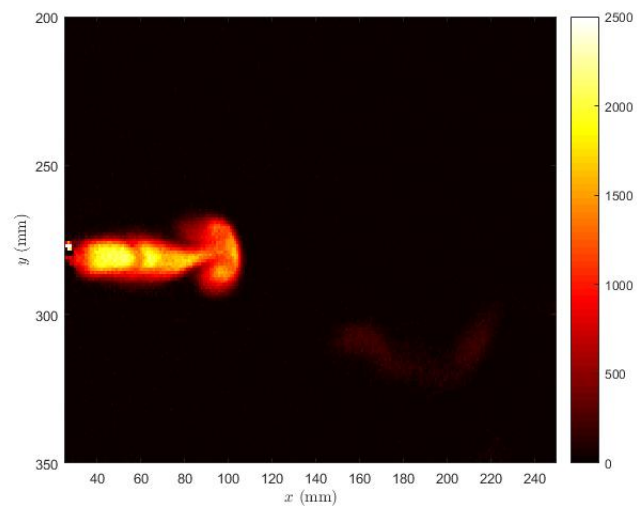


Figure D.3: Unbounded Data 4x4 binned

## D.2 Near Bed Images

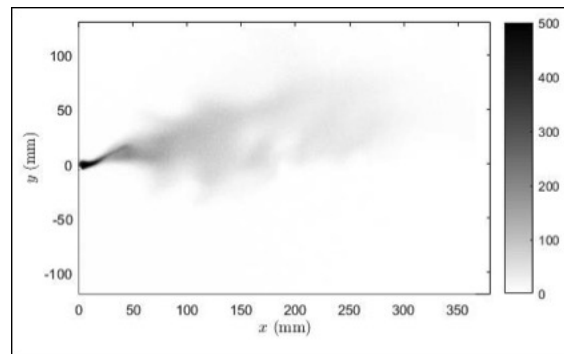


Figure D.4: Near bed Data unbinned

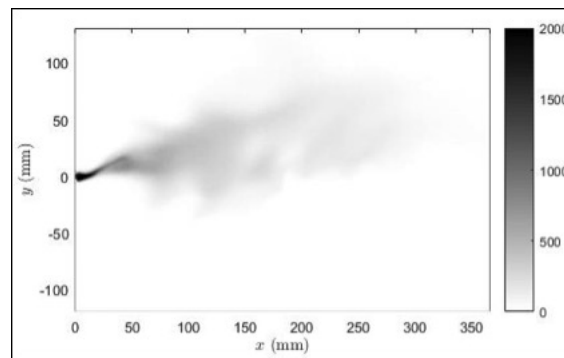


Figure D.5: Near bed Data 2x2 binning

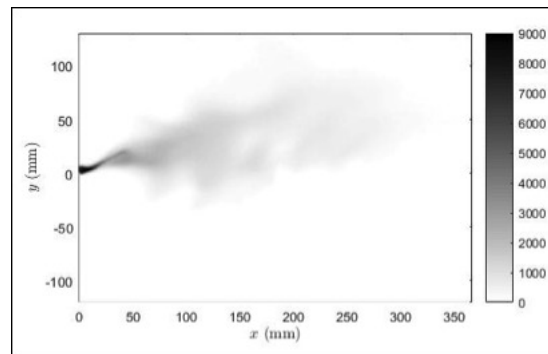


Figure D.6: Near bed Data 4x4 binning

## Appendix E

### Camera Components

#### E.1 Zyla 4.2+ Specifications

The Zyla 4.2+ was a carefully chosen camera, as described in more detail in F.3. Below are some of the relevant camera specifications, and more information can be found at the following website: <http://www.andor.com/scientific-cameras/neo-and-zyla-scmos-cameras/zyla-42-plus-scmos>.

- (1) Sensor Type: Front Illuminated Scientific CMOS(4T) -sCMOS 2.0
- (2) Active Pixels: 2048 x 2048 (4.2 Megapixel)
- (3) Sensor Size: 13.3 x13.3 mm (18.8 diagonal)
- (4) Pixel Size: 6.5  $\mu\text{m}$
- (5) Readout Noise: 0.9 e-
- (6) Maximum dynamic range: 33,000:1
- (7) Maximum Quantum Efficiency: 82%

The quantum efficiency of the camera is very important, as this is the spectral response of the sensor on the camera. Below is an image of the spectral response for the Zyla 4.2+.

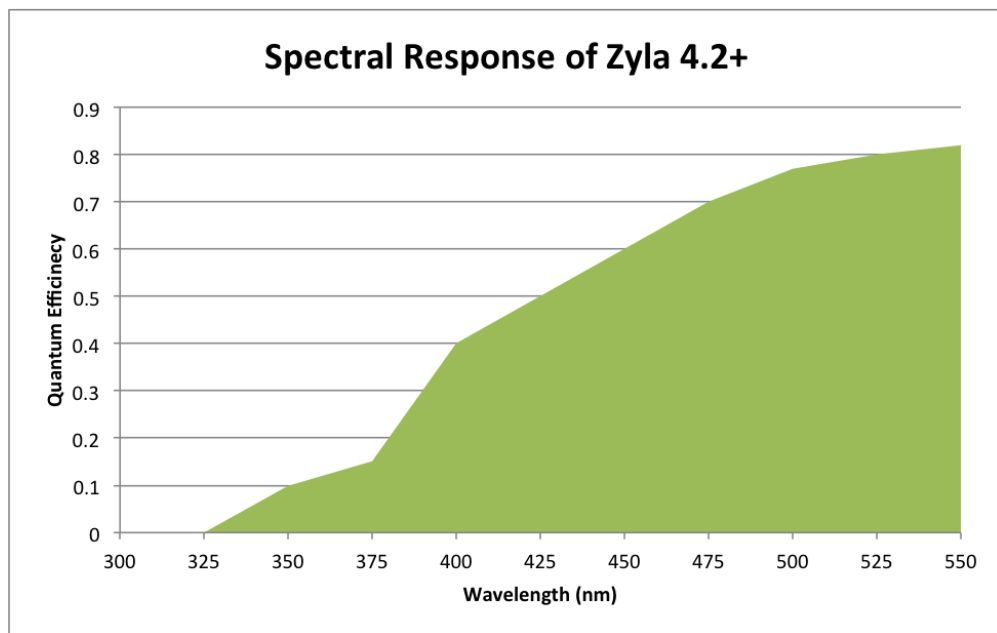


Figure E.1: Spectral Response of Zyla 4.2+ Camera



## E.2 Camera Comparisons

### E.2.1 Evaluation of Current 5.5 Megapixel sCMOS camera versus Zyla 4.2+ camera.

The cameras were set up under the following constraints:

- (1) The vertical dimension in the field of view: 30mm
- (2) The horizontal dimension in the field of view: 30mm for the 4.2+ and about 32mm 5.5.
- (3) 3mm of the tip of the nozzle were showing in each photo.

This gives 4.2+ about 11.3% advantage in terms of pixel area in the image. However, we find this advantage is almost negligible when comparing the overall increase in SNR with the 4.2+ camera.

In order to evaluate the images from the two cameras three measures were calculated. First, the average signal,  $\mu$ , from the controlled release of an acetone jet measured 1 diameter away from the exit nozzle and across the entire diameter of the jet was calculated. This signal value was averaged over an area of interest for each frame, then the final average was time averaged over 500 frames. This area of interest was approximately 2mm wide and a diameter of the jet long. This yielded the following plot and  $\mu$  values:

$$\mu_{4.2} = 1057 \text{ counts}$$

$$\mu_{5.5} = 461 \text{ counts}$$

Next, I evaluated the noise using the dark response images collected that same day. I calculated the time averaged RMSE for each individual pixel in the image, then averaged those RMSE values to obtain the overall average RMSE over the whole sensor and got the following:

$$\text{RMSE}_{4.2+} = 2.4 \text{ counts}$$

$$\text{RMSE}_{5.5} = 7.1 \text{ counts}$$

Next, to compare these numbers I calculated the SNR ( $\frac{\mu}{\text{RMS}}$ ) for each camera:

$$\text{SNR}_{4.2} = 1057/2.37 = 450$$

$$\text{SNR}_{5.5} = 461/7.14 = 65$$

Lastly, we can take three ratio values (4.2+/5.5) to compare the performance of the cameras.

$$\mu_{(4.2+)}/\mu_{(5.5)} = 2.3$$

$$\text{RMSE}_{4.2+}/\text{RMSE}_{5.5} = 0.33$$

$$(\mu/\text{RMS})_{(4.2+)}/(\mu/\text{RMS})_{(5.5)} = 8.6$$

**Thus the new camera is approximately 9 times better than the CCD camera.**

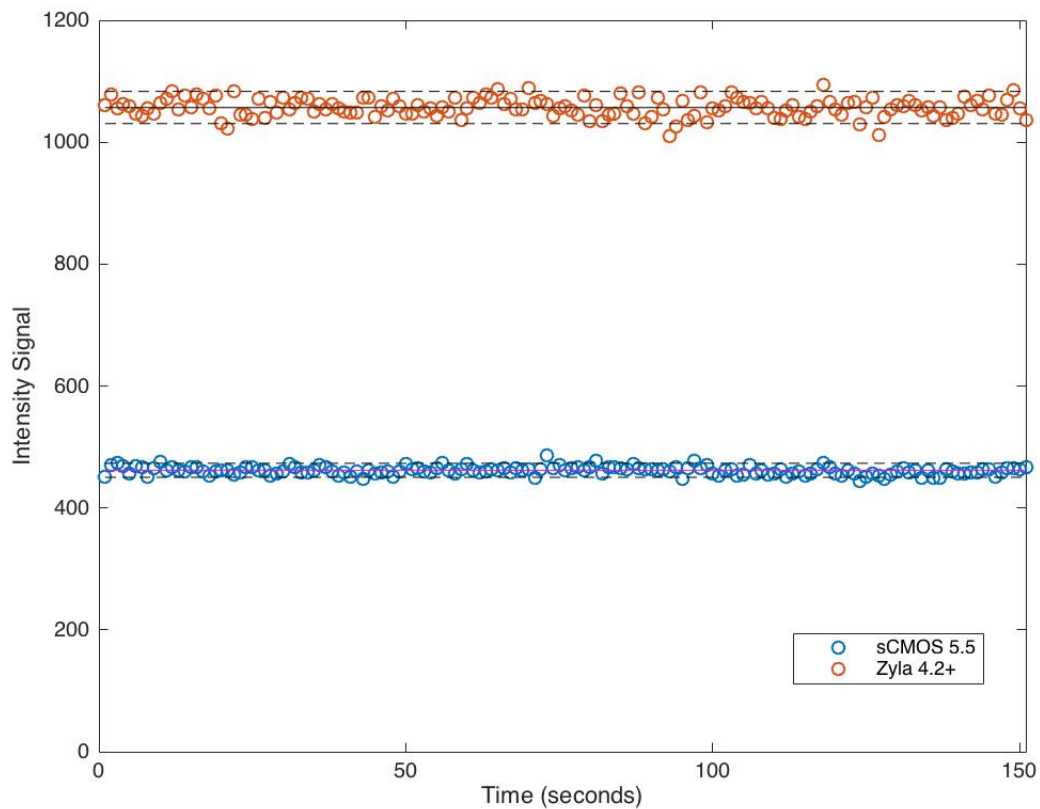


Figure E.2: Comparison of sCMOS 5.5 vs. Zyla 4.2+

### E.2.2 Comparing the Zyla 4.2+ to the Ultra 888

Next the 4.2+ Zyla was also compared to the Andor Ultra 888. In a similar manner as described above the average of the core of a jet was measured, and the noise using the dark

response was measured. In the Andor Ultra 888, the signal was several magnitudes order higher than that of the Zyla 4.2+, however so was the noise. For example, over multiple trials, all data produced similar results to those below:

$$\mu_{Ultra} = 3761 \text{ counts}$$

$$\mu_{zyla} = 200 \text{ counts}$$

$$RMS_{Ultra} = 42 \text{ counts}$$

$$RMS_{zyla} = 2 \text{ counts}$$

$$SNR_{Ultra} = 90$$

$$SNR_{zyla} = 200$$

**Therefore, the Zyla 4.2+ is about 2.22 times better than the Ultra 888.**

### E.3 F-Stop Theory and Calculations

Decreasing your f-stop number increases light allowed into the image on a logarithmic scale. In the table below we see f-stop number (N) increasing by 1/4 stop each column, the Aperture Value (AV). Thus from green to green columns is one full f-stop, while the yellow columns to yellow columns is also one full stop, and blue to blue is half stop in between each. Since we know light doubles with each full stop, this table is a good reference or check to these calculations

In general we can use the following formula to calculate percentage of light change dependent upon f-stop change. Factor of Light Change for changing f-stop number (FLC) =  $2^n$

where  $n = \left| \frac{\ln(A/B)}{\ln(\sqrt{2})} \right|$

- (1) A: F-stop number you are starting with
- (2) B: F-stop number you are going to
- (3) n: exact number of f stops between A and B

Example: How much does the amount of light change between f/1.7 and f/1.1?

$$\begin{aligned} \text{FLC} &= 2n \\ n &= \left| \frac{\ln(1.7/1.1)}{\ln(\sqrt{2})} \right| = 1.25 ** \\ \text{FLC} &= 2 * 1.25 = 2.5 \end{aligned}$$

\*\*note the same number is calculated even if you switch 1.7 and 1.1, just be sure to always take absolute value to get f stop.

Thus it is 1.25 f-stops between 1.7 and 1.1, which we can also verify using the table, and this multiplied by factor of 2 gives you how much light changes between the two. This factor works for both directions, thus if you go from f/1.1 to f/1.7 you lose 2.5 light you had at f/1.1. Note: When computing n it is customary to round down if the numbers are not exactly on quarter scale. Thus if not 0.25, 0.5, or 0.75. For example if you compute the difference between f/1.2 and f/1.8 you get the following:

$$\begin{aligned} \text{FLC} &= 2 * n \\ n &= \left| \frac{\ln(1.8/1.2)}{\ln(\sqrt{2})} \right| = 1.17 \end{aligned}$$

Thus here it is customary to round down to 1.0 and not up 1.25. Thus again if any numbers are not exactly on the quarter scale, it is customary to round down to the nearest full or half stop.

#### E.4 Edmund Optics Notch Filter

A 50mm 532nm notch filter was purchased from Edmund Optics to block residual 532nm light from the captured data images. The percent transmittance curve is shown below, showing a very narrow notch (17nm) about 532nm. The average percent transmission between 350-400nm is over 80%, while the average between 400-1200nm is over 90%. The filter is hard coated with an optical density (OD) of greater than 6.0. The optical density is on a log scale as follows:

$$\begin{aligned} OD &= -\log\left(\frac{T}{100}\right) \\ T(\%transmitted) &= 10^{-(OD)} * 100\%. \end{aligned}$$

Therefore, the percentage of 532nm transmitted through the filter is 0.0001 %. This filter was determined to be the best on the market at the time (2016) in terms of OD, notch width, and cost. More information on the filter can be found at <https://www.edmundoptics.com/optics/>

optical-filters/notch-filters/od-6-notch-filters/86130/.

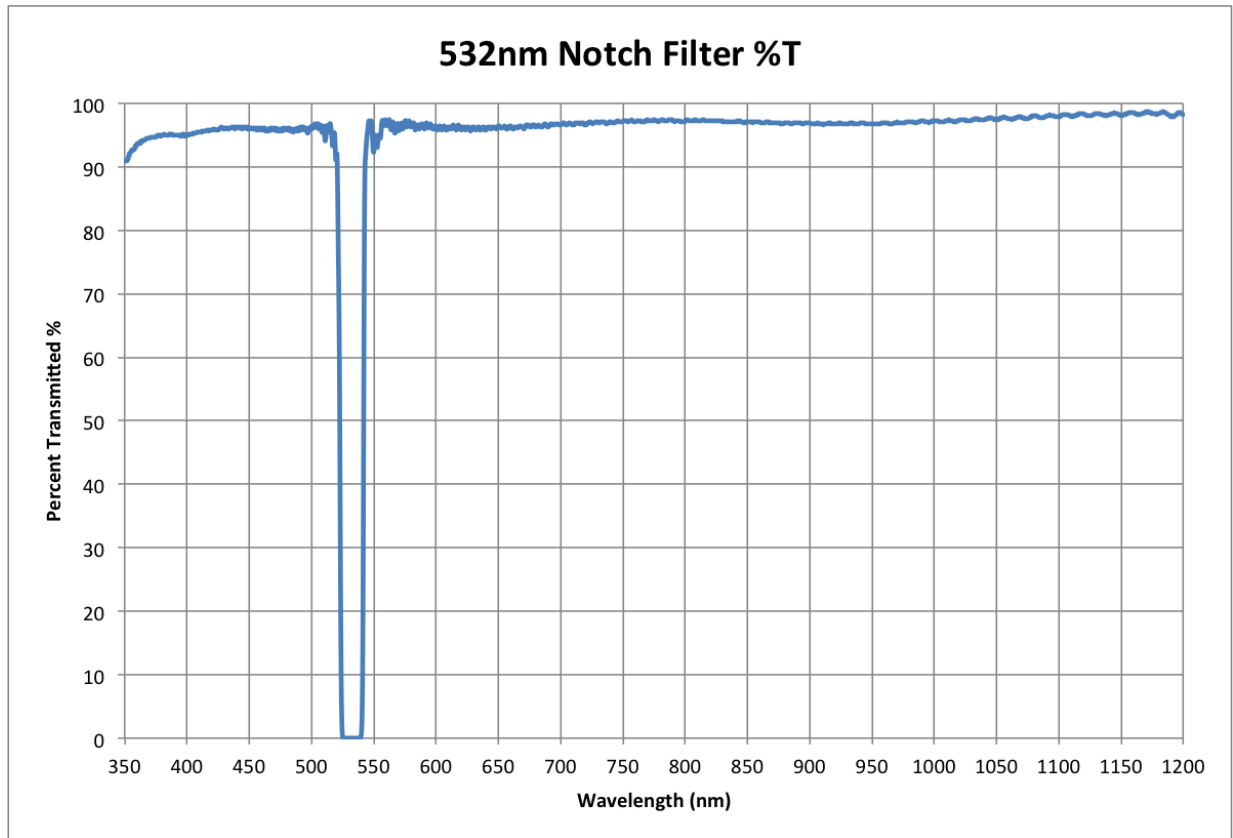


Figure E.3: 532nm Notch Filter Spectra

## **Appendix F**

### **Camera Insight 4G Software Settings**

The software settings in Insight 4G include setting hardware options to USB 3.0, Camera to Zyla 4.2 and a synchronized simulator option on. The global shutter should be checked in the components tab.

## Appendix G

### Acetone PLIF and Beer's Law

#### G.1 Understanding Beers Law in a Wind Tunnel

In this wind tunnel pictured in Figure1, we can see that it is constructed of foam core, and not perfectly sealed. The slits on the side for laser entry are sealed with a FTPE film and the openings during flatfielding are sealed off with retrofitted foam core pieces.

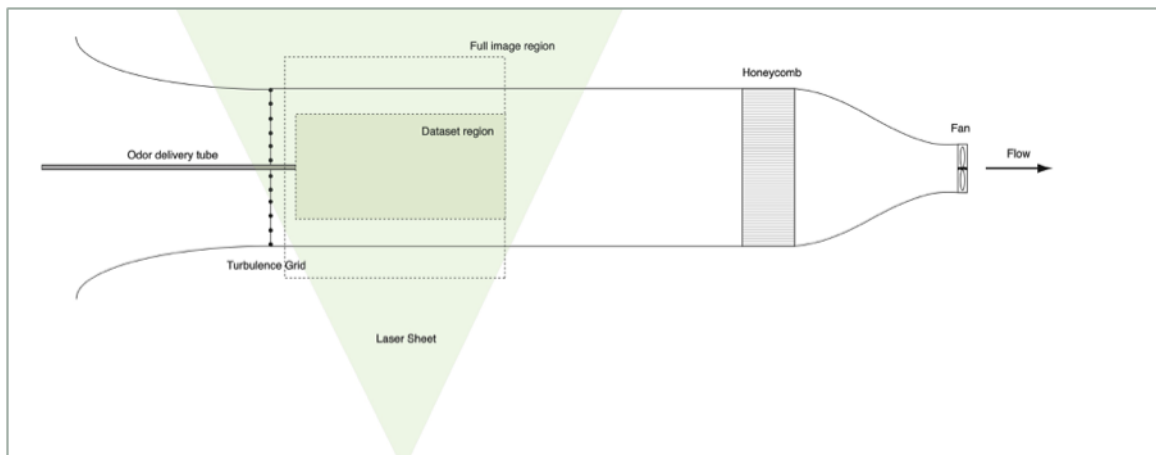


Figure G.1: Wind Tunnel Schematic

During this flatfielding exercise, it was discovered that acetone vapor at high concentrations has a significant effect on absorption and Beer's Law as seen in Figure 2 which shows close to a 50% loss in concentration over the 30cm path length. What this image also shows is a non-linear increase in concentration over 25 minutes, which in fact should be a linear increase. Due to this behavior it was examined if acetone was being lost in the wind tunnel due to it not being perfectly

sealed, and possible absorption of acetone into the foam core.

This indeed was the case, and it was found that over a period of 10 minutes the acetone decreased by a factor of 3 as we can see in Figure 3. To remedy this I averaged over 300 pixels for each time curve, and fit it to a 1st-order decay equation:

$$A = A_0 * e^{-(k*t)}$$

To remedy this situation I fit a decay curve following equation 1 to the data in Figure 3. The first 300 pixels were averaged over each time point and then used to create the following curve in Figure 4. This curve illustrates that the loss is exponential in nature, most likely due to the mixing out of acetone at lower concentrations, thus making it concentration dependent.



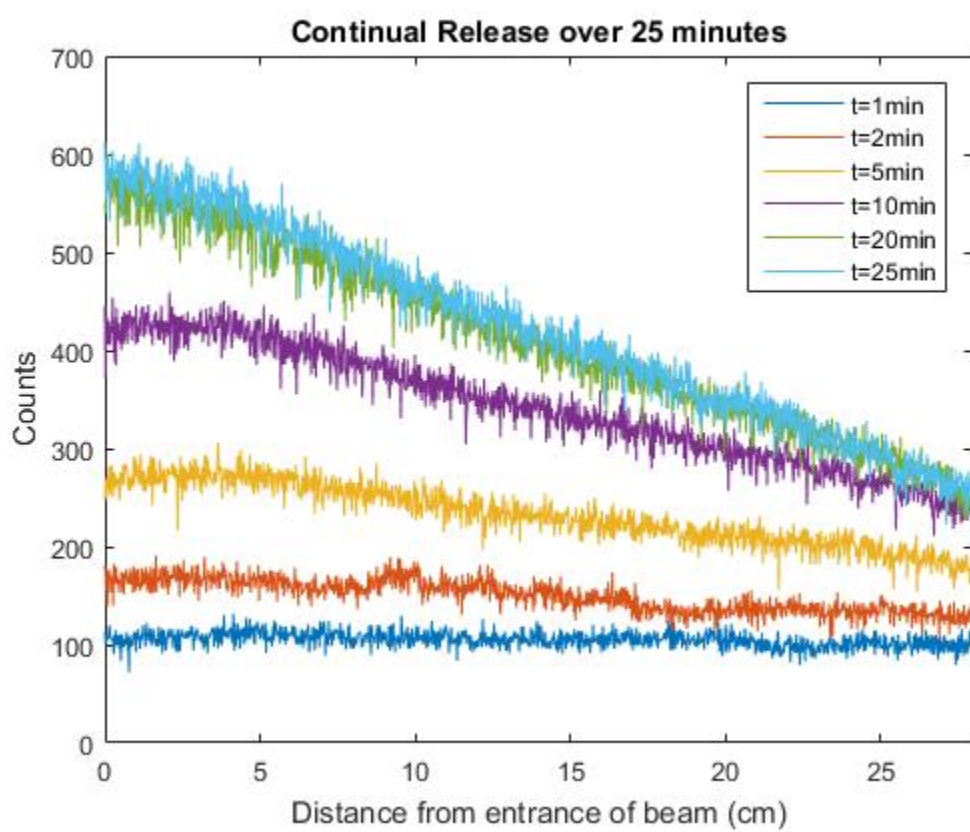


Figure G.2: Continuous Release of Acetone into wind tunnel over 25 minutes

Using the mathematics to solve for a solution for a well mixed reactor as a model then adding in a loss term as described above we get the following solution:

$$\frac{dM}{dt} = R_{in} - R_{out} - R_{rxn}$$

Where  $M$  is defined as mass, and  $R$  is the rate at which it is entering and exiting the system.

$$R_{in} = Q_{in} * C_o \quad R_{out} = Q_{out} * C_{mix}(t) \quad R_{rxn} = -k * V * C_{mix}(t)$$

We can then redefine our well mixed concentration,  $C_{mix}$  as the mass at a specific time divided by the total volume of air in our system. Such that

$$C_{mix}(t) = \frac{M(t)}{V}$$

Note that  $M$  changes with time, since  $C_{mix}$  is also dependent upon time.

Now rearranging we can write equation 1 as follows:

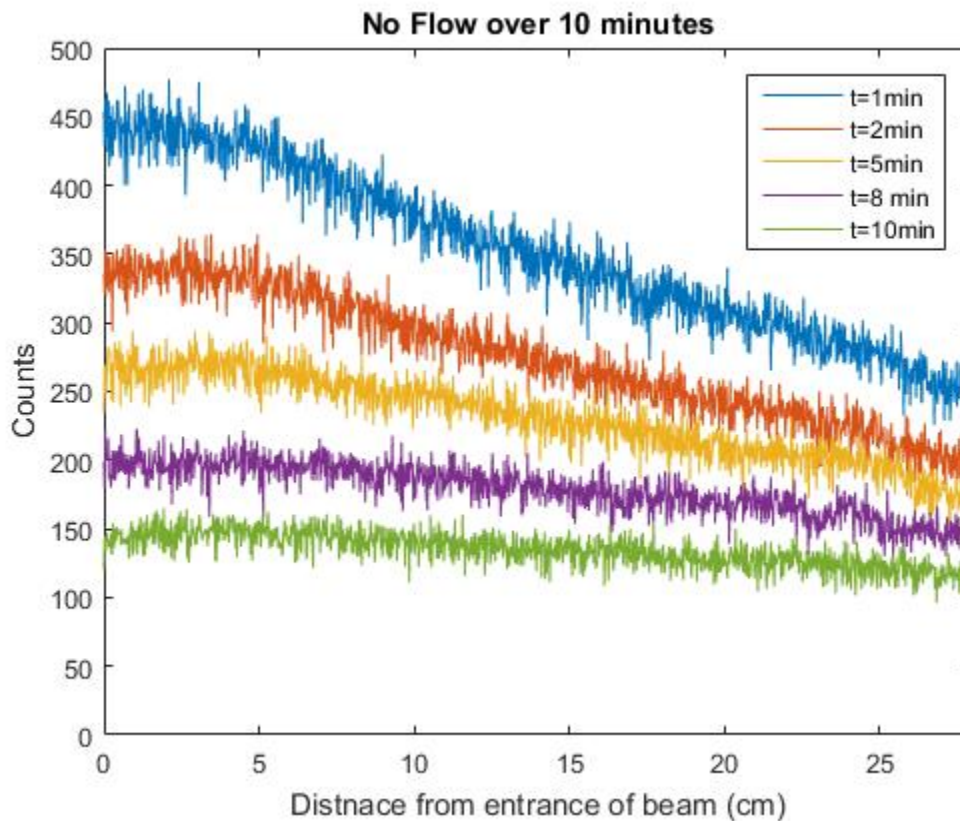


Figure G.3: No Flow in acetone loss over 10 minutes

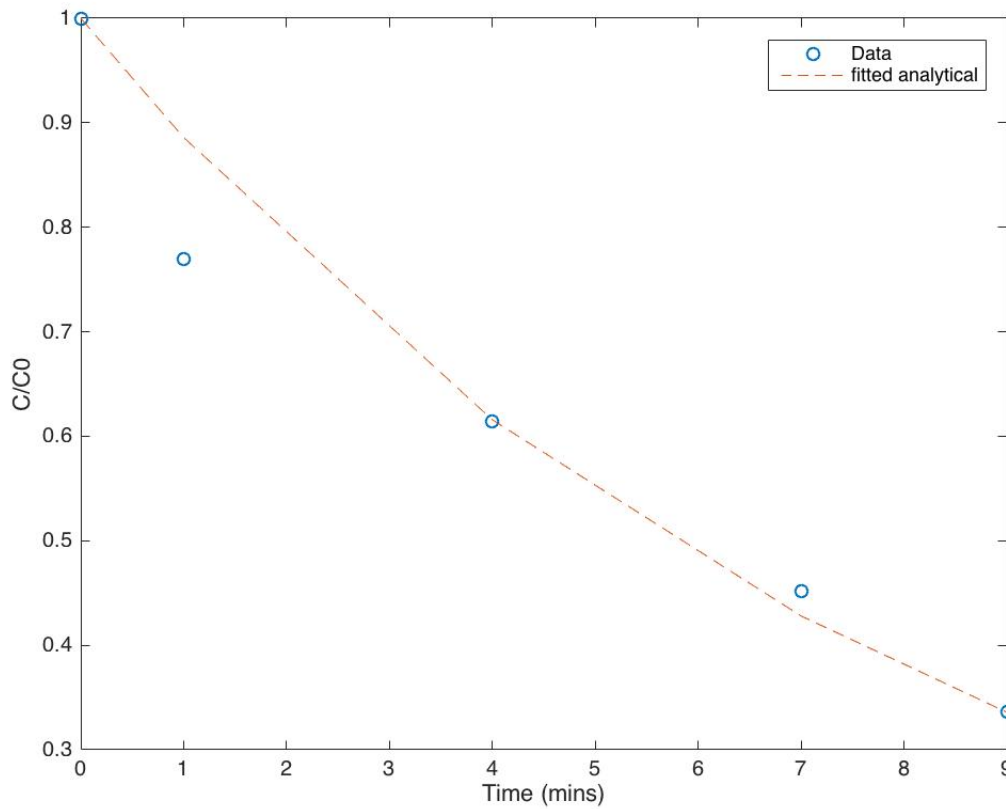


Figure G.4: Fitted analytical solution from equation to loss of acetone over time

$$\frac{dM}{dt} = Q_{in} * C_o - (Q_{out} - k * V) * \frac{M(t)}{V}$$

We can see that this is a linear differential equation which we can arrange to solve.

$$\frac{dM}{dt} + (Q_{out} * -k * V) * \frac{M(t)}{V} = Q_{in} * C_o$$

And

$$M(t) = \int \frac{u(t)*q(t)dt+K}{u(t)}$$

We can define our function  $u(t)$  as follows:

$$u(t) = e^{\int \frac{Q}{V} dt} \quad u(t) = e^{\frac{Q}{V} t}$$

We know that  $q(t)$  is equal to the following:

$$q(t) = Q * C_o$$

So we can plug back into equation 3 and get:

$$M(t) = \int \frac{e^{QVt} * Q * C_o * dt + K}{e^{\frac{Q}{V} * t + k * t}}$$

Which after solving the integral and canceling terms we get:

$$M(t) = C_o * V + K * e^{-\frac{Q}{V} * t + k * t}$$

Now to solve for constant K, we can use an initial condition of  $M(t = 0) = 0$  or in other words at  $t=0$ , there is no acetone in the system.

Plugging that in we get:  $K = -C_o * V$

So plugging back into the final equation and dividing by the volume, V we can rewrite the solution as  $C_{mix}(t)$  :

$$C_{mix}(t) = C_o * 1 - e^{-(\frac{Q}{V} + k) * t}$$

This addition of k constant results in the final equation above, and as seen in Figure 5 matches almost perfectly with the behavior of the system.

Now that this loss has been explained, I can also estimate the absorptivity coefficient using Beer's Law and Figure 6.

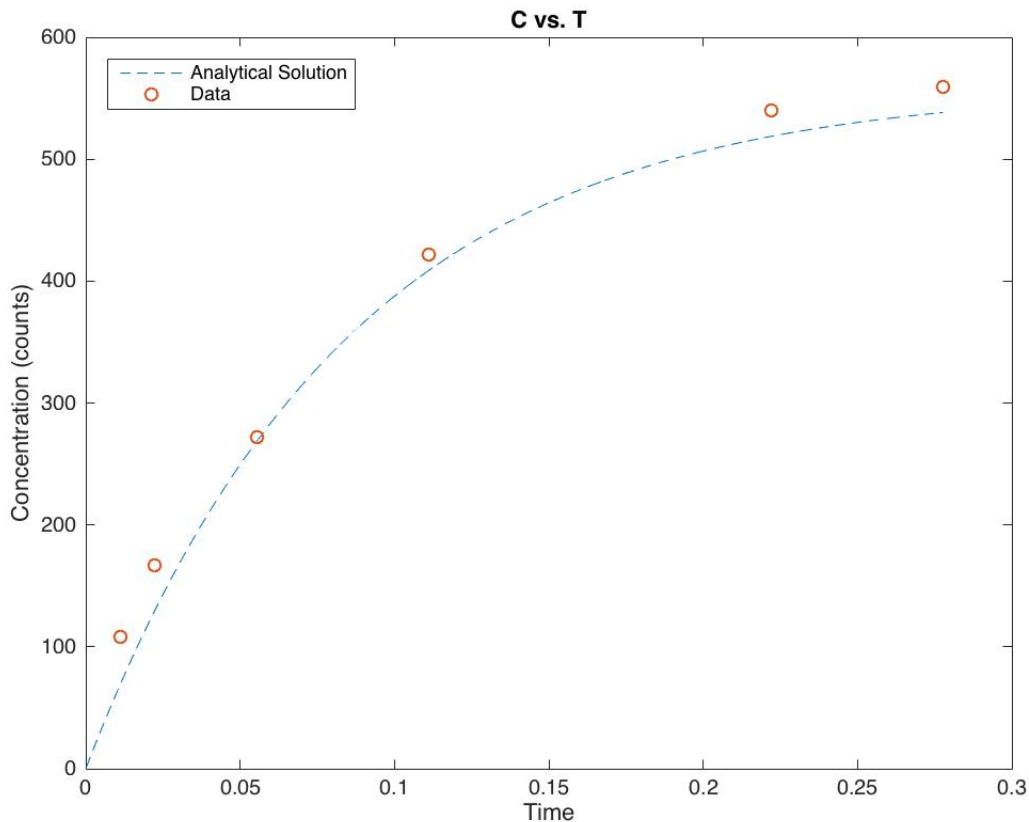


Figure G.5: Fitted analytical solution with concentration data over 25 minutes

### Absorption Coefficient Estimate

To estimate the absorption coefficient in Beer's law I can fit Beers law to current data then estimate the coefficient  $\epsilon$ . To do this I normalized each data time used to the maximum so data ranged (for the most part) from 0 to 1. Then I calculated the concentrations for each time using the final solution below and applied to Beers Law with that concentration.

$$C_{mix}(t) = C_o * 1 - e^{-(\frac{Q}{V}+k)*t}$$

where Q is the flow rate in the wind tunnel, V is the total volume of the tunnel, k is the decay or loss rate, and t is the time in question.

$$I/I_0 = \exp(-\epsilon * C * b)$$

where  $b$  is the path length of where the data point was taken relative to the laser beam entry.

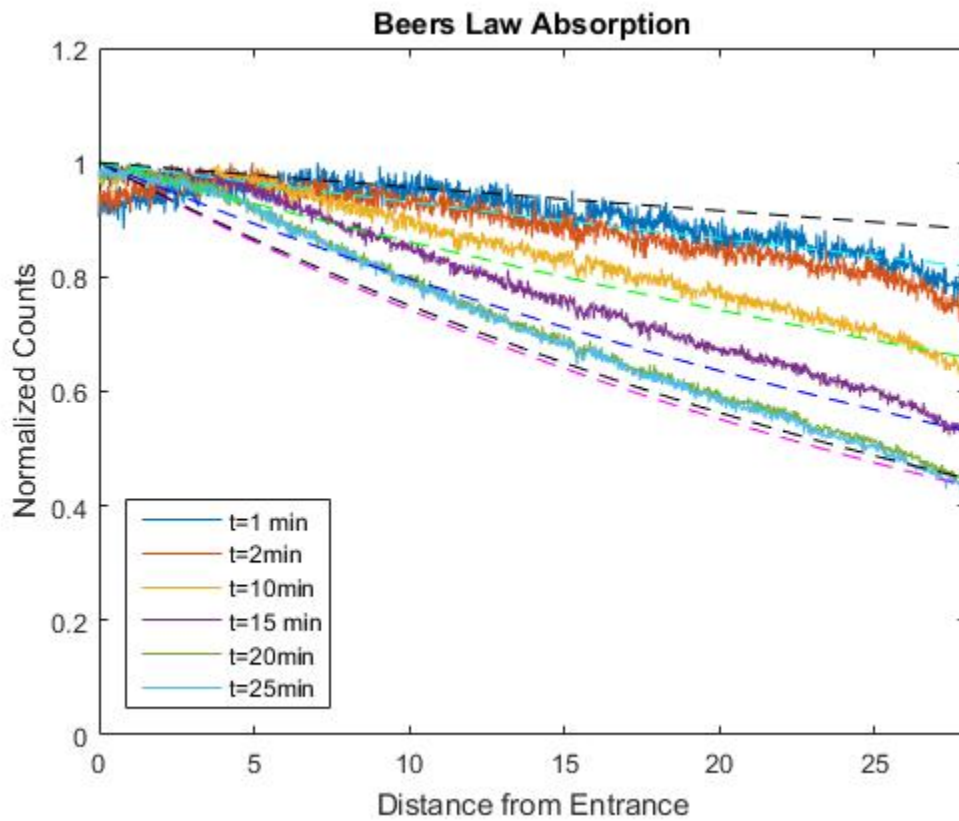


Figure G.6: Normalized Beers Law with data

In Figure 6 the best matched epsilon was  $50 \frac{cm^2}{g}$ . However, this value was not consistent among other trials, so further investigation into the coefficient value is needed.

## Appendix H

### Codes for Processing Data

#### H.1 Code for processing unbounded data

Below is the MATLAB code for processing the unbounded data. Please note some variables may not be used.

Below is the MATLAB code for processing the bounded code. Please note some variables may not be used.

4/13/17 9:28 AM /User.../SecondLevelProcessingUnbounded\_MKM.m 1 of 16

---

```

%second level processing
clc; clear all; close all;
%when changing framing rates need to change following variables:
%FFF=35; %5Hz
%FFF=90; %15Hz
FFF=70; %30Hz
%fps, ni
fps=30; %frame rate
ni=9000; %number of images

%background for flatfield
cd('D:/InsightFolder/Experimentz/DarkResponse/RawData/30Hz_FFBG')
J4=0; K4=[];
tifFiles=dir('*.tif');
for k4 =1:length(tifFiles)
    filename=tifFiles(k4).name;
    I4=imread(filename);
    I4=double(I4);
    J4=J4+I4;
end
backgroundFF=J4./(length(tifFiles));
%converts to double array to use in matrix commands
backgroundFF=double(backgroundFF);

%flatfield
cd('D:/InsightFolder/Experimentz/DarkResponse/RawData/All30Hz')
J1=0; K1=[]; I2=0;
tifFiles=dir('*.tif');
for k1 =1:length(tifFiles)
    filename=tifFiles(k1).name;
    I1=imread(filename);
    I1=double(I1);
    I2=I1-backgroundFF;
    J1=J1+I2;
end
flatfield=J1./(length(tifFiles));
flatfieldnoBG=I2./length(tifFiles);
%converts to double array to use in matrix commands
flatfield=double(flatfield);
%imagesc(flatfield)
flatfield_norm=flatfield./FFF;

cd('D:/InsightFolder/Experimentz/TuesdayData_Unbounded/RawData/BG_30Hz')
J=0; K=[];
tifFiles=dir('*.tif');
for k =1:length(tifFiles)
    filename=tifFiles(k).name;
    I=imread(filename);
    I=double(I);
    J=J+I;
end
background=J./length(tifFiles);
%converts to double array to use in matrix commands
background=double(background);

%upload raw data and convert to double array
cd('D:/InsightFolder/Experimentz/TuesdayData_Unbounded/RawData/Data_30Hz'); %cd('C:\
\Users\LaVision\Desktop\Maggie\v') %
J2=0; K2=[];

```



4/13/17 9:30 AM /Users/margaretmchugh.../SecondLevelNearBed.m 1 of 16

---

```

%second level processing for near bed data
clc; clear all; close all;
%when changing framing rates need to change following variables:
%FFF=60; %5Hz
%FFF=90; %15Hz
FFF=70; %30Hz
%fps, ni
fps=30;
ni=9000;

%background for flatfield
%cd('D:/InsightFolder/Experimentz/DarkResponse/RawData/15Hz_FFBG')
%cd('D:/InsightFolder/Experimentz/DarkResponse/RawData/5Hz_FFBG')
cd('D:/InsightFolder/Experimentz/DarkResponse/RawData/30Hz_FFBG')
J4=0; K4=[];
tifFiles=dir('*.tif');
for k4 =1:length(tifFiles)
    filename=tifFiles(k4).name;
    I4=imread(filename);
    I4=double(I4);
    J4=J4+I4;
end
backgroundFF=J4./(length(tifFiles));
%converts to double array to use in matrix commands
backgroundFF=double(backgroundFF);

%flatfield
%cd('D:/InsightFolder/Experimentz/DarkResponse/RawData/All15Hz')
%cd('D:/InsightFolder/Experimentz/DarkResponse/RawData/All5Hz')
cd('D:/InsightFolder/Experimentz/DarkResponse/RawData/All30Hz')
J1=0; K1=[]; I2=0;
tifFiles=dir('*.tif');
for k1 =1:length(tifFiles)
    filename=tifFiles(k1).name;
    I1=imread(filename);
    I1=double(I1);
    I2=I1+I2;
    I3=I1-backgroundFF;
    J1=J1+I3;
    I4=I1;
    M=I4;
    p=2; q=2; %binning size you want
    [m,n]=size(M); %M is the original matrix
    M=sum(reshape(M,p,[ ]),1);
    M=reshape(M,m/p,[ ]).'; %Note transpose
    M=sum( reshape(M,q,[ ]),1);
    M=reshape(M,n/q,[ ]).'; %Note transpose
    FF(:, :, k1)=M;
end
flatfield=J1./(length(tifFiles));
flatfieldnoBG=I2./length(tifFiles);
%converts to double array to use in matrix commands
flatfield=double(flatfield);
flatfieldnoBG=double(flatfieldnoBG);
imagesc(flatfield)
flatfield_norm=flatfield./FFF;

%background images for data

```

## Appendix I

### Sources of Error and Noise

As mentioned in Chapter 3, there are significant sources of error at the source release of the plume. This RMS is thought to be due to the laser head variation. In the 30Hz data this RMS at pixel 1, which is the pixel located right at the source, has a value of 0.08C0 for the unbounded data and 0.13C0 for the bounded data. These values are normalized by the average concentration at that pixel over time. This noise is much higher than what we would expect in the 30Hz data, however in 30Hz data the heads are alternating and are slightly offset from one another, therefore, we expect a higher noise due to this difference in location. Furthermore, a higher noise is expected in the bounded data as there is a higher signal and more persistent signal which can demonstrate the difference in head locations more than in the lower signal unbounded data which wavers much more. Below are a few plots comparing the heads for both unbounded and data. Other sources of error could include but are not limited to, the acetone generation system, camera, and diffusion and advection of the release.

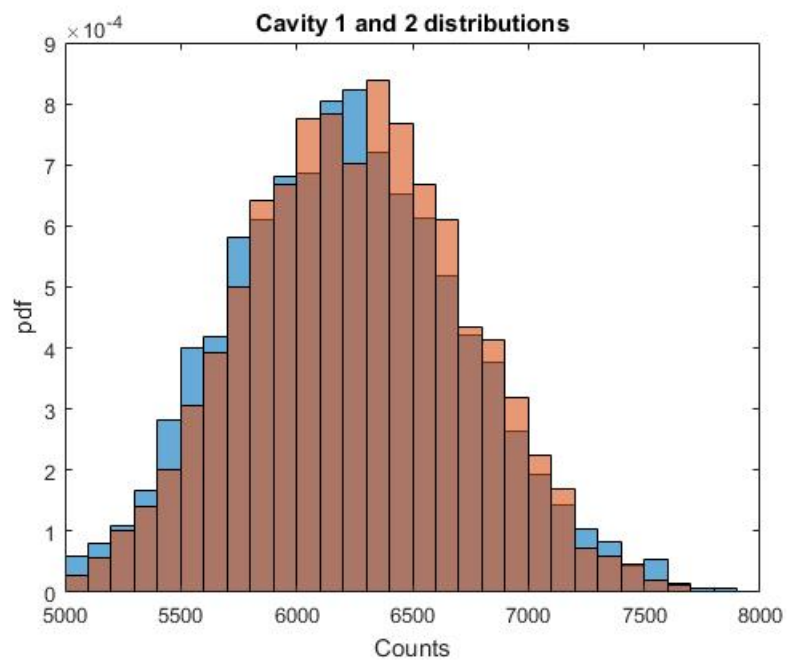


Figure I.1: Normalized pdfs of the unbounded 30Hz data, with two heads separated and shown in different color.

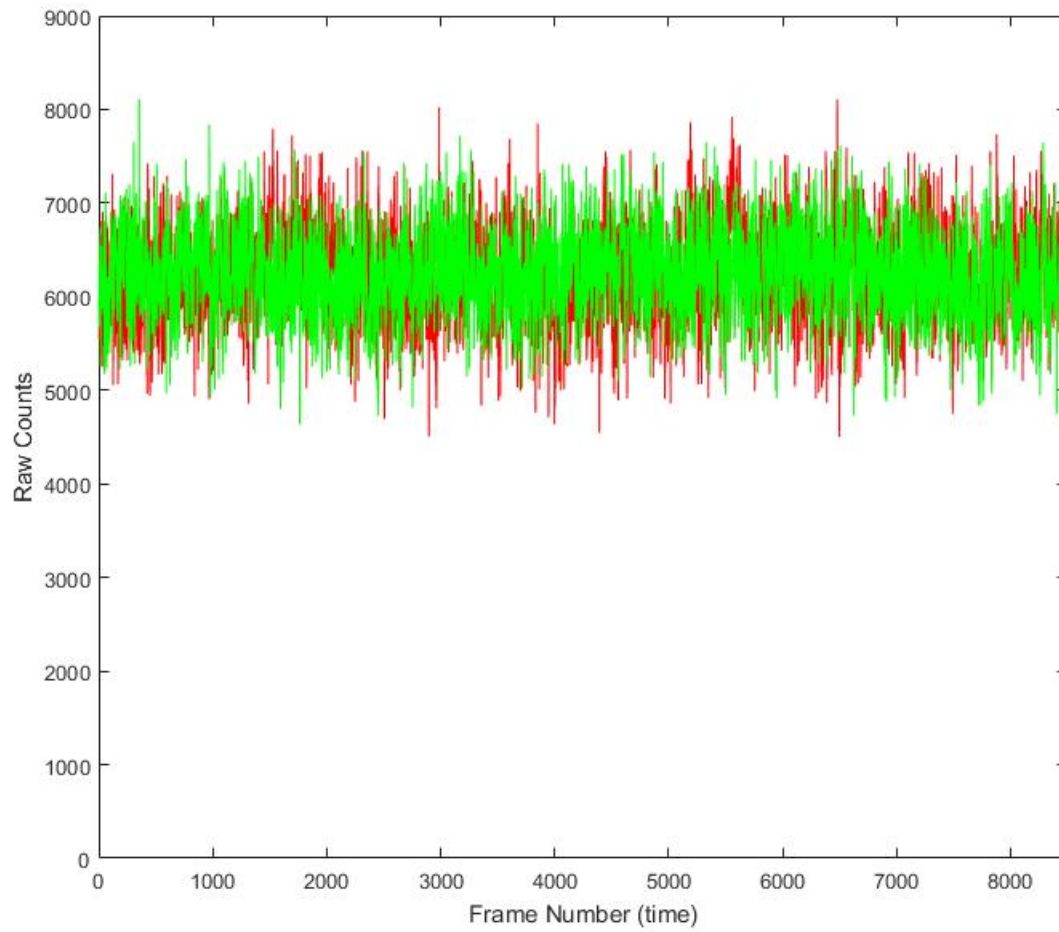


Figure I.2: Time-series of pixel 1, which is source location of the plume for the 30Hz unbounded data. The two heads are separated and shown in different colors.

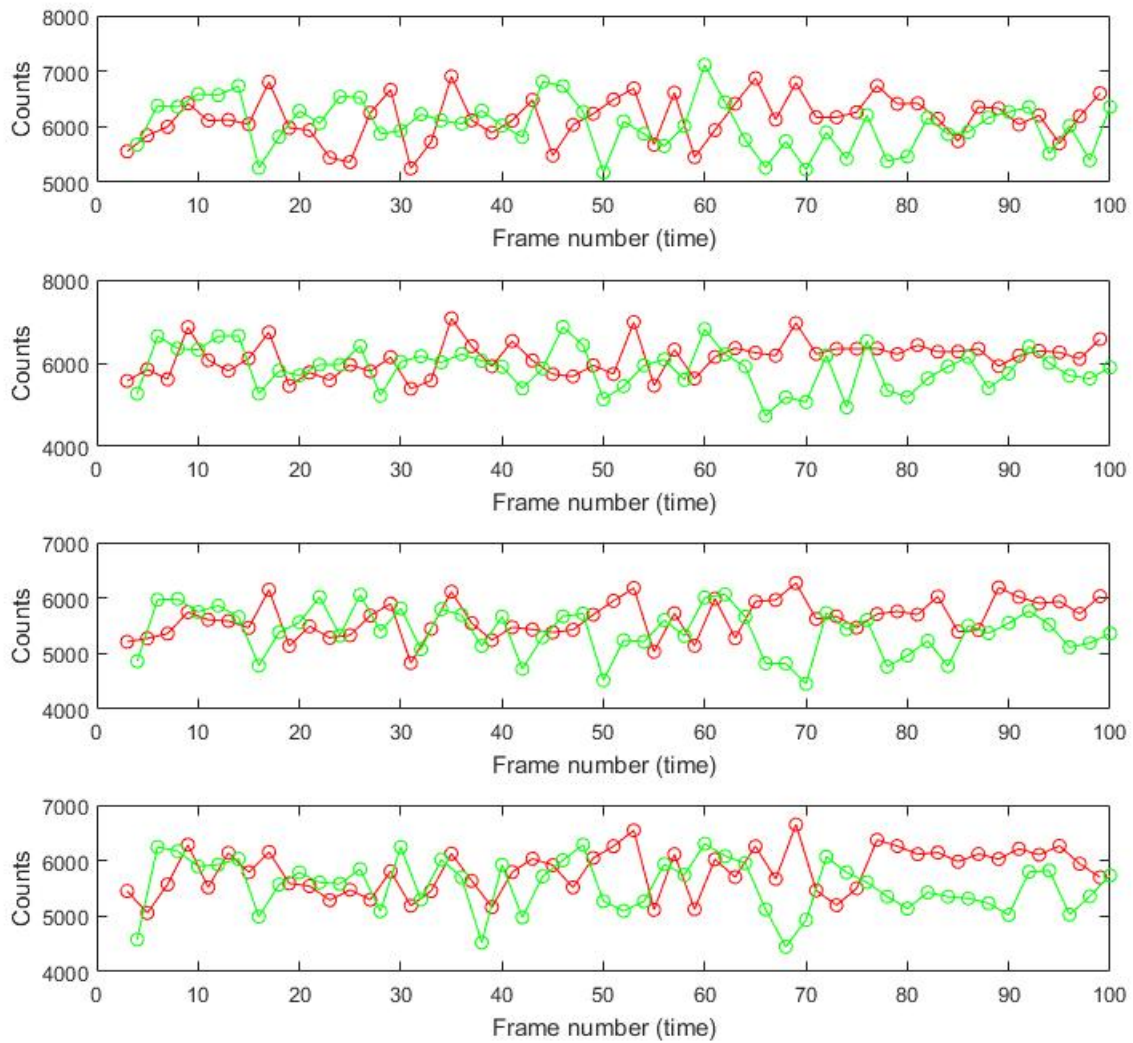


Figure I.3: Time-series of pixels 1-4 along the centerline. The two heads are separated and shown in different colors.

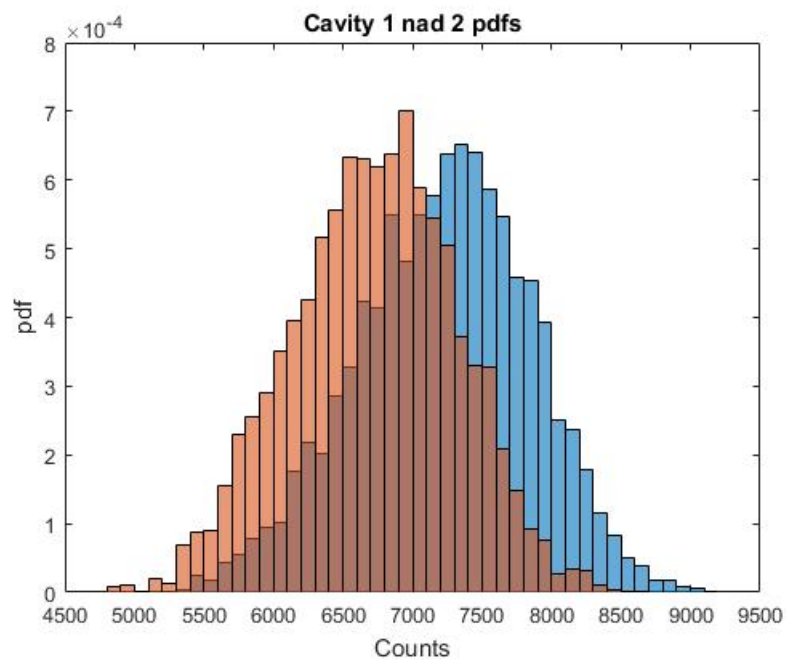


Figure I.4: Normalized pdfs of the bounded 30Hz data, with two heads separated and show in different colors.

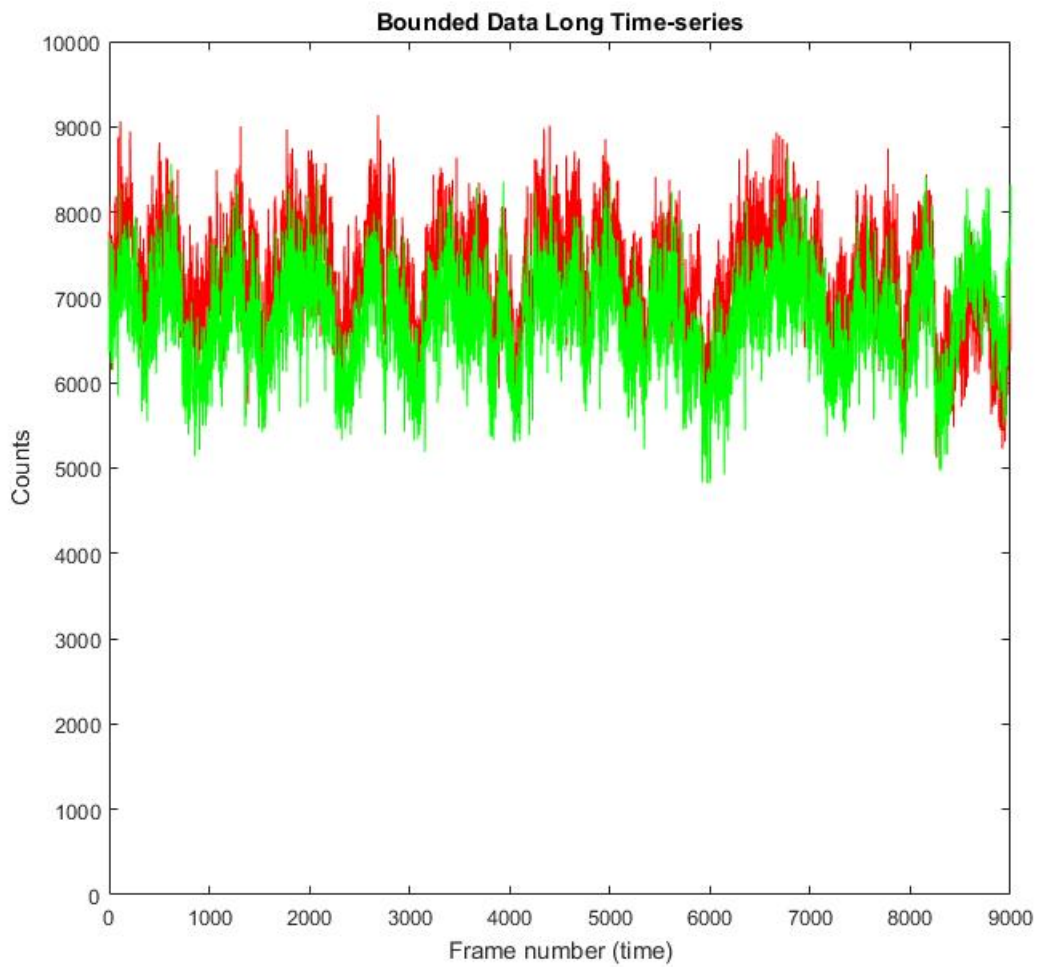


Figure I.5: Time-series of pixel 1, which is source location of the plume for the 30Hz bounded data. The two heads are separated and shown in different colors.

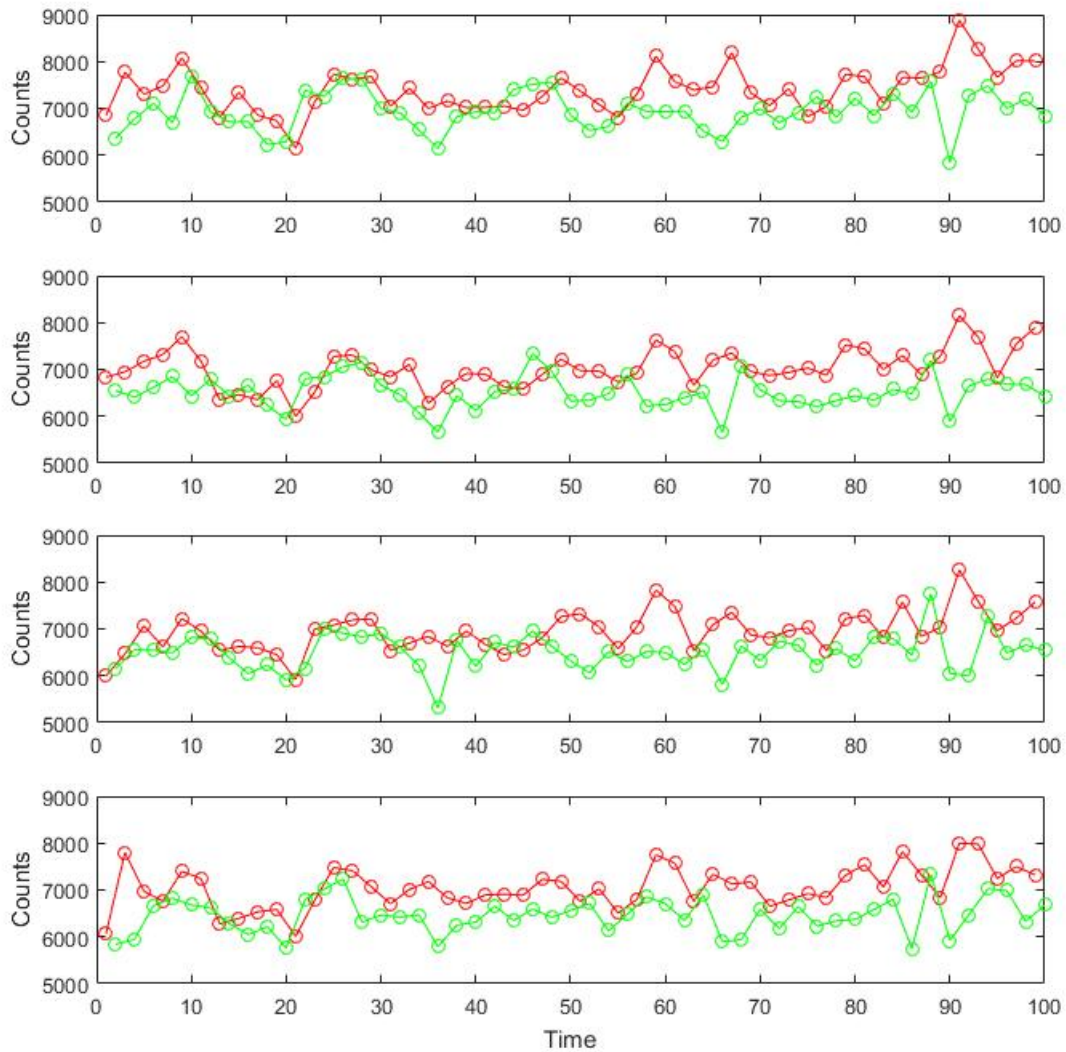


Figure I.6: Time-series of pixels 1-4 along the centerline. The two heads are separated and shown in different colors.